Study of 5%MgO:PPLN and CdSiP2 for infrared parametric generation

Pierre Brand

Study of 5%MgO:PPLN and $CdSiP_2$ for infrared parametric generation

Pierre Brand

Doctoral Thesis in Physics

Université Joseph Fourier

Defense: July 9th, 2010

François Balembois	Professor at Université Paris XI	Rapporteur
Michel Lefèbvre	Maître de recherche at ONERA	Rapporteur
Takunori Taira	Associate Professor at IMS	Examitateur
Jacques Dérouard	Professor at Université Joseph Fourier	Examinateur
Benoît Boulanger	Professor at Université Joseph Fourier	Directeur
Patricia Segonds	Maître de conférences at Université Joseph Fourier	Co-directrice

Institut Néel, CNRS/UJF
25 rue des Martyrs
BP 166
38042 Grenoble cedex 9

Avant-propos

Cette thèse s'est déroulée dans le département "Matière Condensée, Matériaux et Fonctions" de l'Institut Néel sous la direction de Benoît Boulanger et Patricia Segonds. Je tiens à leur adresser ici toute ma reconnaissance pour avoir remarquablement encadré le travail. Je les remercie particulièrement pour leur disponibilité et la confiance qu'ils m'ont accordée durant ces trois années.

Je remercie aussi Bruno Desruelles, de la Délégation Générale de l'Armement, pour avoir accordé un financement à ce travail.

J'aimerais également remercier et féliciter Bertrand Ménaert pour avoir réalisé les deux sphères sur lesquelles tout mon travail a reposé. J'espère qu'il m'excusera pour l'état dans lequel je les laisse en partant ! Je remercie aussi Corinne Félix pour son aide en optique, Jérôme Debray pour le polissage et l'orientation des cristaux, et Christophe Bouchard pour son aide à l'atelier.

Je salue aussi Yannick, qui avait commencé durant sa thèse le travail que j'ai poursui, et je souhaite bonne chance à Vincent qui prendra la suite.

Ma thèse s'est déroulée dans un environnement très convivial grâce à tous les membres du bâtiment F et à tous les thésards du département. Je pense en particulier à Simon, avec qui les heures passées dans la salle d'optique ont été très agréables, malgré l'obscurité et le bruit des lasers ! Je pense également à Julien et tout le VTT qu'on a fait ensemble, à Houmed, Issam, Sandra, Audrey, Oana, Marcio, Cécile, Vinicius, Marta, Yan, Mariana, Michèle, Jonathan.

Bien sûr, je n'oublie pas mes amis et ma famille dont le soutien est infaillible.

Finalmente, tengo a ringraziare Valeria per tutto l'amore che mi ha dato e per tutti i chilometri che ha fatto per venirmi a trovare regolarmente durante questi tre anni. Ti amo buneddhra!

Contents

Introduction

Nowadays, number of applications in the fields of research, medicine, industry or defense take advantage of coherent sources, mainly thanks to the monochromatic light and the high power they can deliver. The demand always increases for either ultra-short pulses or high energy, or the access to different wavelengths. Among the different types of sources, solid-state lasers suit to a lot of requirements because they are robust and they offer a wide range of wavelengths, output energies, and pulse durations. Nevertheless, the discrete transitions of the rare earth elements used as dopant in the active medium limits the number of accessible wavelengths. Optical parametric oscillators (OPOs) overcome this problem since they deliver wavelengths that result from a frequency conversion in a nonlinear crystal. They allow to produce monochromatic light over a wide and continuous range of wavelengths from ultraviolet until infrared light. The generation of light between $3\,\mu$m and $12\,\mu$m is of particular interest for spectroscopic and military applications since the atmosphere is transparent in the $3-5\,\mu$m and $8-12\,\mu$m ranges. Even if OPOs are used today in many commercial devices, they still have drawbacks concerning the nonlinear crystal. First, the output energies are often limited by the size of the crystal aperture according to the intensity damage threshold. Secondly, the frequency conversion does not always preserve the pulse duration due to its limited spectral acceptance, and finally the output power of OPOs emitting light above $3\,\mu$m is severely limited because of the lack of well-suited nonlinear crystals.

The present work deals with the study of two nonlinear crystals for the infrared: periodically-poled 5%MgO:$LiNbO_3$ (5%MgO:PPLN) and $CdSiP_2$. The first one is already widely used in devices working until a wavelength of $5\,\mu$m. However, its refractive indices are not known with enough accuracy, which is detrimental for the design of OPOs. The second one is a new material that is promising for parametric generation until a wavelength of $12\,\mu$m. Its exhaustive linear and nonlinear properties are not known yet.
The first chapter presents the theoritical basis of linear and nonlinear optics that is necessary to the characterization of crystals. The second chapter explains the sphere method, which is

the chosen methodology allowing to fully characterize crystals. The third chapter concerns the measurements of the nonlinear properties of 5%MgO:PPLN: they led to a refinement of the previous and well established Sellmeier equations; furthermore, the recently proposed *angular quasi-phase-matching* scheme was verified by experiments and its relevance was discussed. The last chapter concerns the measurements of the nonlinear properties of $CdSiP_2$: the Sellmeier equations were refined, and its potentiality as a new nonlinear crystal for the infrared is discussed.

The Délégation Générale pour l'Armement provided the funding for this PhD thesis.

Chapter 1

Linear and nonlinear optical properties of uniaxial crystals

1.1 Introduction

This chapter gives the theoritical elements which are used in the next chapters. A first part is devoted to the linear and nonlinear optical properties of uniaxial crystals. The linear optical properties, based on the dielectric permittivity tensor, describe the propagation phenomena. The nonlinear optical properties describe quadratic parametric phenomena. Two ways to maximize the parametric generation efficiency are presented. The first one is birefringence phase-matching [1] and the second one is angular quasi-phase-matching [2].

1.2 Crystal linear optical properties

The equation that describes the propagation of an electromagnetic wave in a medium is obtained from Maxwell equations and the constitutive relations of this medium. We assume here that the medium is a homogeneous, non-conducting and non-magnetic crystal. However in an anisotropic crystal, the polarization vector $\vec{P}$ is not necessary in the direction of the electric vector $\vec{E}$ [3]. Then in the linear regime the electric susceptibility is a rank-two tensor so that each component of $\vec{P}$ at the angular frequency ω is linearly related to the components of $\vec{E}$, *i.e.* [3]:

$$\vec{P}(\omega) = \epsilon_0 \chi^{(1)}(\omega) \vec{E}(\omega) \tag{1.1}$$

where ϵ_0 is the free-space permittivity. $\chi^{(1)}(\omega)$ is called the first-order electric susceptibility tensor. In this work the imaginary part of $\chi^{(1)}$ is neglected since the present study is

restricted to the spectral regions where the crystals are transparent.
The wave propagation equation at the circular frequency ω is given by the following equation [3]:

$$\vec{\nabla} \times \vec{\nabla} \times \vec{E}(\omega) = \frac{\omega^2}{c^2}\vec{E}(\omega) + \omega^2 \mu_0 \vec{P}(\omega) \tag{1.2}$$

$\omega = 2\pi c/\lambda$ where λ is the wavelength and c is the velocity of light in vacuum; μ_0 is the free-space permeability. From inserting Eq. 1.1 in Eq. 1.2 we get:

$$\vec{\nabla} \times \vec{\nabla} \times \vec{E}(\omega) = \frac{\omega^2}{c^2}\epsilon(\omega)\vec{E}(\omega) \tag{1.3}$$

In this equation $\epsilon(\omega)$ is the *dielectric permittivity tensor* of the crystal defined as $\epsilon(\omega) = 1 + \chi^{(1)}(\omega)$. There is an orthonormal frame linked to the crystal in which the dielectric tensor is diagonal. This particular system is called *dielectric frame* which axes are called the *principal axes*, labeled (x, y, z). In the dielectric frame the dielectric permittivity tensor can be then written [4]:

$$\epsilon(\omega) = \begin{pmatrix} \epsilon_x & 0 & 0 \\ 0 & \epsilon_y & 0 \\ 0 & 0 & \epsilon_z \end{pmatrix} \tag{1.4}$$

According to the symmetry of the crystal structure, three optical classes of crystals are distinguished: the isotropic class is defined by $\epsilon_x = \epsilon_y = \epsilon_z$, the uniaxial class by $\epsilon_x = \epsilon_y \neq \epsilon_z$, and the biaxial class by $\epsilon_x \neq \epsilon_y \neq \epsilon_z$. The two crystals studied in this work, *i.e.* 5%MgO:PPLN and $CdSiP_2$, belong respectively to the trigonal and tetragonal lattice systems, and thus they belong to the uniaxial class.
The plane wave is a particular solution of Eq. 1.3. At a position $\vec{r}$ and angular frequency ω, it is given by [5]:

$$\vec{E}(\omega, \vec{r}, t) = \vec{e}(\omega)\, E(\omega, \vec{r})\, \exp[\pm i\vec{k} \cdot \vec{r}]\, \exp[-i\omega t] \tag{1.5}$$

where $\vec{e}(\omega)$ is the unit vector giving the direction of $\vec{E}$. $E(\omega, \vec{r})$ is the scalar complex amplitude that verifies $E^*(\omega, \vec{r}) = E(-\omega, \vec{r})$; $\vec{k}$ is the wavevector: $+\vec{k} \cdot \vec{r}$ corresponds to a forward propagation whereas $-\vec{k} \cdot \vec{r}$ corresponds to a backward propagation. In an uniaxial crystal there are two possible amplitudes, $\|\vec{k}^o\|$ and $\|\vec{k}^e\|$, for the wavevector in a given direction of unit vector $\vec{s}$:

$$\vec{k}^{o,e}(\omega, \theta, \phi) = \frac{\omega}{c}\, n^{o,e}(\omega, \theta, \phi)\, \vec{s}(\theta, \phi) \tag{1.6}$$

(θ, ϕ) are the angles of spherical coordinates of the direction $\vec{s}$ in the dielectric frame (x, y, z). At a given angular frequency ω, the refractive indices $n^o(\omega, \theta, \phi)$ and $n^e(\omega, \theta, \phi)$ are respectively the ordinary and the extraordinary refractive indices, defined in an uniaxial crystal as [3]:

$$n_x^2 = \epsilon_x \qquad n_y^2 = \epsilon_y \qquad n_z^2 = \epsilon_z$$

$$\begin{cases} n_o = n_x = n_y \\ n_e = n_z \end{cases} \tag{1.7}$$

$$\begin{cases} n^o(\theta, \phi) = n_o \\ n^e(\theta, \phi) = \left[\dfrac{\cos^2(\theta)}{n_o^2} + \dfrac{\sin^2(\theta)}{n_e^2} \right]^{-1/2} \end{cases}$$

n_o and n_e are the principal refractive indices at the frequency ω. The sign of the quantity $n_e - n_o$, which defines the birefringence, gives the sign of the optical class of the crystal: $n_e > n_o$ corresponds to the positive class, whereas $n_e < n_o$ corresponds to the negative class. The index surface represents the angular distribution of $n^o(\theta, \phi)$ and $n^e(\theta, \phi)$ in the dielectric frame. $n^o(\theta, \phi)$ is a sphere while $n^e(\theta, \phi)$ is an ellipsoid. Fig. 1.1 shows the index surface in the case of a negative uniaxial crystal in a quarter space of the dielectric frame. The principal refractive indices depend on the circular frequency ω; this dependency is given by the *Sellmeier's dispersion formula* $n_o(\omega)$ and $n_e(\omega)$ [6]. In an uniaxial crystal, the components of the ordinary and extraordinary unit electric field vectors $\vec{e}^{\,o}$ and $\vec{e}^{\,e}$ are [5]:

$$\begin{cases} e_x^o = -\sin(\phi) \\ e_y^o = \cos(\phi) \\ e_z^o = 0 \end{cases} \tag{1.8}$$

$$\begin{cases} e_x^e = -\cos\left[\theta \pm \rho(\theta, \omega)\right] \cos(\phi) \\ e_y^e = -\cos\left[\theta \pm \rho(\theta, \omega)\right] \sin(\phi) \\ e_z^e = \sin\left[\theta \pm \rho(\theta, \omega)\right] \end{cases} \tag{1.9}$$

with $-\rho$ for the positive class and $+\rho$ for the negative class. $\rho(\theta, \omega)$ is the double refraction angle representing the angle between the displacement vector $\vec{D}$ and the electric vector $\vec{E}$. Note that in uniaxial crystals, $\vec{e}^{\,e} \cdot \vec{e}^{\,o} = 0$ is always fulfilled.

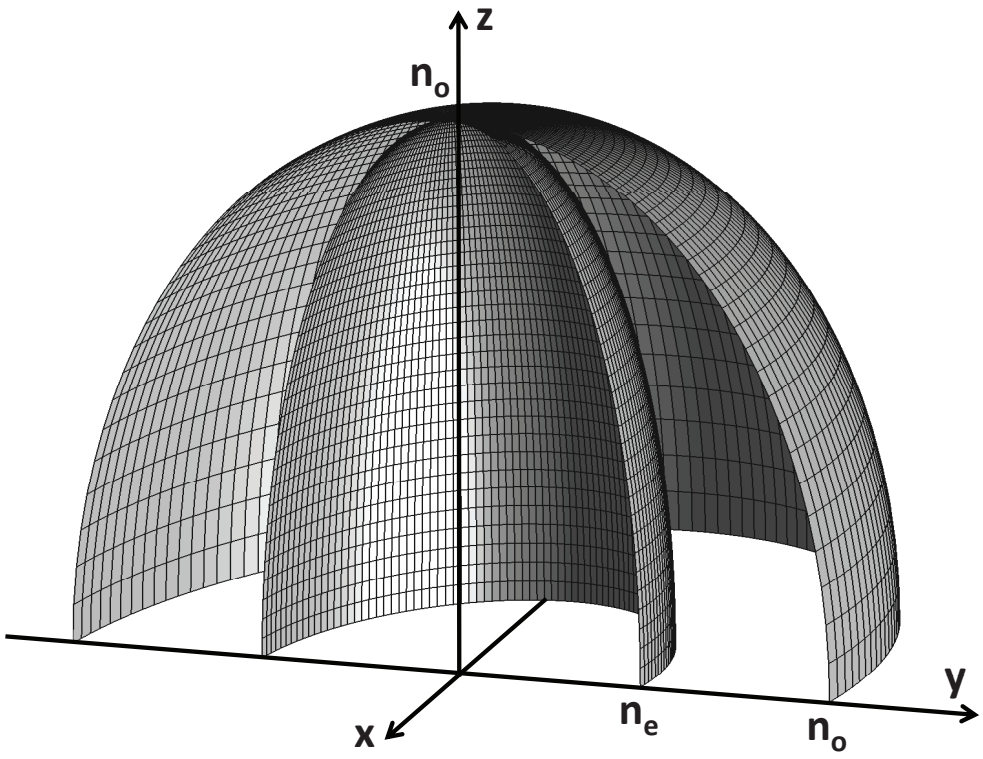

Figure 1.1: Index surface of a negative uniaxial crystal in the dielectric frame (x, y, z).

Finally, the energy flux is given by the Poynting vector [3]:

$$\vec{S}(\omega) = \vec{E}(\omega) \times \vec{H}(\omega) \tag{1.10}$$

Its modulus gives the power density expressed in $[W \cdot m^{-2}]$ [3]:

$$\|\vec{S}^{o,e}(\omega)\| = \frac{\|\vec{k}^{o,e}(\omega)\|}{2\,\mu_0\,\omega} \|\vec{E}^{o,e}(\omega)\|^2 \cos^2[\rho(\omega)] \tag{1.11}$$

Moreover it is important to notice that the Poynting vector and the wavevector do not necessary have the same direction. The angle between these two vectors is the double refraction angle, that can be written as:

$$\rho = \arccos\left[\frac{\vec{k}}{\|\vec{k}\|} \cdot \frac{\vec{S}}{\|\vec{S}\|}\right] \tag{1.12}$$

For an ordinary wave, $\rho = 0$ according to Eq. 1.8: the energy flow thus propagates in the direction of the wavevector. For an extraordinary wave, $\rho \neq 0$ in the general case according to Eq. 1.9, so that the energy flow does not propagate in the direction of the wavevector. Note that whatever ω, one has $\rho(\omega) = 0$ in any direction of the xy plane of an uniaxial crystal. The double refraction effect can be detrimental for parametric generation as explained later.

1.3 Equations of propagation in the nonlinear regime

We consider here the interaction between three electromagnetic waves at the circular frequencies $\omega_i = \omega_1$, ω_2 and ω_3 verifying the energy conservation:

$$\hbar\omega_1 + \hbar\omega_2 = \hbar\omega_3 \tag{1.13}$$

Such an interaction between waves with different circular frequencies is only possible in a noncentrosymmetric crystal and at high intensities that are accessible with lasers.
The Fourier component of the polarization vector at the circular frequency $\omega_i = \omega_1$, ω_2 or ω_3 is [1]:

$$\vec{P}(\omega_i) = \epsilon_0 \chi^{(1)}(\omega_i)\vec{E}(\omega_i) + \vec{P}^{(2)}(\omega_i) \tag{1.14}$$

$\vec{P}^{(2)}(\omega_i)$ is the second order nonlinear polarization defined as [1]:

$$\begin{cases} \vec{P}^{(2)}(\omega_1) = \epsilon_0 \chi^{(2)}(\omega_1) : \vec{E}(\omega_3) \otimes \vec{E}^*(\omega_2) \\ \vec{P}^{(2)}(\omega_2) = \epsilon_0 \chi^{(2)}(\omega_2) : \vec{E}(\omega_3) \otimes \vec{E}^*(\omega_1) \\ \vec{P}^{(2)}(\omega_3) = \epsilon_0 \chi^{(2)}(\omega_3) : \vec{E}(\omega_1) \otimes \vec{E}(\omega_2) \end{cases} \tag{1.15}$$

where ":" is the contraction product and "$\otimes$" is the tensor product. Eq. 1.15 shows the three possible processes allowed in a nonlinear crystal: sum-frequency generation between ω_1 and ω_2 written SFG ($\omega_3 = \omega_1 + \omega_2$), difference-frequency generation between ω_3 and ω_2 written DFG($\omega_1 = \omega_3 - \omega_2$), and difference-frequency generation between ω_3 and ω_1 written DFG($\omega_2 = \omega_3 - \omega_1$). The particular case of sum-frequency generation for which $\omega_1 = \omega_2 = \omega$ is called second-harmonic generation and is written SHG ($2\omega = \omega + \omega$). $\chi^{(2)}(\omega_i)$ is the second-order electric susceptibility tensor at the frequency ω_i. This rank three tensor has twenty-seven independent elements in the general case [5] and is represented by the

following matrix:

$$\chi^{(2)} = \begin{pmatrix} \chi_{xxx} & \chi_{xyy} & \chi_{xzz} & \chi_{xyz} & \chi_{xzy} & \chi_{xxz} & \chi_{xzx} & \chi_{xxy} & \chi_{xyx} \\ \chi_{yxx} & \chi_{yyy} & \chi_{yzz} & \chi_{yyz} & \chi_{yzy} & \chi_{yxz} & \chi_{yzx} & \chi_{yxy} & \chi_{yyx} \\ \chi_{zxx} & \chi_{zyy} & \chi_{zzz} & \chi_{zyz} & \chi_{zzy} & \chi_{zxz} & \chi_{zzx} & \chi_{zxy} & \chi_{zyx} \end{pmatrix} \tag{1.16}$$

The indices x, y, z refer to the dielectric frame. The orientation symmetry imposes some components to be equal to zero and also relations between the non-zero components of the tensor $\chi^{(2)}$. Furthermore, in case of low absorption at the considered frequencies, the Kleinman's conditions reduce more the number of independent non-zero components [5]. According to Eqs. 1.3 and 1.14, the propagation equation of each interacting wave is written [1]:

$$\vec{\nabla} \times \vec{\nabla} \times \vec{E}(\omega_i) = \frac{\omega_i^2}{c^2} \epsilon(\omega_i) \vec{E}(\omega_i) + \omega_i^2 \mu_0 \vec{P}^{(2)}(\omega_i) \tag{1.17}$$

where $i = 1, 2 \text{ or } 3$. The three propagation equations are coupled by the Fourier components of the nonlinear polarization $\vec{P}^{(2)}(\omega_1)$, $\vec{P}^{(2)}(\omega_2)$ and $\vec{P}^{(2)}(\omega_3)$ given by Eq. 1.15, which leads to a variation of the three complex amplitudes $E(\omega_i)$ along the direction of propagation. In the slowly varying envelope approximation, which corresponds to a small variation of the wave amplitudes over one wavelength λ_i, it comes in the case of three collinear waves [1]:

$$\begin{cases} \dfrac{\partial E(\omega_1)}{\partial Z} = j\kappa_1 E(\omega_3) E^*(\omega_2) \exp(j\Delta k \cdot Z) \\ \dfrac{\partial E(\omega_2)}{\partial Z} = j\kappa_2 E(\omega_3) E^*(\omega_1) \exp(j\Delta k \cdot Z) \\ \dfrac{\partial E(\omega_3)}{\partial Z} = j\kappa_3 E(\omega_1) E(\omega_2) \exp(-j\Delta k \cdot Z) \end{cases} \tag{1.18}$$

Z stands for the spatial coordinate along the direction of propagation of the three waves described by the unit vector $\vec{s}$. The parameter Δk is the phase-mismatch between the nonlinear polarization $\vec{P}^{(2)}(\omega_i)$ and the radiated field $\vec{E}(\omega_i)$, defined in the collinear case by:

$$\Delta k = k(\omega_3) - k(\omega_1) - k(\omega_2) \tag{1.19}$$

$\kappa_i = \dfrac{\pi \chi_{\text{eff}}}{n_i \lambda_i}$, where n_i is the refractive index of the wave at λ_i in the considered direction of propagation, and χ_{eff} is the effective coefficient defined as [5]:

$$\chi_{\text{eff}} = \sum_{ijk} F_{ijk}\chi_{ijk}(\omega_3) = \sum_{jik} F_{jik}\chi_{jik}(\omega_1) = \sum_{kij} F_{kij}\chi_{kij}(\omega_2) \tag{1.20}$$

for SFG (ω_3), DFG (ω_1) and DFG (ω_2) respectively.
F_{abc} stands for the twenty seven coefficients of the field tensor defined by [5]:

$$F_{ijk} = F_{jik} = F_{kij} = e_i(\omega_3)e_j(\omega_1)e_k(\omega_2) \tag{1.21}$$

where e_i, e_j and e_k are the Cartesian coordinates of the unit electric field vectors of the interacting waves. Each of them can correspond to the coordinates of $\vec{e}^{\,o}$ or $\vec{e}^{\,e}$ given by Eqs. 1.8 and 1.9. Then the effective coefficient χ_{eff} is a linear combination of the components of χ and F.

1.4 Conversion efficiency

The general solution of the three coupled equations 1.18 are Jacobi's elliptic functions [1]. The resolution is easier if the variation of two of the three amplitudes can be neglected: it is the so-called undepleted pump approximation. It corresponds for example to $\partial E_1/\partial Z = \partial E_2/\partial Z = 0$ in the case of SFG($\omega_3 = \omega_1 + \omega_2$). Then the power of the generated wave at ω_3 with respect to the length $Z = L$ of the crystal along the direction of propagation under this approximation becomes [1]:

$$\mathcal{P}^{\omega_3}(L) \propto \chi^2_{\text{eff}}\, I^{\omega_1}(0)\, I^{\omega_2}(0)\, L^2\, \text{sinc}^2\left(\frac{\Delta k \cdot L}{2}\right) \tag{1.22}$$

Eq. 1.22 shows that when $\Delta k \neq 0$ there is a reversal of the energy flow between the interacting waves every *coherence length* defined as $L_c = \pi/\Delta k$, as shown in Fig. 1.2. This situation is not interesting form the conversion efficiency point of view, contrary to the case where $\Delta k = 0$ for which the generated power reaches a maximum. This interesting situation can be achieved thanks to different techniques described below.

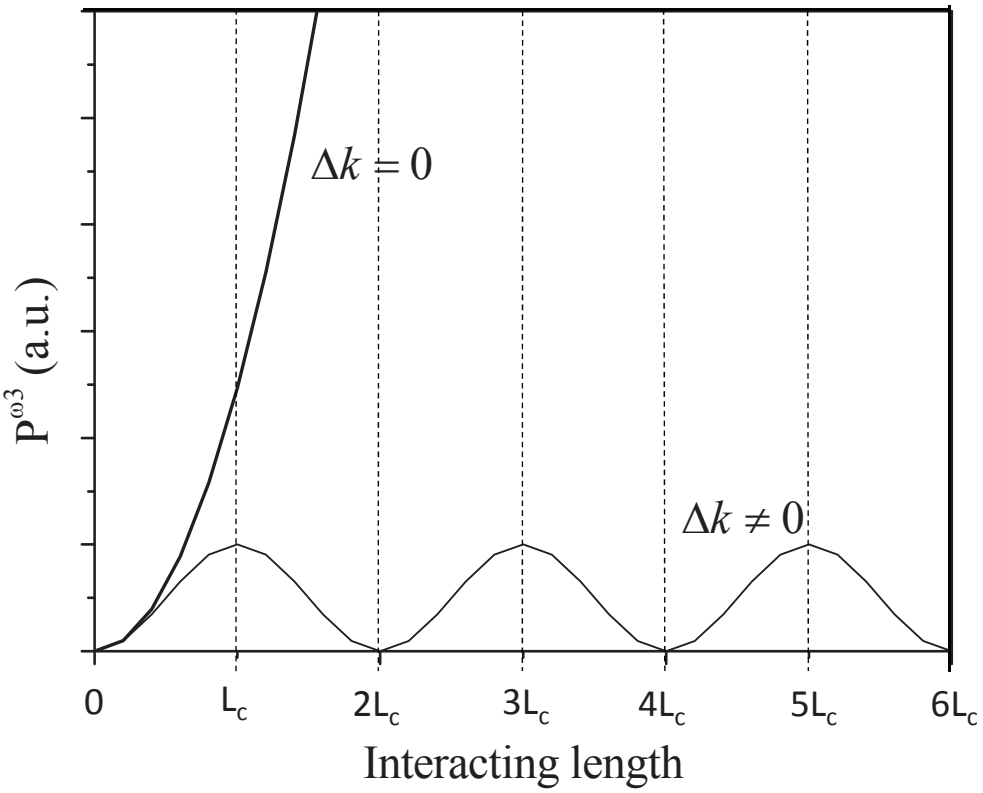

Figure 1.2: Evolution of the power of the generated parametric wave as a function of the interacting length in the cases of non phase-matching condition ($\Delta k \neq 0$) and birefringence phase-matching (BPM) corresponding to $\Delta k = 0$. L_c is the coherence length of the considered parametric interaction.

1.5 Birefringence phase-matching

1.5.1 Momentum conservation

The energy transfer between the waves is maximum for $\Delta k = 0$, which corresponds to the phase-matching between the nonlinear polarization and the radiated field. If this condition is fulfilled, the energy flow does not alternate in sign and the power of the generated field grows continuously as the square of the interacting length L according to Eq. 1.22, and as shown in Fig. 1.2.

Note that from the point of view of the quantum theory of light, the phase-matching condition corresponds to the total photon-momentum conservation. Moreover, the energy

conservation given by Eq. 1.13 is always verified and is equivalent to:

$$\frac{1}{\lambda_1} + \frac{1}{\lambda_2} = \frac{1}{\lambda_3} \tag{1.23}$$

where $\lambda_i = 2\pi c/\omega_i$ $(i = 1, 2, 3)$ is the wavelength in vacuum of the interacting wave i. According to Eqs. 1.6 and 1.19, the phase-matching condition can be expressed as a function of the refractive indices in a considered direction of propagation $\vec{s}\,(\theta, \phi)$:

$$\Delta k_{\mathrm{BPM}} = 2\pi \left[\frac{n(\lambda_3, \theta, \phi)}{\lambda_3} - \frac{n(\lambda_1, \theta, \phi)}{\lambda_1} - \frac{n(\lambda_2, \theta, \phi)}{\lambda_2} \right] = 0 \tag{1.24}$$

where BPM stands for birefringence-phase-matching. The phase-matching condition would be always verified in a hypothetical non dispersive medium, where $n(\lambda_1) = n(\lambda_2) = n(\lambda_3)$. Indeed in this case, Eq. 1.24 reduces to energy conservation (Eq. 1.23). In realistic situations, any medium is dispersive so that $n(\lambda_1) \neq n(\lambda_2) \neq n(\lambda_3)$. However, birefringency can be used to compensate the dispersion, since each refractive index can take two possible values: $n^o(\theta, \phi)$ and $n^e(\theta, \phi)$ given by Eq. 1.7. This technique is called birefringence phase-matching (BPM). Consequently, there are 2^3 possible combinations of indices in Eq. 1.24 [5].

1.5.2 BPM types

Only three combinations among the 2^3 are compatible with the wavelength dispersion and with the momentum and energy conservation [5]. These three possible combinations are designated as *types* I, II and III, according to the polarization states of the three frequencies. They are defined in table 1.1 [7].

Momentum conservation relation	Interaction type		
	SFG (ω_3)	DFG (ω_1)	DFG (ω_2)
$\omega_3 n_3^- = \omega_1 n_1^+ + \omega_2 n_2^+$	I	II	III
$\omega_3 n_3^- = \omega_1 n_1^- + \omega_2 n_2^+$	II	III	I
$\omega_3 n_3^- = \omega_1 n_1^+ + \omega_2 n_2^-$	III	I	II

Table 1.1: Definition of interaction types versus phase-matching relations according to sum-frequency generation (SFG) and difference-frequency generation (DFG); $(n^+, n^-) = (n^e, n^o)$ in the case of a positive uniaxial crystal, and $(n^+, n^-) = (n^o, n^e)$ for a negative optical sign.

To each type corresponds a specific configuration of polarization. As an example for SFG: (e_1^+, e_2^+, e_3^-) for type I, (e_1^-, e_2^+, e_3^-) for type II and (e_1^+, e_2^-, e_3^-) for type III. Note that types II and III are equivalent in the case of second-harmonic generation since $\omega_1 = \omega_2$.

1.5.3 BPM loci

The phase-matching angles, written $(\theta_{\mathrm{BPM}}, \phi_{\mathrm{BPM}})$, are the solutions of Eq. 1.24. They define the BPM directions. In uniaxial crystals, there is no influence of the spherical angle ϕ on the refractive indices according to Eq. 1.7. As a consequence, the loci of the BPM directions of types I, II and III are always cones around the z-axis, as represented in Fig. 1.3. However, the angle ϕ can have an influence on the effective coefficient χ_{eff} through the field factor (Eqs. 1.20 and 1.21) and thus on the power of the generated wave.

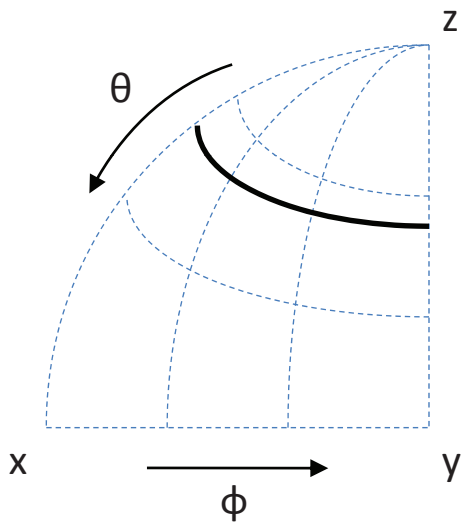

Figure 1.3: BPM loci forming a cone around the z-axis (bold line) represented in a Wülf diagram. (θ, ϕ) are the angles of spherical coordinate in the dielectric frame (x, y, z).

The main drawback of BPM is that it does not allow to access to all the coefficients of the second order electric susceptibility tensor [5]. In particular in any ferroelectric crystal the highest coefficient χ_{zzz} cannot be purely sollicitated by BPM.

1.6 Quasi-phase-matching and angular quasi-phase-matching

1.6.1 Quasi-phase-matching

Another technique enabling to increase the conversion efficiency of a parametric process is to use a medium having a periodic change in sign of the second-order electric susceptibility, with a periodicity twice the coherence length of the considered process [1, 8]. This method is called *quasi-phase-matching* (QPM) when the direction of propagation of the waves is along the grating vector, as shown in Fig. 1.4.

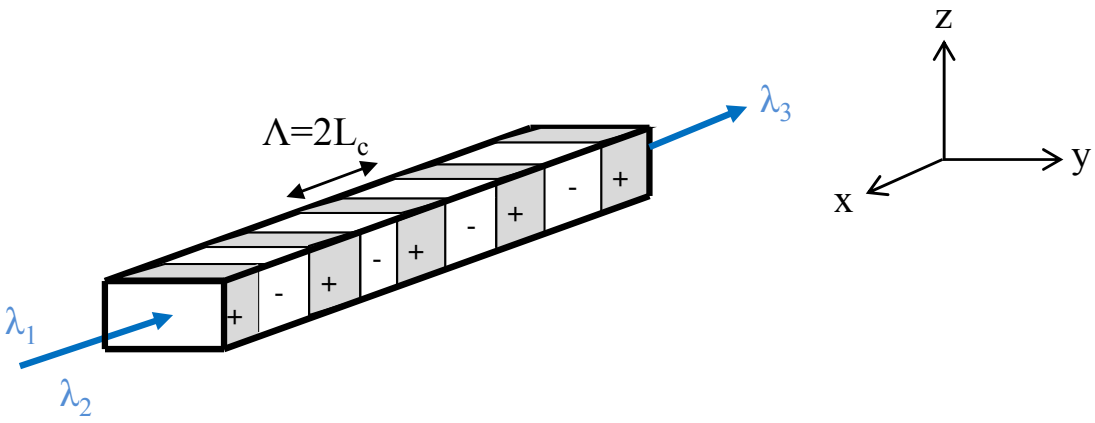

Figure 1.4: Scheme of QPM where Λ is the inverting periodicity along the x-axis of the dielectric frame (x, y, z). λ_3 is the wavelength of the generated wave verifying the energy conservation condition $\lambda_3^{-1} = \lambda_1^{-1} + \lambda_2^{-1}$. L_c is the coherence length of the considered parametric process. "+" and "-" signs stand for $+\chi_{\text{eff}}$ and $-\chi_{\text{eff}}$.

By taking an inversion period equal to the coherence length $L_c = \pi/\Delta k$ of the considered parametric interaction, it is possible to keep a constructive interference along the propagation direction, due to the π shift reset from a coherence length to the following one, as shown in Fig. 1.5. Since the direction of propagation is along x, we get $\theta = 90°$ and $\phi = 0°$ and the momentum conservation can be written [1]:

$$\Delta k_{\text{QPM}} = 2\pi \left[\frac{n_{o,e}(\lambda_3)}{\lambda_3} - \frac{n_{o,e}(\lambda_1)}{\lambda_1} - \frac{n_{o,e}(\lambda_2)}{\lambda_2} \right] - \frac{2\pi}{\Lambda} = 0 \tag{1.25}$$

where n_o and n_e are the ordinary and extraordinary principal refractive indices. The expression of the conversion efficiency corresponding to QPM is given by Eq. 1.22 multiplied

by a factor $4/\pi^2$ [8], as shown in Fig. 1.5.

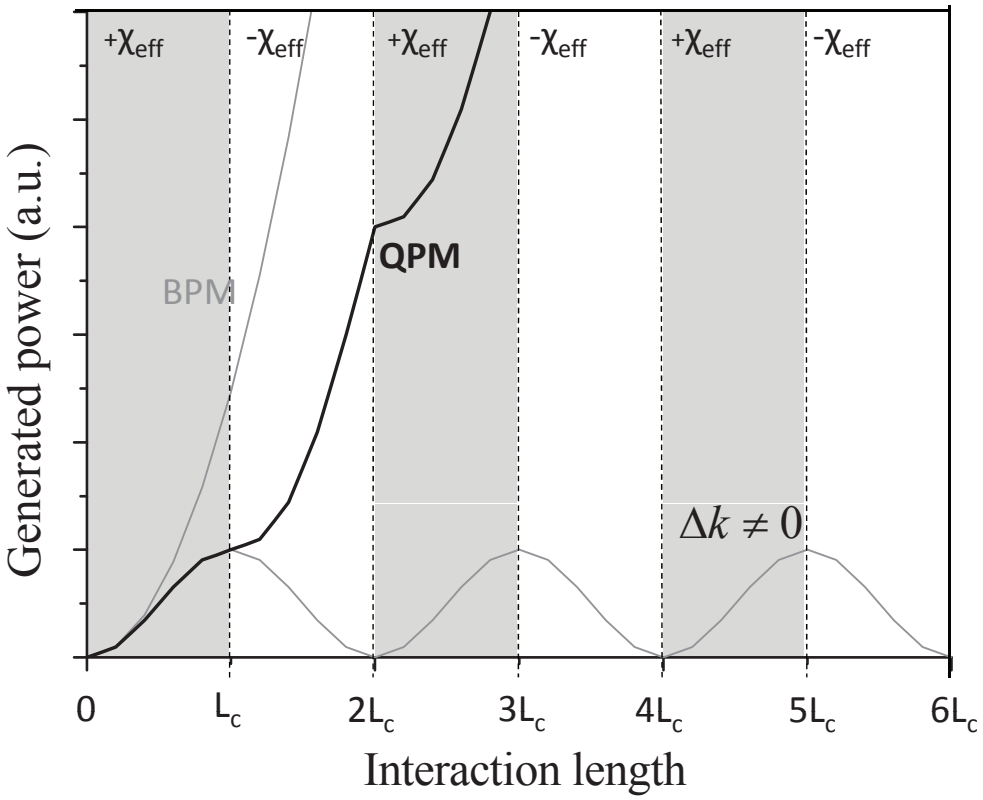

Figure 1.5: Evolution of the power of the generated wave as a function of the interacting length in the cases of non phase-matching condition ($\Delta k \neq 0$), birefringence phase-matching (BPM) and quasi-phase-matching (QPM). χ_{eff} is the effective coefficient of the considered parametric process. L_c is the coherence length of the considered parametric interaction.

Thanks to the contribution of the wavevector associated to the periodic structure, it is possible to choose any of the 8 possible configurations of polarization, given in table 1.2, whereas BPM only allows three of them [2].

Momentum conservation relation	Interaction type		
	SFG (ω_3)	DFG (ω_1)	DFG (ω_2)
$\omega_3 n_3^- = \omega_1 n_1^+ + \omega_2 n_2^+ + 1/\Lambda_{\text{eff}}$	I	II	III
$\omega_3 n_3^- = \omega_1 n_1^- + \omega_2 n_2^+ + 1/\Lambda_{\text{eff}}$	II	III	I
$\omega_3 n_3^- = \omega_1 n_1^+ + \omega_2 n_2^- + 1/\Lambda_{\text{eff}}$	III	I	II
$\omega_3 n_3^- = \omega_1 n_1^- + \omega_2 n_2^- + 1/\Lambda_{\text{eff}}$	IV	IV	IV
$\omega_3 n_3^+ = \omega_1 n_1^+ + \omega_2 n_2^+ + 1/\Lambda_{\text{eff}}$	V	V	V
$\omega_3 n_3^+ = \omega_1 n_1^- + \omega_2 n_2^+ + 1/\Lambda_{\text{eff}}$	VI	VIII	VII
$\omega_3 n_3^+ = \omega_1 n_1^+ + \omega_2 n_2^- + 1/\Lambda_{\text{eff}}$	VII	VI	VIII
$\omega_3 n_3^+ = \omega_1 n_1^- + \omega_2 n_2^- + 1/\Lambda_{\text{eff}}$	VIII	VII	VI

Table 1.2: Definition of interaction types as a function of the relations of momentum conservation of QPM or AQPM according to sum-frequency generation (SFG) and difference-frequency generation (DFG); Λ_{eff} is the effective grating period of QPM or AQPM.

1.6.2 Angular quasi-phase-matching

In a previous work, it was shown that it is possible to generalize QPM by considering any angle of propagation with respect to the grating vector of the periodic structure. This general scheme was called *angular quasi-phase-matching* (AQPM) [2, 9]. In the following, any direction of propagation $\vec{s}$ is represented by its angles of spherical coordinates (θ, ϕ) in the dielectric frame, as shown in Fig. 1.6.

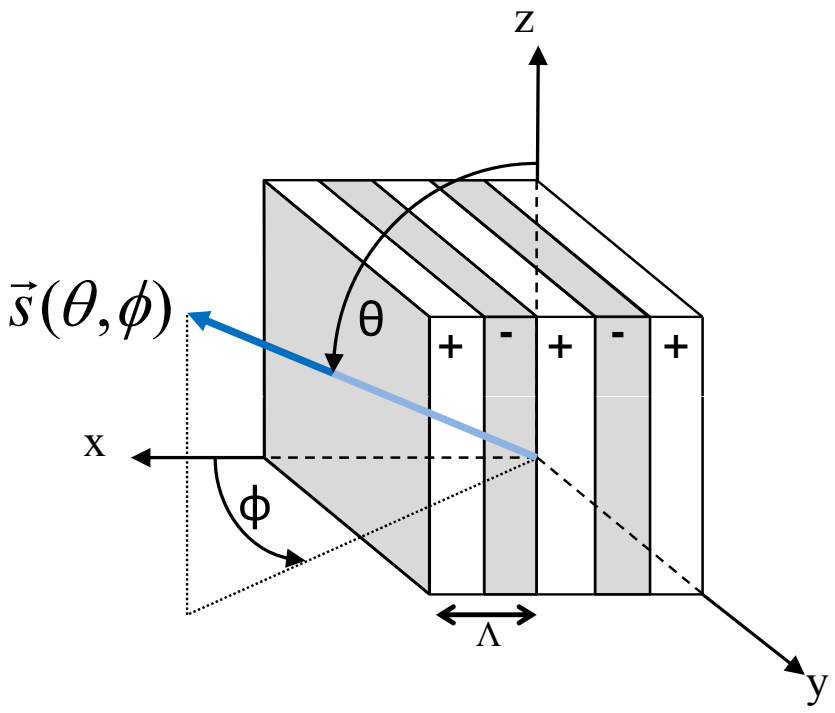

Figure 1.6: Scheme of AQPM in a periodically-poled medium. Λ is the inverting periodicity along the x-axis. $\vec{s}$ is the unit wave vector of the interacting waves with the coordinates (θ, ϕ) in the dielectric frame (x, y, z).

Then in the configuration of AQPM, the right grating period that has to be considered is along the $\vec{s}$ vector, as shown in Fig. 1.7; it is expressed by the following equation in the linear geometry:

$$\Lambda_{\text{eff}}(\theta, \phi) = \left| \frac{\Lambda}{\sin(\theta)\ \cos(\phi)} \right| \tag{1.26}$$

Moreover, the refractive indices depend on the direction of propagation as shown in Fig. 1.7. The momentum conservation condition of QPM (Eq. 1.25) can thus be generalized in

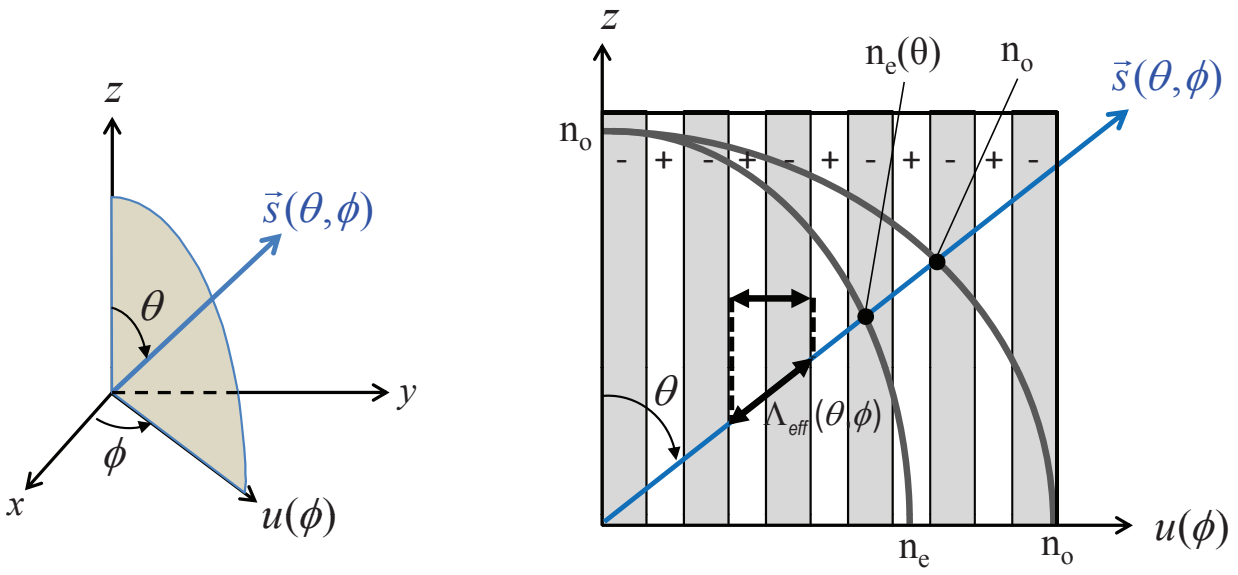

Figure 1.7: AQPM in the direction of propagation $\vec{s}$ with the angles of spherical coordinates (θ, ϕ) in a periodically-poled medium. The two curves correspond to the section of the index surface of a negative uniaxial crystal defined by the z-axis and the direction $u(\phi)$ contained in the xy plane. n_o and n_e are the ordinary and extraordinary principal refractive indices. Λ is the grating periodicity along the x-axis. $\Lambda_{\text{eff}}(\theta, \phi)$ is the effective grating periodicity along the direction (θ, ϕ).

the case of AQPM by taking into account the angular tunability of both the grating and the birefringence, leading to the following equation:

$$\Delta k_{\text{AQPM}} = 2\pi \left[\frac{n(\lambda_3, \theta, \phi)}{\lambda_3} - \frac{n(\lambda_1, \theta, \phi)}{\lambda_1} - \frac{n(\lambda_2, \theta, \phi)}{\lambda_2} \right] - \frac{2\pi}{\Lambda_{\text{eff}}(\theta, \phi)} = 0 \tag{1.27}$$

θ and ϕ are the angles of spherical coordinates of the direction of propagation in the dielectric frame (x, y, z). λ_1, λ_2 and λ_3 are the wavelengths of the interacting waves; $n(\lambda_i, \theta, \phi)$ with $i = 1, 2, 3$ are the corresponding refractive indices in the considered direction (θ, ϕ). $\Lambda_{\text{eff}}(\theta, \phi)$ is the effective grating periodicity in the direction (θ, ϕ) defined by Eq. 1.26: it ranges from Λ along the x-axis to infinity when the propagation occurs in the yz plane. Note that this latest case corresponds to BPM, for which there is no grating.

1.6.3 AQPM types

As for QPM, due to the implication of Λ_{eff} in Eq. 1.27, AQPM authorizes the 8 possible refractive indices combinations. These 8 types are defined in the same way as QPM ones

and are given in table 1.2.

1.6.4 AQPM loci

The determination of the AQPM directions $(\theta_{\text{AQPM}}, \phi_{\text{AQPM}})$ can be performed by numerically solving Eq. 1.27, according to the grating period of the medium, the set of considered wavelengths and the corresponding refractive indices. In uniaxial media, the loci of directions corresponding to the eight AQPM types are distributed over cones that can exhibit three possible topologies as shown in Fig. 1.8 using a Wülf diagram representation [2].

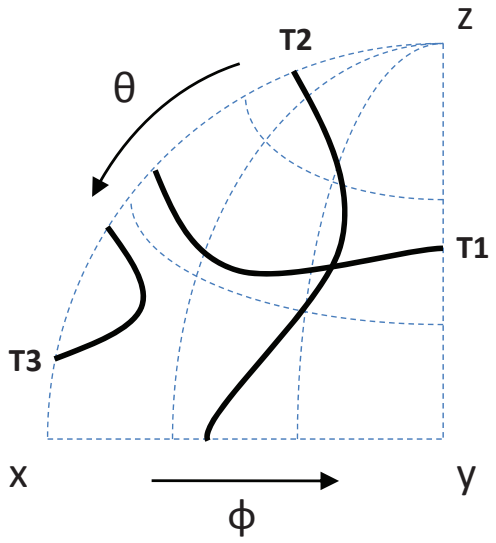

Figure 1.8: The three possible topologies **T1**, **T2** and **T3** of AQPM loci represented in a Wülf diagram for uniaxial media. θ and ϕ are the angles of spherical coordinates of any direction of propagation in the dielectric frame (x,y,z).

The three AQPM topologies of Fig. 1.8 are different that the one of BPM given in Fig. 1.3, but they are similar to those of BPM in biaxial crystals, which put in emphasis the breaking of the uniaxial symmetry by the inversion grating [2].

1.7 Acceptances

The interference function $\text{sinc}^2(\Delta kL/2)$ of Eq. 1.22 is maximum for $\Delta k = 0$ in a given direction $(\theta_{\text{PM}}, \phi_{\text{PM}})$ and at a given set of wavelengths $(\lambda_{1\text{PM}}, \lambda_{2\text{PM}}, \lambda_{3\text{PM}})$, where the index PM stands for either BPM, QPM or AQPM phase-matching. It is important to quantify

the consequence of a variation of Δk from 0, due to variations of wavelength $\lambda_{i\mathrm{PM}} \pm d\lambda_i$ with $i = (1, 2, 3)$, or angles, $\theta_{\mathrm{PM}} \pm d\theta$ and $\phi_{\mathrm{PM}} \pm d\phi$. Note that Δk can also depend on the temperature, due to the thermooptical effect. The acceptance bandwidth is defined from the deviation $\delta\xi$ of the dispersive parameter ξ ($\xi = \lambda, \theta, \phi$) leading to a phase-mismatch variation Δk from 0 to $2\pi/L$, where L is the crystal length as shown in Fig. 1.9 [5].

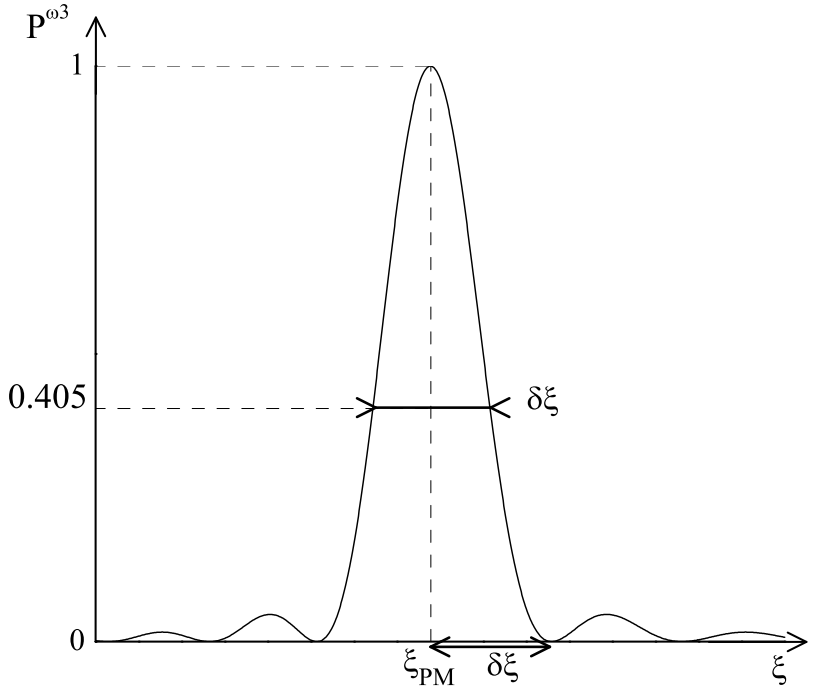

Figure 1.9: Generated power P^{ω_3} as a function of any dispersive parameter ξ of the refractive indices. ξ_{PM} is the value allowing phase-matching; $\delta\xi$ is the full-width of the curve at 0.405 of the maximum, corresponding to a phase-mismatch $\Delta k = 2\pi/L$ where L is the crystal length.

The acceptance bandwidth can be calculated by expanding Δk in Taylor series about ξ [5]:

$$\frac{2\pi}{L} = \Delta k = \left.\frac{\partial(\Delta k)}{\partial \xi}\right|_{\xi_{\mathrm{PM}}} \delta\xi + \frac{1}{2}\left.\frac{\partial^2(\Delta k)}{\partial \xi^2}\right|_{\xi_{\mathrm{PM}}} (\delta\xi)^2 + \ldots \tag{1.28}$$

The acceptance bandwidth is then given by the product $L \cdot \delta\xi$: $\xi = \lambda_i$ corresponds to the spectral acceptance relative to λ_i; $\xi = \theta_{\mathrm{PM}}$ or ϕ_{PM} corresponds to the angular acceptances. This approach is relevant for BPM, QPM and AQPM, the corresponding mismatch parameters Δk being given by Eq. 1.24, Eq. 1.25 and Eq. 1.27 respectively.

1.7.1 Spectral acceptance

The BPM or AQPM tuning curves have the same generic appearance given in Fig. 1.10(a) [2], exhibiting a vertical tangent (point A) corresponding to propagation angle θ_A. This situation is of prime importance because the associated spectral acceptance reaches its maximal value, which is termed as a spectrally non critical phase-matching (NCPM). This situation is also illustrated in Fig. 1.11 where Δk is plotted as a function of λ. A spectrally NCPM corresponds to the cancellation of the first term of the expansion of Δk in Eq. 1.28, *i.e.*:

$$\left.\frac{\partial(\Delta k)}{\partial\lambda}\right|_{\lambda_A} = 0 \tag{1.29}$$

It can be shown that Eq. 1.29 is equivalent to the group velocity matching between two of the three interacting waves [10]. Thus, at the particular wavelength λ_A, both the phase velocities and the group velocities are matched. The value of the spectral acceptance $L\delta\lambda$ in this case is maximal, given by the following equation according to Eqs. 1.28 and 1.29:

$$L\delta\lambda = \sqrt{4\pi L}\left(\left.\frac{\delta^2\Delta k}{\delta\lambda^2}\right|_{\lambda_A}\right)^{-1/2} \tag{1.30}$$

For applications that require a large spectral bandwidth, it is useful to be able to vary the particular wavelength λ_A. In the case of BPM and QPM, there usually exists a unique wavelength that fulfills both these conditions, that is fixed by the spectral dispersion of the refractive indices of the crystal. Different schemes have been proposed to enable such a variation of these particular wavelength: by tailoring the material dispersion thanks to an appropriate doping level [10], by temperature tuning [11], or by using non-collinear interactions [12]. It will be shown in the next chapter that AQPM allows an angular tunability of the non critical wavelength λ_A.

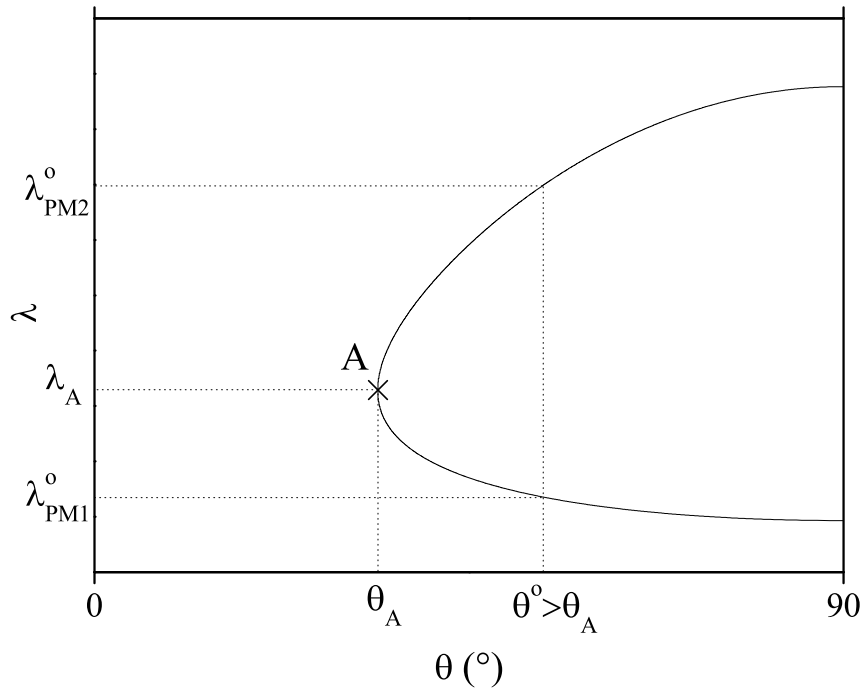

(a)

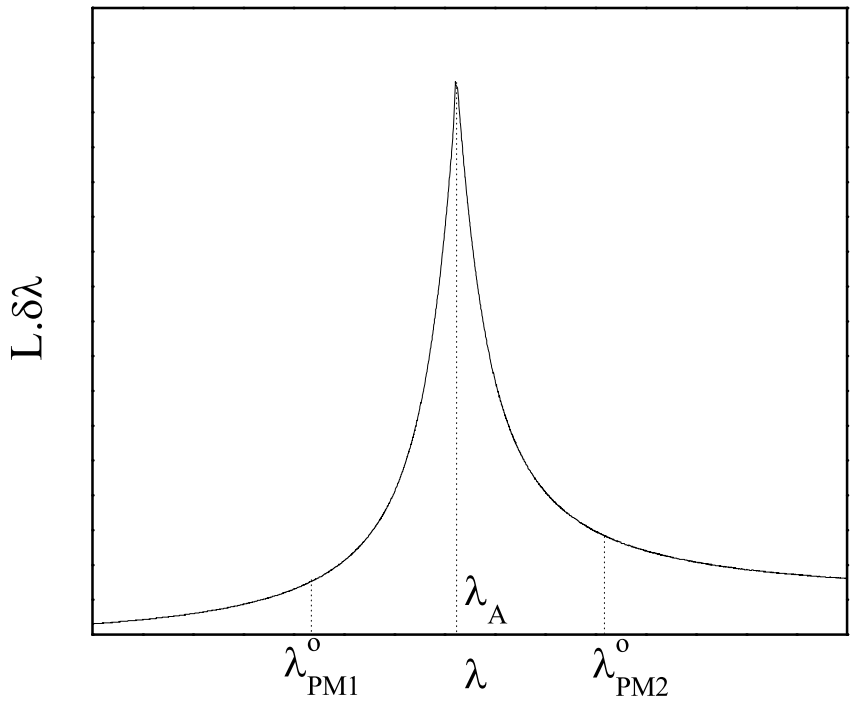

(b)

Figure 1.10: Typical BPM or AQPM tuning curve in a $\phi = \text{cte}$ plane of the crystal (a), and its associated spectral acceptance $L\delta\lambda$ (b). λ stands for λ_1 or λ_2 for SFG(λ_3), λ_3 or λ_2 for DFG(λ_1), and λ_3 or λ_2 for DFG(λ_2). λ_{PM1} and λ_{PM2} are two particular wavelengths. Point A corresponds to the wavelength λ_A and the angle θ_A for which the spectral acceptance is maximal. λ^o_{PM1} and λ^o_{PM2} are two wavelengths corresponding to the same phase-matching angle θ^o.

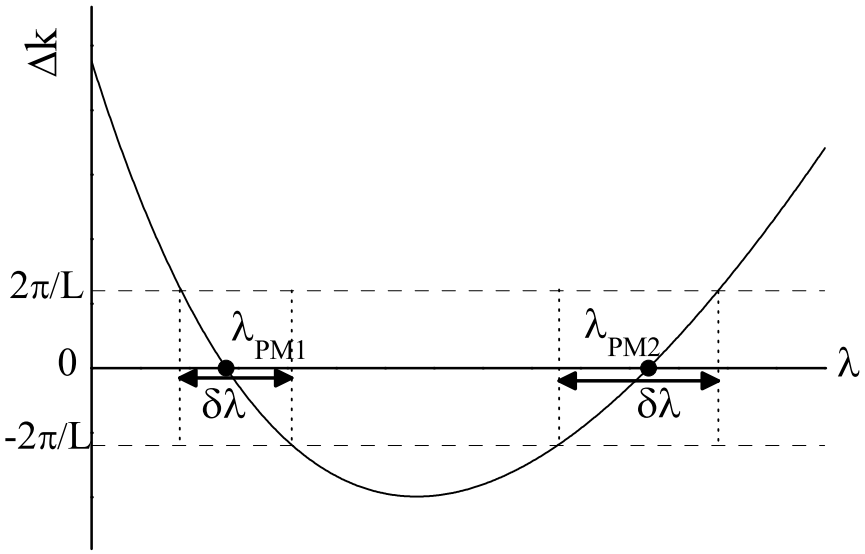

(a)

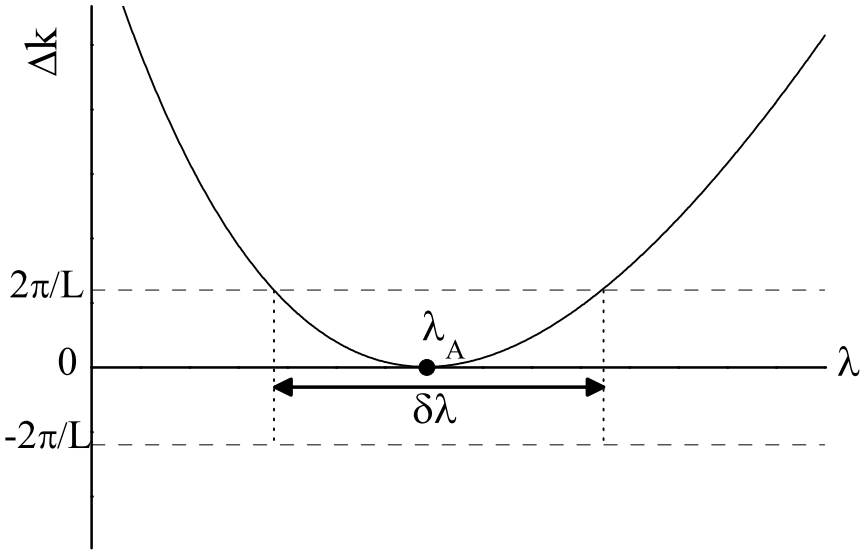

(b)

Figure 1.11: Phase-mismatch Δk as a function of λ at $\theta > \theta_A$ (a) and $\theta = \theta_A$ (b), where point A, λ_A, PM1 and PM2 are defined in Fig. 1.10; $\delta\lambda$ corresponds to a phase-mismatch $\Delta k = 2\pi/L$ where L is the crystal length.

1.7.2 Angular acceptances

In the case of BPM in uniaxial crystals, the refractive indices do not vary in ϕ leading to an infinite ϕ angular acceptance bandwidth ($L\delta\phi \rightarrow \infty$). $\delta\theta$ is then the only one to be considered [5]. The case of AQPM is different, the angular bandwidth in ϕ being not infinite anymore as it is explained in the next chapter.

1.8 Conclusion

The theoritical basis given in this chapter are useful for understanding the experimental work presented in the next chapters.

Chapter 2

Optical characterization using the sphere method

2.1 Introduction

This chapter presents the experimental method called the "sphere method", which was used to study the exhaustive optical properties of 5%MgO:PPLN and $CdSiP_2$ crystals cut as spheres. Since the experiment requires a quasi-parallel propagation inside the spheres, it could not have been carried out without calculations using Gaussian optics detailed hereafter.

2.2 State of the art

The exhaustive study of the nonlinear optical properties of an anisotropic crystal requires an access to a maximum of directions of propagation inside the medium with laser beams able to deliver a range of wavelengths covering the whole transparency range of the studied material. It would thus require a huge number of parallelepipedic samples cut and polished in different directions. However, it is often not compatible with the small volume of matter that is usually available at the first steps of crystal growth. In order to overcome this difficulty, the "sphere method" was proposed and developed by our group since 1989 [13]. This technique consists in cutting and polishing the crystal as a sphere, which allows laser beams to propagate in any direction of the crystal while keeping normal incidence. We have the technical know-how for fabricating spheres of diameter down to less than 4 mm with an asphericity better than 1%. This technique enables to directly measure any phase-matching

direction with an accuracy better than 0.5°, and the associated conversion efficiency, spectral and internal angular acceptances. The sphere method was successfully applied in the past to the study of several crystals as KTP [14], RTP [15], KTA [16], RTA [16], CTA [16], YCOB [17] and Nd:YCOB [18] in their whole transparency range. According to the required tunability of the incident beam, optical parametric oscillators (OPO) or optical parametric generators (OPG) are ideal sources to carry out the measurements on the sphere.

2.3 Experimental setup

The optical source we used is a multi-stages parametric source from Excel Technology and Light Conversion, detailed in Fig. 2.1.

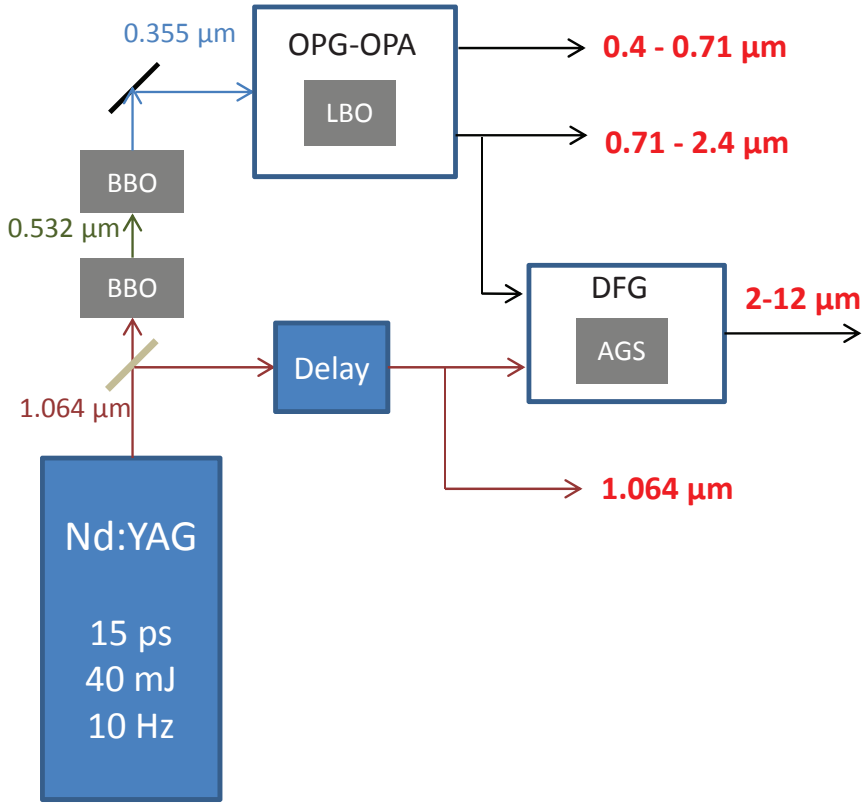

Figure 2.1: Scheme of the parametric source used for the sphere experiments.

The pump is a Nd:YAG laser emitting pulses of FWHM pulse duration of 15 ps at 1.064 μm with a repetition rate of 10 Hz. The energy per pulse at 1.064 μm is 40 mJ. This beam is divided in two parts: 10 mJ go directly in the direction of a difference-frequency generation

(DFG) stage while 30 mJ go first in the direction of an OPG-OPA stage. After doubling and tripling of 1.064 μm in two BBO crystals, pulses at 355 nm are produced with an energy of 8 mJ. These pulses are used for pumping the OPG-OPA stage based on a crystal of LBO of which rotation is motorized and controlled by computer. This OPG-OPA stage delivers a beam where the signal wavelength λ_s can be tuned between 0.40 μm and 0.71 μm, corresponding to a tunability of the idler wavelength between 2.40 μm and 0.71 μm respectively. The energy of these pulses depends on the considered wavelength, and is around 200 μJ. Finally, a DFG between the idler and the pulse at 1.064 μm is realized in a crystal of $AgGaS_2$ (AGS) thanks to a non collinear interaction in order to produce a tunable wavelength between 2 μm and 12 μm.

The measurement setup must enable the study of sum-frequency generation (SFG), second-harmonic generation (SHG) and difference-frequency generation (DFG) in any direction of the studied crystal cut as a sphere. SFG and DFG require two incident beams with perfect spatial and temporal overlaps, while SHG measurements only require one incident beam that is tunable in wavelength. In the first cases, one of the two beams was taken at 1.064 μm, the other one being at the signal or idler wavelength. An example of a typical experimental setup for DFG is shown in Fig. 2.2.

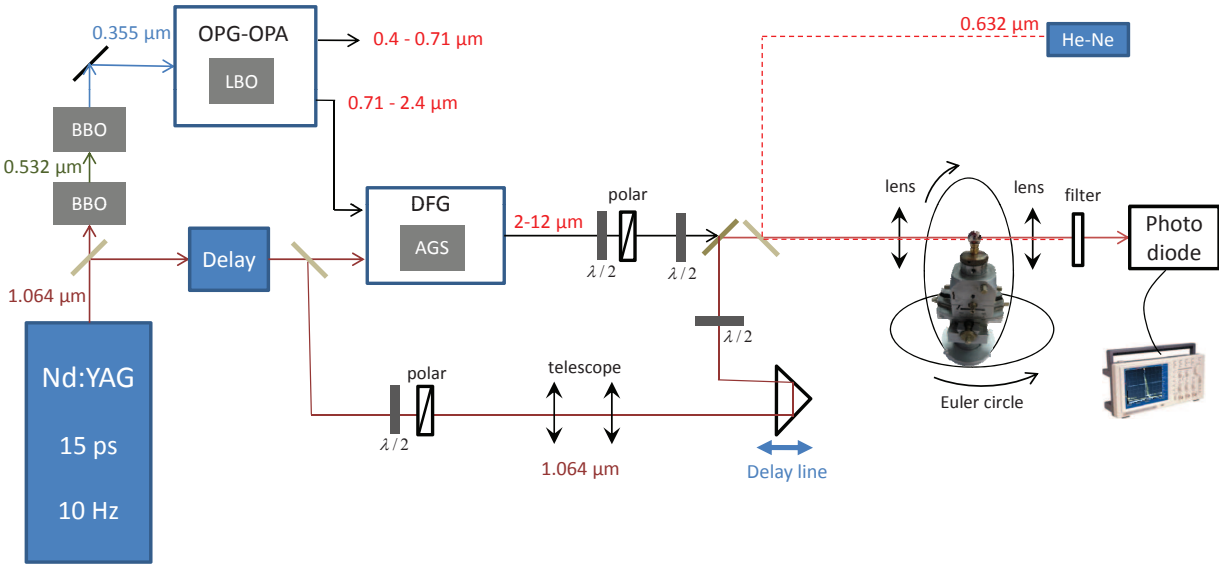

Figure 2.2: Example of the experimental setup aimed at studying SFG in a sphere between a beam at 1.064 μm and an infrared beam tunable between 2 and 12 μm.

The energy of each incident beam was controlled by the association of a half-wave plate and a Glan-Taylor prism. The polarization state of each beam was then controlled by the half-wave plates. A telescope using two convergent lenses allowed the radius of the Nd:YAG beam to be adjusted to the one of the infrared beam, and a delay line allowed to realize the temporal overlap between the two beams. This temporal overlap was realized prior to the sphere experiment by replacing the sphere by a nonlinear crystal of RTP in which a SFG was realized in a way to generate a visible beam. Since pulses of 15 ps have a spatial extension of about 4.5 mm, the precision of the delay line must be in the order of the millimeter. The spherical crystal to characterize was then placed at the center of an Euler circle allowing the rotation of the sphere on itself. The mechanism of the Euler circle is described later in section 2.5. The alignment of the two beams was realized thanks to an He-Ne laser that was premilinary adjusted to propagate exactly along a diameter of the sphere. The generated beam was detected by means of different photodiodes according to the wavelength: the visible and near-IR range until 1 μm was covered by Silicon, the range $1 - 3\,\mu$m by InGaAs, the range $3 - 5.5\,\mu$m by Nitrogen-cooled InSb, and the far infrared until 12 μm by Nitrogen-cooled HgCdTe.

The sphere experiment requires a quasi-parallel propagation inside the sphere in order to get a good precision on the measured direction of propagation. A non parallel beam would also lead to an overevaluation of the spectral and angular acceptances. A "quasi-parallel" propagation is usually realized thanks to an *entrance lens* that focuses the beam at the front focal point of the sphere. It requires preliminary calculations described hereafter.

2.4 Propagation of Gaussian beams in a sphere

2.4.1 The spherical lens

A crystal cut as a sphere behaves like a spherical lens. The focal length f of a sphere with a radius r and a refractive index n is given by [6]:

$$f = \frac{nr}{2(n-1)} \tag{2.1}$$

For an incident parallel beam and if $n < 2$, then $f > r$ and the focal point of the sphere is outside the sphere. At the opposite, $n > 2$ leads to $f < r$, so that the focal point is inside the sphere, which may be detrimental to the crystal according to its optical damage. These

situations are represented in Fig. 2.3.

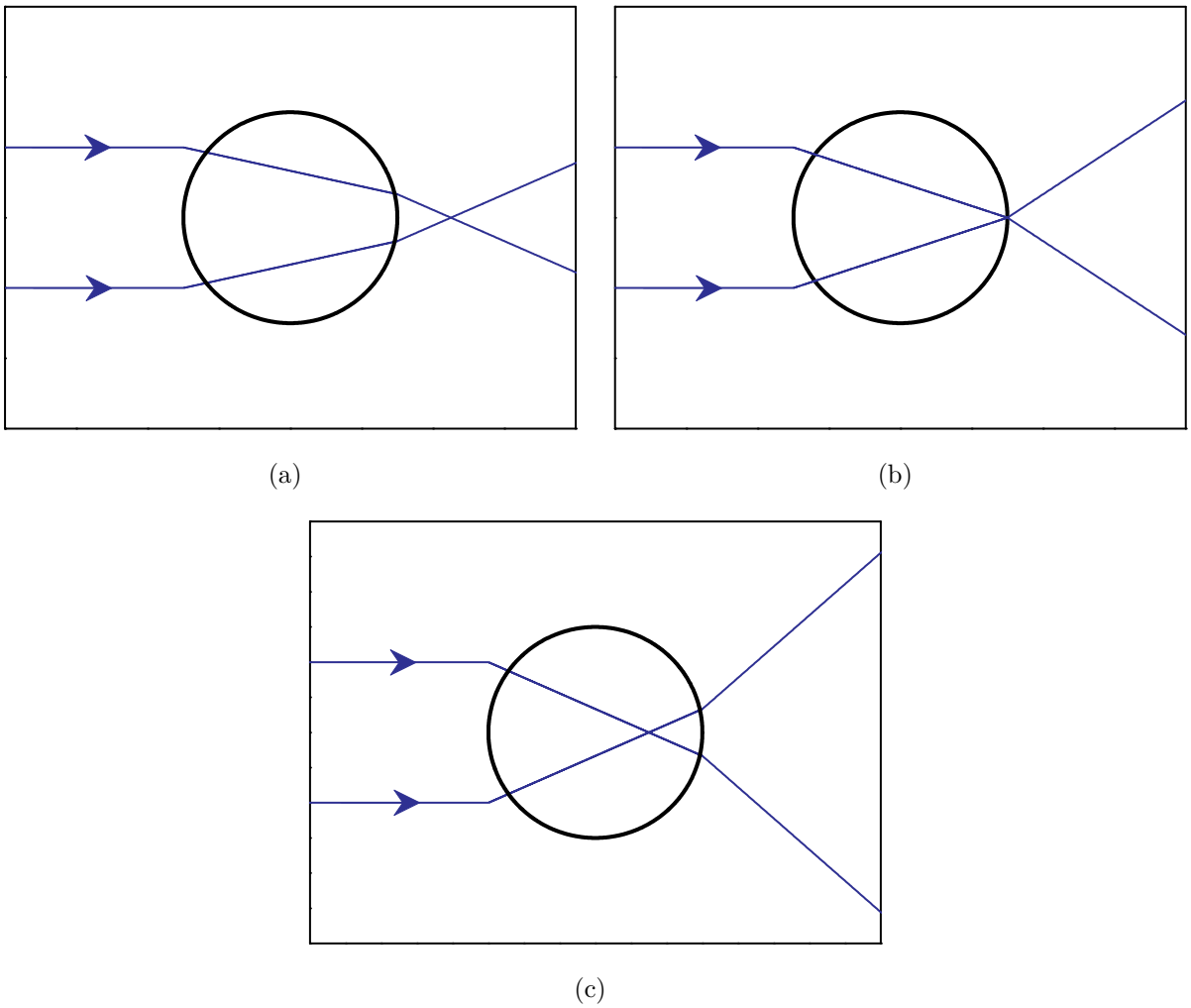

Figure 2.3: Focalization of a parallel beam by spheres with different refractive indices: (a) $n = 1.5$, (b) $n = 2.0$, (c) $n = 3.0$.

In any case, it will be important to use a focusing lens in order to control the radius and location of the beam waist inside the sphere. Note that $CdSiP_2$ and 5%MgO:PPLN have refractive indices $n > 2$.

2.4.2 Focusing conditions and Gaussian beam profile inside the crystal sphere

The proper focusing conditions can be determined by using the Gaussian formalism in the paraxial approximation [19]. The *complex beam parameter* $q(z)$ is a complex number which

characterizes the Gaussian beam at any point z along the axis of the beam. It is calculated from both the radius of curvature of the phase front $R(z)$ and the beam radius $w(z)$. Its expression is written:

$$\frac{1}{q(z)} = \frac{1}{R(z)} - i\frac{\lambda}{\pi w^2(z)} \tag{2.2}$$

The evolution of $q(z)$ when the beam propagates through several optical systems can be calculated using the *transfer matrices method*, where each optical system is described by an $ABCD$ matrix [20]. Eq. 2.3 allows the resulting beam parameter q_f to be calculated for a given initial beam parameter q_i [20]:

$$q_f = \frac{Aq_i + B}{Cq_i + D} \tag{2.3}$$

Eq. 2.3 allows us to calculate the longitudinal spatial profile of a Gaussian beam through the considered optical system. The matrices are the same as the ones used for geometric ray tracing [20]. A propagation inside a medium of refractive index n over a distance z is then described by [20]:

$$\begin{pmatrix} A & B \\ C & D \end{pmatrix} = \begin{pmatrix} 1 & z/n \\ 0 & 1 \end{pmatrix} \tag{2.4}$$

The pass through a spherical dioptre with a radius of curvature R separating two media of refractive indices n_1 and n_2 is described by [20]:

$$\begin{pmatrix} A & B \\ C & D \end{pmatrix} = \begin{pmatrix} 1 & 0 \\ \dfrac{n_2 - n_1}{R} & 1 \end{pmatrix} \tag{2.5}$$

where $R < 0$ at the entrance of the dioptre, and $R > 0$ at the exit. We used these matrices and MATLAB for the modelisation of the propagation. It enables to calculate the distance d_{opt} between the entrance lens and the sphere, leading to a quasi-parallel propagation inside the sphere with an associated maximal beam radius for which the optical damage is not overpassed. This optimal configuration is illustrated on Fig. 2.4.
From the numerical data of table 2.1, we calculated the evolution of the minimum beam radius w_{min} inside the sphere as a function of the distance d between a ZnSe focusing lens and the sphere entrance for $CdSiP_2$ and 5%MgO:PPLN.

The corresponding curves at $\lambda = 1.064\,\mu$m are given in Figs. 2.5 and 2.6. These figures

	Lens	Crystal spheres	
Materials	ZnSe	5%MgO:PPLN	$CdSiP_2$
Entrance radius of curvature (mm)	-139.96	-1.95	-2.495
Exit radius of curvature (mm)	∞	$+1.95$	$+2.495$
Thickness (mm)	2.6	3.9	4.99
Refractive index at $1.064\,\mu$m	$n = 2.48$	$n_o = 2.22$ $n_e = 2.15$	$n_o = 3.16$ $n_e = 3.11$
Reference of Sellmeier equations	[21]	[22]	[23]

Table 2.1: Data used for the modelisation of the Gaussian beam through the optical system made of a ZnSe entrance plano-convex lens and the studied crystal sphere of 5%MgO:PPLN or $CdSiP_2$.

allow us to determine the optimal distance d_{opt} corresponding to the maximum value of w_{min}. The optimal distance d_{opt} is 94.7 mm for $CdSiP_2$ and 95.2 mm for 5%MgO:PPLN at $1.064\,\mu$m. Note that since $CdSiP_2$ has a higher refractive index than 5%MgO:PPLN, the placement of the entrance lens is more tricky as shown in Figs. 2.5(a) and 2.6(a). For example, if one needs to have $w_{\text{min}} > 0.05$ mm inside the sphere in order to avoid optical damage, the optimal distance must belong to an interval of $\Delta d = 0.8$ mm for $CdSiP_2$, versus 8.9 mm for 5%MgO:PPLN. The situation was not so tough in media of refractive index $n < 2$ because there were no risk to focus the beam inside the sphere if the entrance lens was too far from the sphere (cf Fig. 2.3(a)).

Figs. 2.5(b) and 2.6(b) give the position z_{min} of w_{min} inside the sphere, the origin being taken at the entrance of the sphere. We can distinguish different situations according to the value of d, which are illustrated in the case of $CdSiP_2$ in Fig. 2.7. First, if $d < 93.5$ mm, the beam focuses inside the sphere; point A corresponds to this case, with a beam waist being located in the first half of the sphere. Then, if $93.5\,\text{mm} < d < 98\,\text{mm}$, there is no focalization inside the sphere, and the minimum beam radius is located either at the entrance or at the exit of the sphere (point B). Finally, if $d > 98$ mm, the beam focuses again inside the sphere, always in the second half (point C).

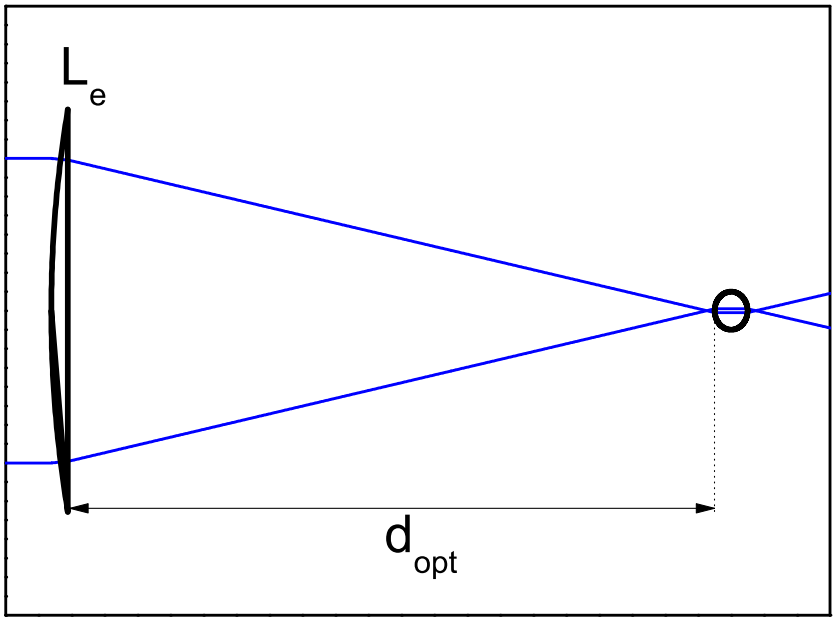

(a)

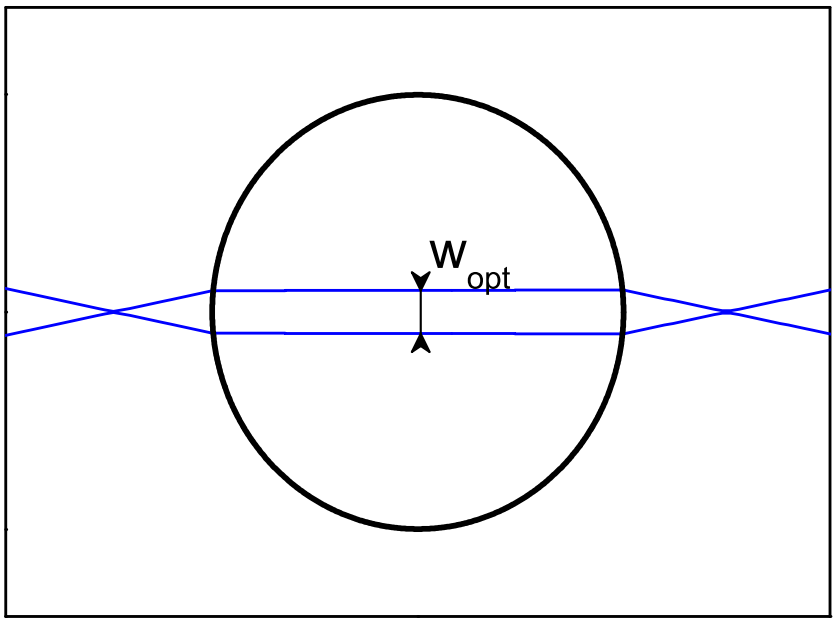

(b)

Figure 2.4: Gaussian calculation of the optimal focusing configuration leading to a quasi-parallel propagation inside the crystal sphere. L_e is the entrance lens, $d = d_{\text{opt}}$ is the optimal distance between the lens and the sphere entrance. (a) Scheme of the experiment. (b) Magnification zoom.

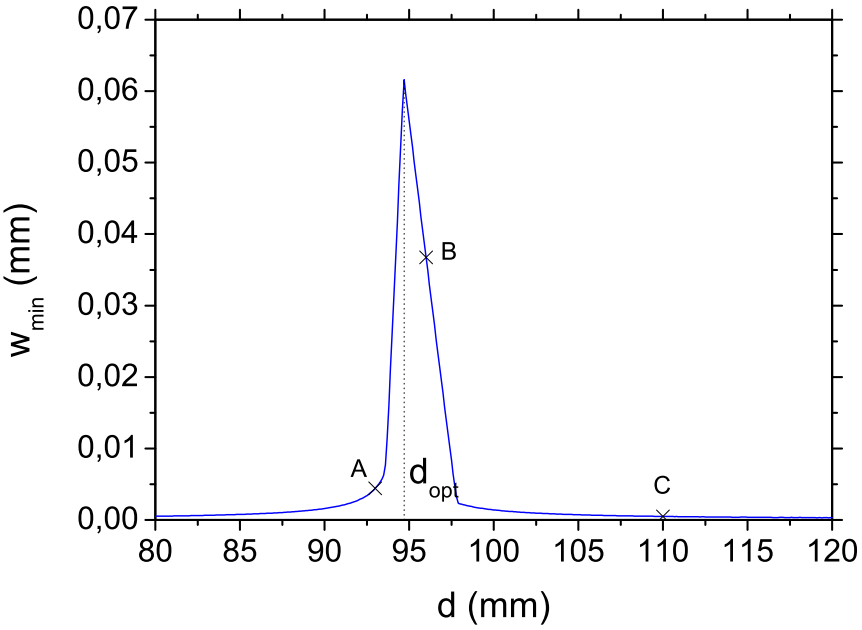

(a)

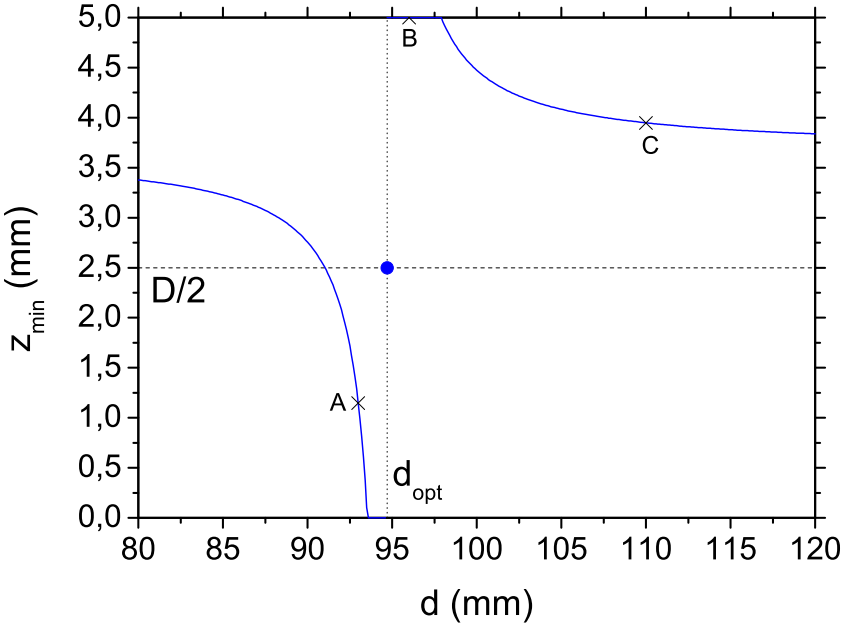

(b)

Figure 2.5: Minimum beam radius $w_{\min}$ (a) and its location $z_{\min}$ (b) inside the $CdSiP_2$ sphere at the wavelength 1.064 μm as a function of the distance d between the incident ZnSe lens and the sphere entrance. The origin for $z_{\min}$ is chosen at the entrance of the sphere. D is the diameter of the sphere and the horizontal dashed line corresponds to the center of the sphere. d_{opt} is the optimal distance.

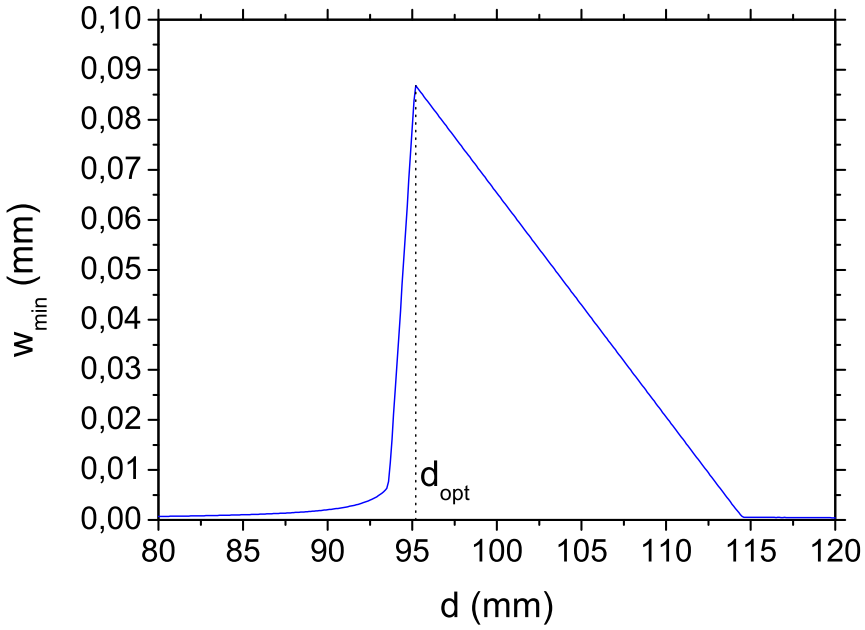

(a)

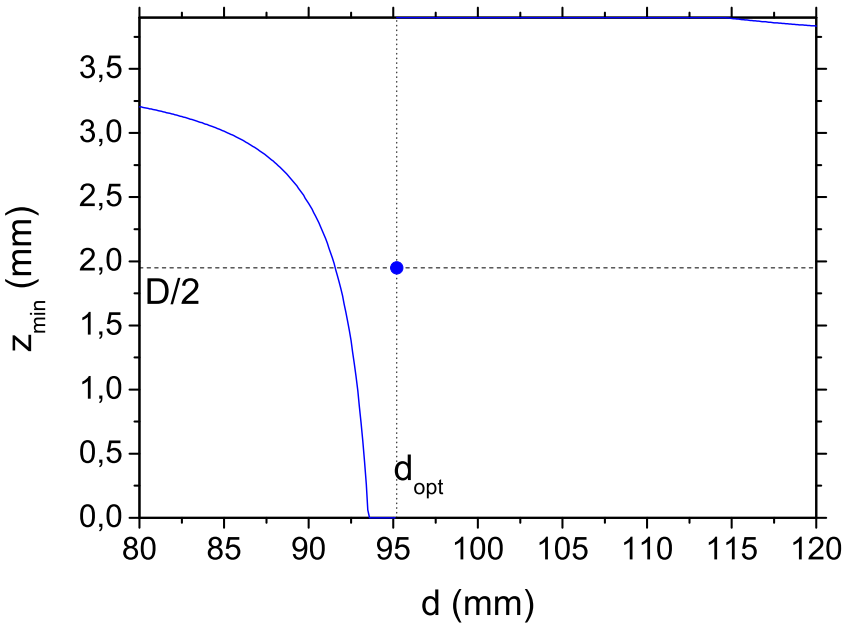

(b)

Figure 2.6: Minimum beam radius $w_{\min}$ (a) and its location $z_{\min}$ (b) inside the 5%MgO:PPLN sphere at the wavelength 1.064 μm as a function of the distance d between the incident ZnSe lens and the sphere entrance. The origin for $z_{\min}$ is chosen at the entrance of the sphere. D is the diameter of the sphere and the horizontal dashed line corresponds to the center of the sphere. d_{opt} is the optimal distance.

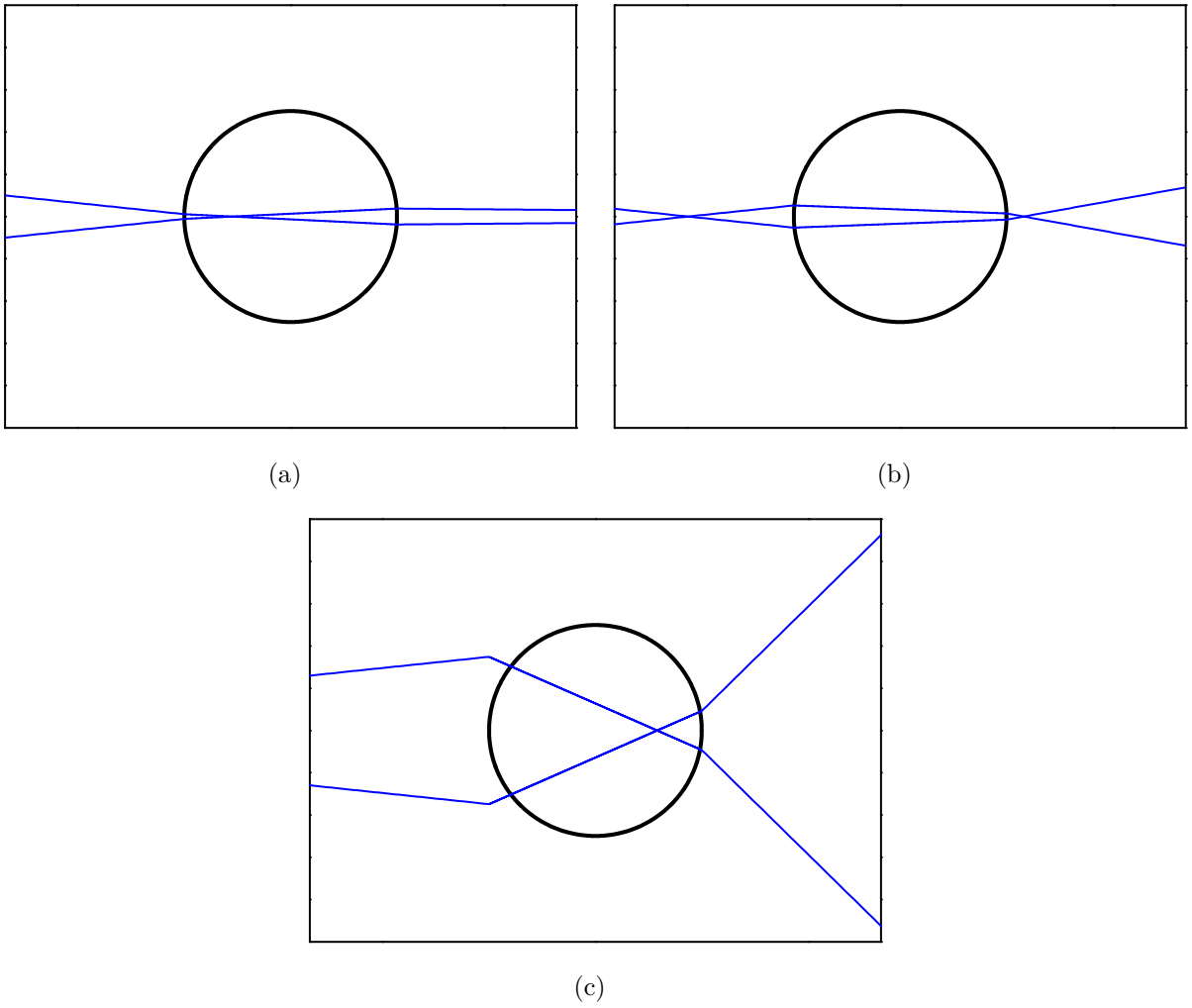

(a) (b)

(c)

Figure 2.7: Geometry of the beam at $\lambda = 1.064\,\mu$m inside the sphere of $CdSiP_2$ at different distances d between the entrance lens and the entrance sphere corresponding to point A (a), point B (b), and point C (c) of Fig. 2.5.

The sphere experiments have to be carried out on the whole transparency range of the studied crystals, *i.e.* for wavelengths varying from 0.5 μm to 5 μm in the case of 5%MgO:PPLN, and from 0.5 μm to 10 μm in the case of $CdSiP_2$. Due to the dispersion of the focal lengths of both the entrance lens and the sphere, the optimal distance d_{opt} strongly depends of the wavelength, as shown in Figs. 2.8(a) and 2.8(b) for $CdSiP_2$ and 5%MgO:PPLN respectively. The optimal distance d_{opt} varies a lot between 1 μm and 2 μm where the refractive indices dispersion is the strongest.

Using the optimal focusing configuration described above, it is possible to tune w_{min} by varying the beam radius w_{inc} of the input beam thanks to a telescope. Figs. 2.9(a) and 2.9(b) show the evolution of w_{min} as a function of w_{inc} in the case of $CdSiP_2$ and 5%MgO:PPLN respectively at 3 μm. Note that another way to increase the beam radius inside the sphere would be to reduce the focal length of the entrance lens f, but it was not realizable in our case because of mechanical obstruction problems with the Euler circle.
The optimal focusing configuration being defined, it is necessary to know the optical damage threshold expressed in $[\text{J/cm}^2]$ or $[\text{W/cm}^2]$, of the studied crystal in order to calculate the energy of the incident beam(s) that should not be overpassed in order to avoid any damage inside the sphere. As example, we considered an incident beam at 1.064 μm and a pulse duration of 15 ps and a repetition rate of 10 Hz as in our experiments. The measurement of the optical damage threshold of $CdSiP_2$ was done in this work and is presented later in chapter 4: it is of about 0.3 J/cm^2. The optical damage threshold of 5%MgO:PPLN at a pulse duration of 7 ns is about 3 J/cm^2 [24]: according to the square root dependance of the energy density on the pulse duration [25], the damage threshold at 15 ps is in the order of 65 J/cm^2. Given that the surface of the beam inside the sphere is $S = \pi w_0^2$ and given the curves of Fig. 2.9, it is possible to calculate the threshold energy of the incident beam $E_{\text{inc}}^{\text{th}}$ that must not be overpassed. The result of these calculations are shown in Fig. 2.10 in both cases of $CdSiP_2$ and 5%MgO:PPLN. These curves are of prime importance for the conception of sphere experiments.

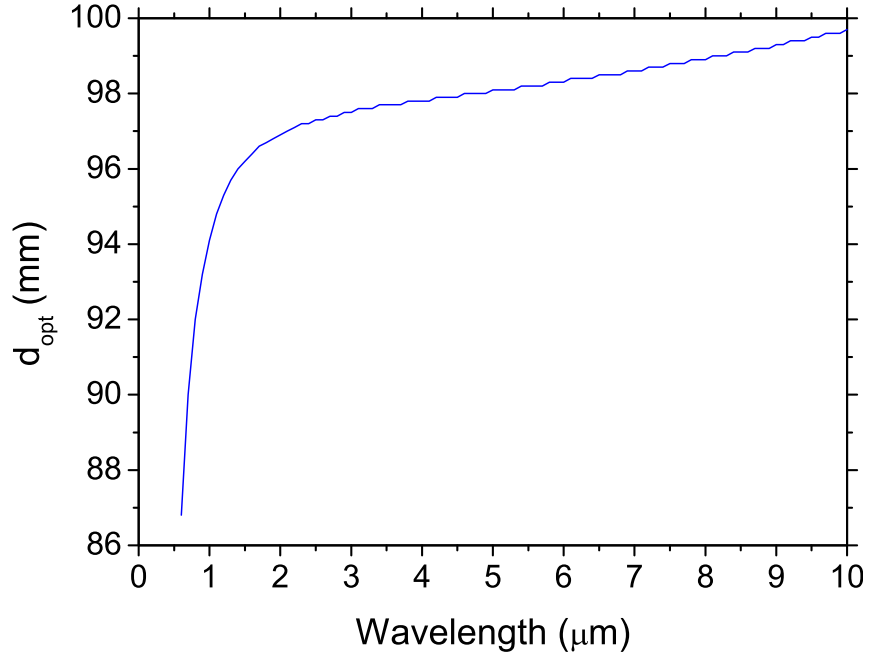

(a)

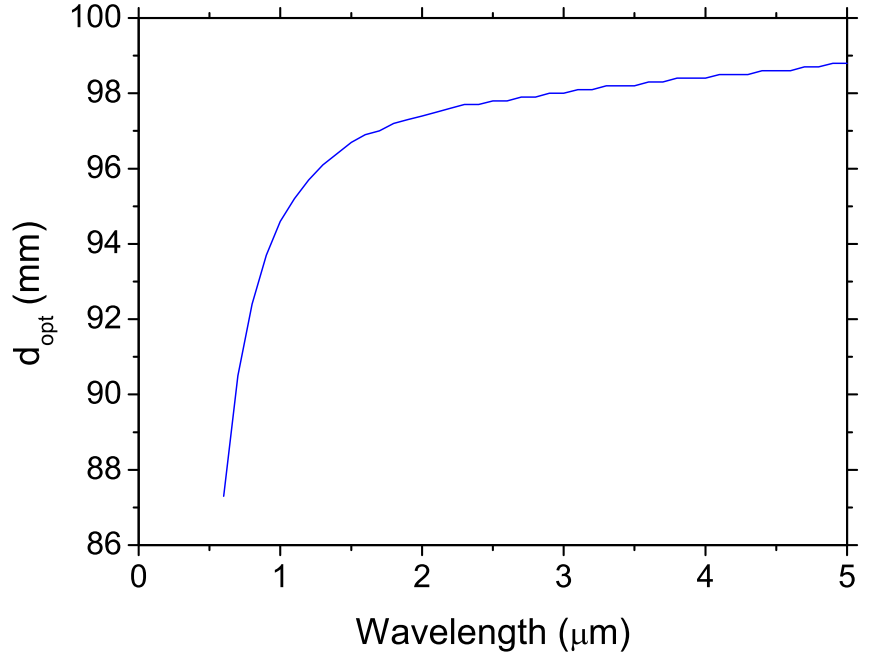

(b)

Figure 2.8: Optimal distance d_{opt} between the lens and the spheres entrance as a function of the wavelength. (a) Sphere of $CdSiP_2$ of diameter 4.99 mm; (b) sphere of 5%MgO:PPLN of diameter 3.9 mm.

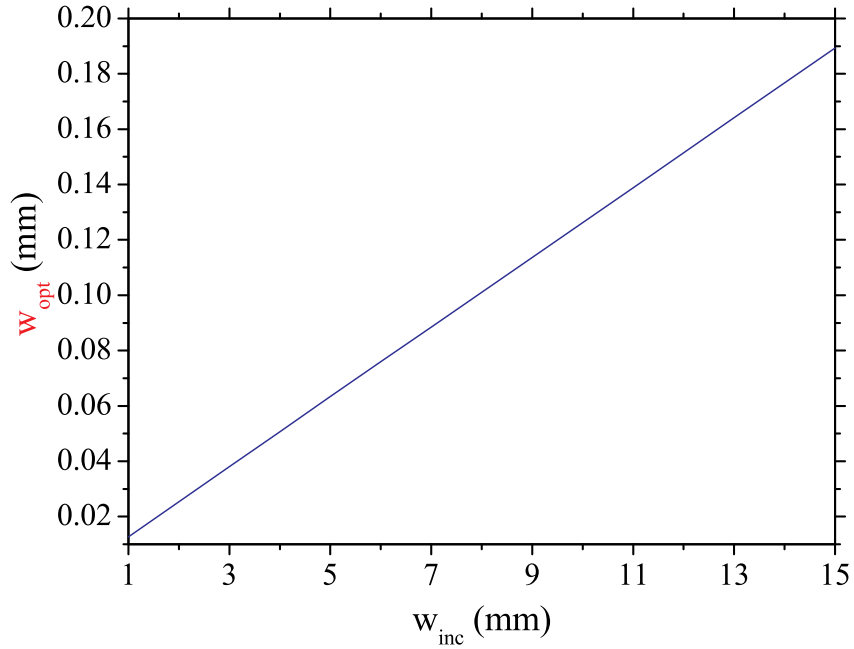

(a)

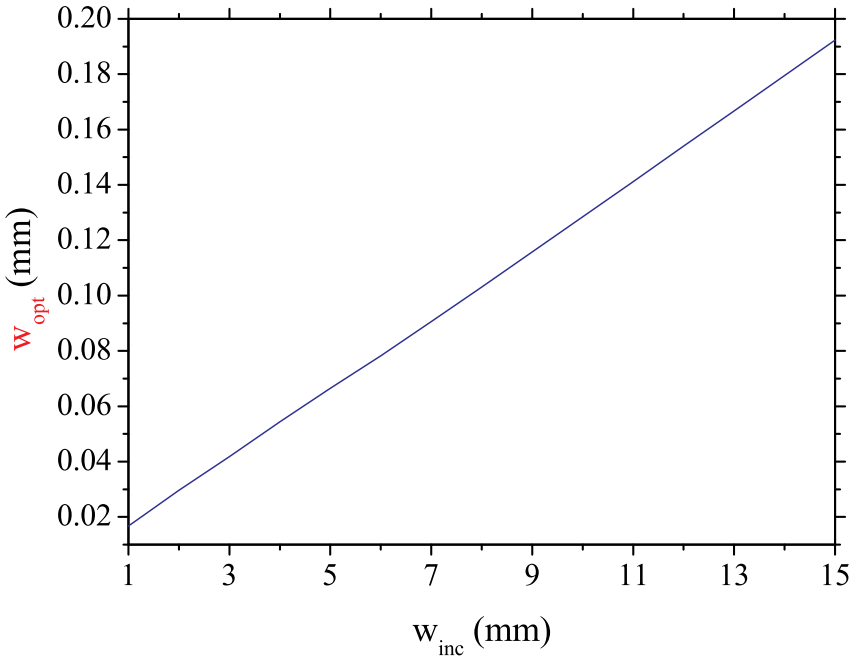

(b)

Figure 2.9: Evolution of the minimum beam radius w_{min} inside the sphere as a function of the incident beam waist radius w_{inc}. (a) Sphere of $CdSiP_2$ of diameter 4.99 mm; (b) sphere of 5%MgO:PPLN of diameter 3.9 mm.

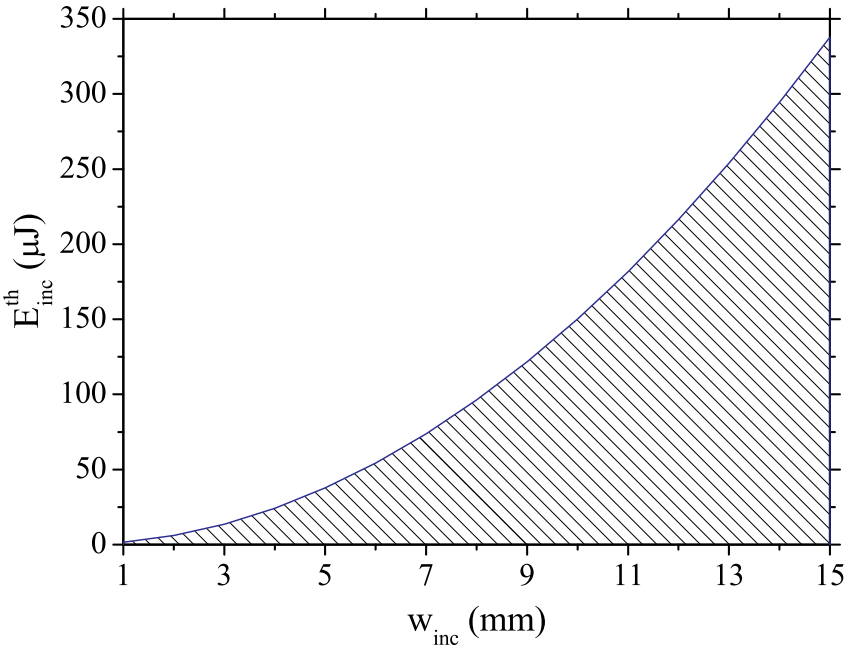

(a)

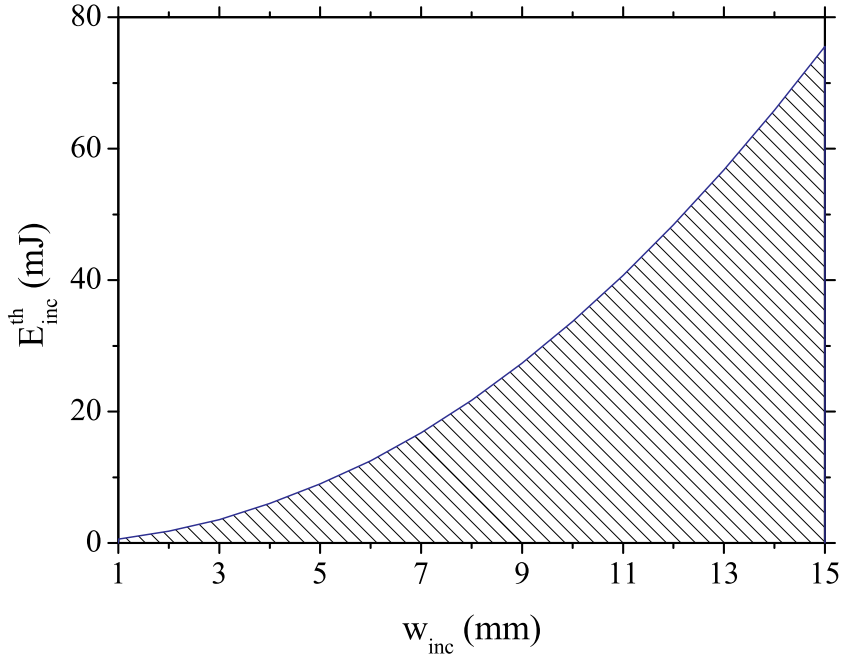

(b)

Figure 2.10: Maximum allowed energy $E_{\text{inc}}^{\text{th}}$ of the incident beam at 1.064 μm in order to avoid optical damage as a function of the incident beam radius w_{inc}. The hatched zones correspond to the permitted configurations. The corresponding values of the beam waist radius w_0 inside the spheres are given in Figs. 2.9. (a) Sphere of $CdSiP_2$ of diameter 4.99 mm; (b) sphere of 5%MgO:PPLN of diameter 3.9 mm.

It is also important to be sure that the propagation inside the sphere is parallel if one wants to measure phase-matching directions and angular acceptances with a good accuracy. In order to know if the propagation is quasi-parallel inside the sphere when $d = d_{\text{opt}}$, it is necessary to compare the radius of the sphere R with the Rayleigh length z_R given by [19]:

$$z_R = \frac{\pi\, n\, w_0^2}{\lambda} \tag{2.6}$$

In our experimental conditions, we have $w_{\text{inc}} \approx 5\,\text{mm}$, that gives $w_0 \approx 0.06\,\text{mm}$ for $CdSiP_2$ as well as for 5%MgO:PPLN from the curves of Fig. 2.9. From the radii and the refractive indices given in table 2.1, we can compute the Rayleigh length as a function of the wavelength for each crystal sphere, as shown in Fig. 2.11. We see that in both cases, the condition $z_R > R$ is verified over the whole transparency range of the crystal.
As a conclusion, since quasi-parallel propagation is ensured over the whole transparency ranges of the spheres, the measurements of phase-matching directions and acceptances performed on 5%MgO:PPLN and $CdSiP_2$ using the sphere method with our experimental conditions will be given with good accuracy, and in a safety way.

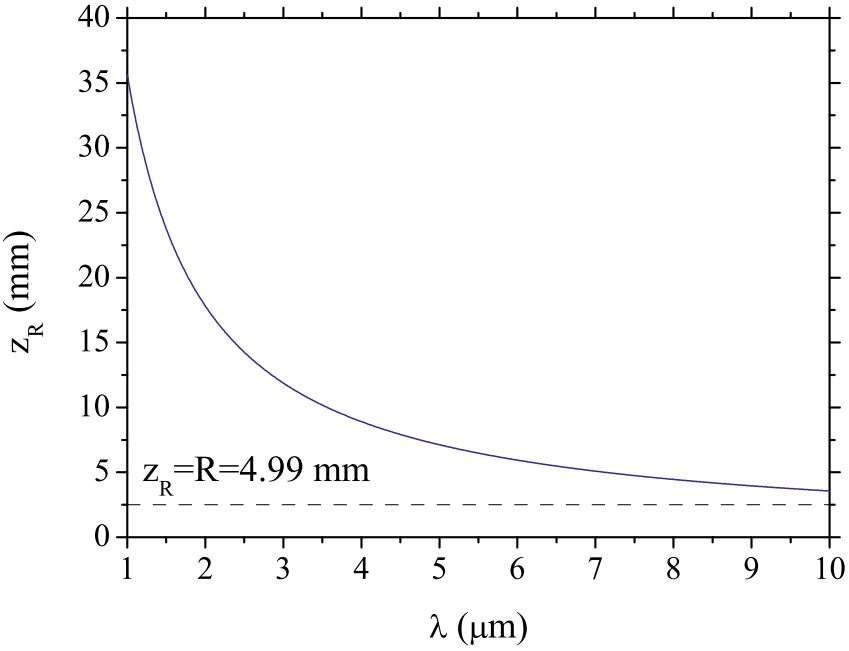

(a)

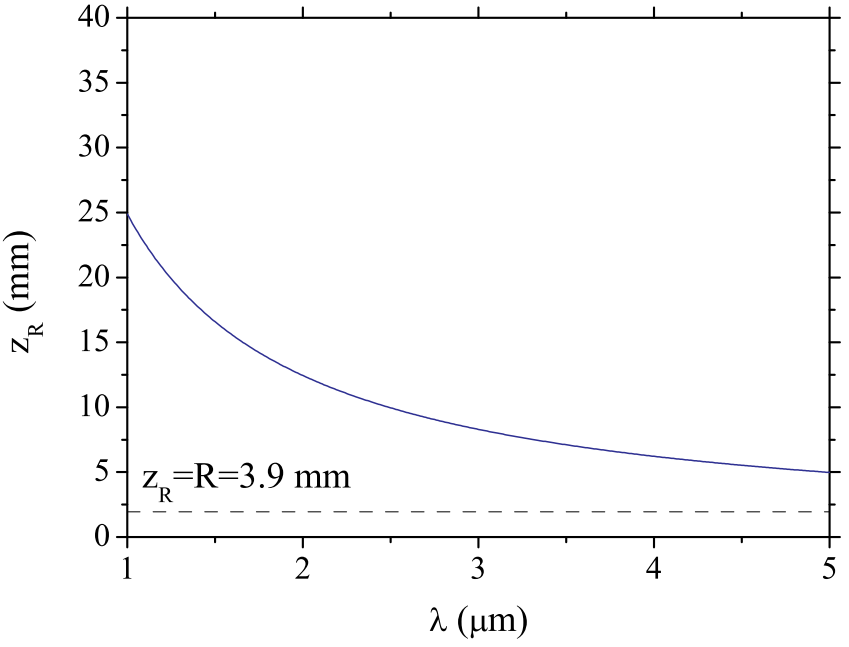

(b)

Figure 2.11: Rayleigh lengths z_R of the focused beam inside the $CdSiP_2$ (a) and 5%MgO:PPLN (b) sphere calculated as a function of the wavelength λ. R is the sphere radius.

2.5 Goniometry of the Euler circle

We have seen in chapter 1 that the phase-matching angles $(\theta_{\mathrm{PM}}, \phi_{\mathrm{PM}})$ are defined in the dielectric frame (x, y, z) of the studied nonlinear crystal. In order to propagate the laser beams in the crystal sphere at any angle, an *Euler circle* was used. The goal of this section is then to explain the way to pass from the angles (α, β, γ) of the Euler circle to the angles (θ, ϕ) of the dielectric frame.

The Euler circle is composed of three rotating stages as shown in Fig. 2.12.

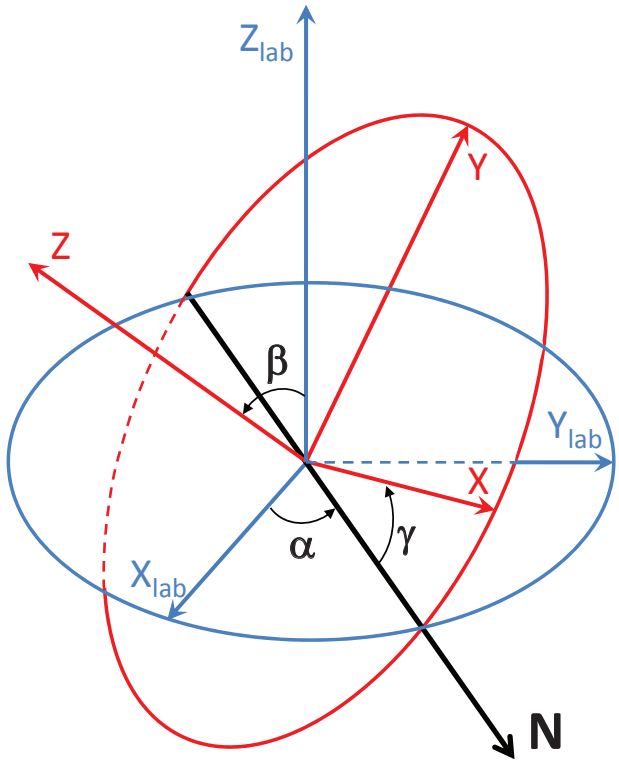

Figure 2.12: Orientation of the Euler angles (α, β, γ). $(X_{\mathrm{lab}}, Y_{\mathrm{lab}}, Z_{\mathrm{lab}})$ is the laboratory frame. (X, Y, Z) is the frame associated to the goniometric head on which the crystal sphere is stuck. The label N stands for the line of nodes.

The Euler angles express the link between the fixed laboratory frame $(X_{\mathrm{lab}}, Y_{\mathrm{lab}}, Z_{\mathrm{lab}})$ and the rotated frame (X, Y, Z) associated to the goniometric head supporting the crystal. The definition of the angles require to define the *line of nodes* that is the intersection of the XY and the $X_{\mathrm{lab}}Y_{\mathrm{lab}}$ planes. The Euler angles are defined as follows [26]:

- α is the angle between the X-axis and the line of nodes;

- β is the angle between the Z_{lab}-axis and the Z-axis;
- γ is the angle between the line of nodes and the X-axis.

The angular conversion between a direction in the (x, y, z) frame into the (X, Y, Z) frame can be carried out by means of the transformation matrix M expressed as the product of three rotation matrices [26]:

$$M = \begin{pmatrix} \cos\gamma & \sin\gamma & 0 \\ -\sin\gamma & \cos\gamma & 0 \\ 0 & 0 & 1 \end{pmatrix} \begin{pmatrix} 1 & 0 & 0 \\ 0 & \cos\beta & \sin\beta \\ 0 & -\sin\beta & \cos\beta \end{pmatrix} \begin{pmatrix} \cos\alpha & \sin\alpha & 0 \\ -\sin\alpha & \cos\alpha & 0 \\ 0 & 0 & 1 \end{pmatrix} \tag{2.7}$$

As the laser beam keeps a fixed direction in the laboratory frame, its direction can be chosen arbitrarily: we choose the X_{lab}-axis in the present work. The direction of the beam in the laboratory frame is thus given by:

$$\vec{u}|_{\text{lab}} = \begin{pmatrix} 1 \\ 0 \\ 0 \end{pmatrix} \tag{2.8}$$

In the frame (X, Y, Z) of the goniometric head, this direction is given by:

$$\vec{u}|_{\text{gonio}} = A\,\vec{u}|_{\text{lab}} = \begin{pmatrix} \cos\alpha\cos\gamma - \sin\alpha\cos\beta\sin\gamma \\ -\cos\alpha\sin\gamma - \sin\alpha\cos\beta\cos\gamma \\ \sin\alpha\sin\beta \end{pmatrix} \tag{2.9}$$

This direction can also be expressed in spherical coordinates (θ_g, ϕ_g) in the (X, Y, Z) frame as follows:

$$\vec{u}|_{\text{gonio}} = \begin{pmatrix} \sin\theta_g\cos\phi_g \\ \sin\theta_g\sin\phi_g \\ \cos\theta_g \end{pmatrix} \tag{2.10}$$

The two ways of defining $\vec{u}|_{\text{gonio}}$ give the correspondance between the Euler angles and the corresponding angles of spherical coordinates in the (X, Y, Z) frame, *i.e.*:

$$\begin{cases} \cos\alpha\cos\gamma - \sin\alpha\cos\beta\sin\gamma = \sin\theta_g\cos\phi_g \\ -\cos\alpha\sin\gamma - \sin\alpha\cos\beta\cos\gamma = \sin\theta_g\sin\phi_g \\ \sin\alpha\sin\beta = \cos\theta_g \end{cases} \tag{2.11}$$

The systematic experimental procedure to find the phase-matching angles is to vary the θ angle of the dielectric frame by keeping a fixed ϕ angle [13]. The β angle was thus fixed to $-\pi/2$. Nevertheless, due to dead zones caused by the mechanical support of the Euler

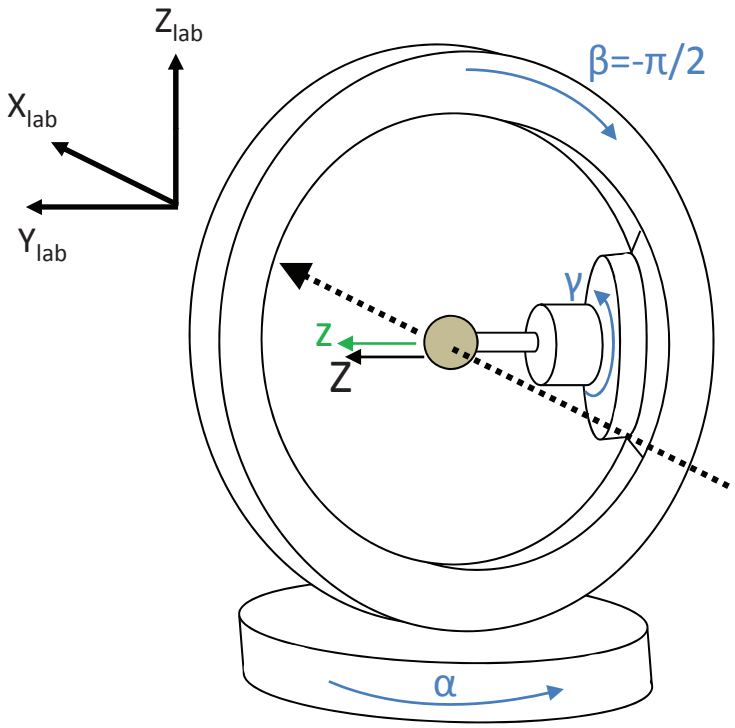

Figure 2.13: Scheme of the Euler circle where the z-axis of the dielectric frame is along the Z-axis of the goniometric head. The direction of propagation of the laser beam is along the X_{lab}-axis of the laboratory frame.

circle, it was necessary to successively stick the sphere in two different directions on the gonometric head: ($z = Z$, $x = X$, $y = Y$) and ($y = Z$, $z = -Y$, $x = X$). In the first case, illustrated on Fig. 2.13, the dielectric frame (x, y, z) coincides with the goniometric frame, *i.e.*:

$$\begin{pmatrix} \sin\theta_g \cos\phi_g \\ \sin\theta_g \sin\phi_g \\ \cos\theta_g \end{pmatrix} = \begin{pmatrix} \sin\theta\cos\phi \\ \sin\theta\sin\phi \\ \cos\theta \end{pmatrix} \tag{2.12}$$

According to Eq. 2.11 and Eq. 2.12, we thus have:

$$\begin{cases} \cos\alpha\cos\gamma = \sin\theta\cos\phi \\ -\cos\alpha\sin\gamma = \sin\theta\sin\phi \\ -\sin\alpha = \cos\theta \end{cases} \tag{2.13}$$

Then it comes:

$$\begin{cases} \theta = \arccos(-\sin\alpha) = \dfrac{\pi}{2} - \alpha \\ \\ \phi = \arccos\left(\dfrac{\cos\alpha\cos\gamma}{\sin\theta}\right) = \arccos(\cos\gamma) = \gamma \end{cases} \tag{2.14}$$

The second case is illustrated in Fig. 2.14.

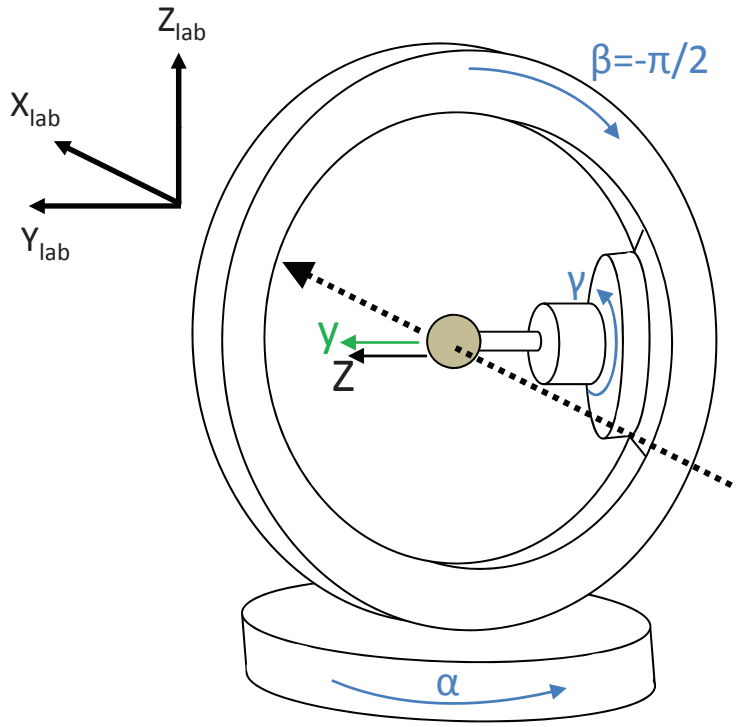

Figure 2.14: Scheme of the Euler circle where the y-axis of the dielectric frame is along the Z-axis of the goniometric head. The direction of propagation of the laser beam is along the X_{lab}-axis of the laboratory frame.

The associated matrices are:

$$\begin{pmatrix} \sin\theta_g \cos\phi_g \\ \sin\theta_g \sin\phi_g \\ \cos\theta_g \end{pmatrix} = \begin{pmatrix} \sin\theta\cos\phi \\ \cos\theta \\ -\sin\theta\sin\phi \end{pmatrix} \tag{2.15}$$

According to Eq. 2.11 and Eq. 2.15, it comes:

$$\begin{cases} \cos\alpha\cos\gamma = \sin\theta\cos\phi \\ -\cos\alpha\sin\gamma = \cos\theta \\ -\sin\alpha = -\sin\theta\sin\phi \end{cases} \tag{2.16}$$

Finally, we get:

$$\begin{cases} \theta = \arccos(-\cos\alpha\sin\gamma) \\ \\ \phi = \arccos\left(\dfrac{\cos\alpha\cos\gamma}{\sin\theta}\right) \end{cases} \tag{2.17}$$

Then once a particular direction is detected using the Euler circle, formula 2.14 and 2.17 allow this direction to be expressed in the dielectric frame of the crystal.

2.6 Conclusion

The theoritical basis given in this chapter were useful for designing the angular experiments presented in the next chapters. Indeed, measurements of phase-matching directions necessitated the use of the Euler circle. Moreover, the conditions of quasi-parallel propagation inside the crystal sphere were permanently applied to the experimental setup, in both cases of 5%MgO:PPLN and $CdSiP_2$.

Chapter 3

Angular quasi-phase-matching in 5%MgO:PPLN

3.1 State of the art

Quasi-Phase-Matching (QPM) in periodically-poled materials is today the most promising configuration for achieving efficient three-wave nonlinear parametric interactions [8, 27, 28, 29]. Indeed, it makes possible to use the stronger element χ_{zzz} of the second-order electric susceptibility tensor. Commercial devices are now available, in particular based on periodically-poled $LiNbO_3$ (PPLN) and periodically-poled $KTiOPO_4$ (PPKTP). The poling period has to be equal to the coherence length $L_c = \pi/\Delta k$ of the considered interaction, as previously explained in paragraph 1.6 of chapter 1. The calculation of L_c requires a precise knowledge of the refractive indices of the material at the three involved wavelengths. For tunable-wavelength devices, a variation of the grating periodicity is then necessary to compensate the variation of Δk due to the dispersion of the refractive indices. The three methods which are generally used to realize this variation are shown in Figs. 3.1(a), 3.1(b) and 3.1(c). In the two first cases corresponding to Figs. 3.1(a) and 3.1(b), the direction of the beam is fixed and chosen along a principal axis of the crystal in order to avoid walk-off. The drawback of the fan-shaped grating is that the the period varies inside the beam diameter, increasing the spectral bandwidth, and the disadvantage of the multi-grating scheme is that it does not allow a continuous variation of the wavelength but only a discrete one due to the jump between a grating and another one. These disadvantages have been circumvented by using the third scheme given in Fig. 3.1(c) where the periodically-poled crystal is cut as a cylinder with the revolution axis parallel to the ferroelectric axis

[30]. Such a geometry allowed any grating period to be addressed by rotating the cylinder around its revolution axis, the propagation of the beams keeping a normal incidence for any direction. Recent advances led to a successful poling over few millimeters of 5%MgO:PPLN

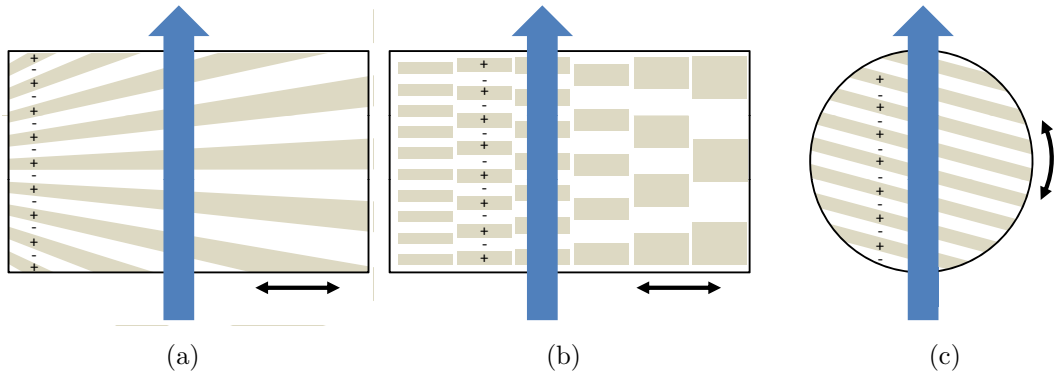

Figure 3.1: The three schemes for tunable devices using QPM. (a) Fan-shaped gratings, (b) multi-gratings, (c) single grating in a cylinder sample. The large arrow represents the fixed laser beam. The spectral tunability of the generated wave is obtained by translating the crystal in the cases (a) and (b), or rotating the crystal (c).

slabs, allowing the use of pump laser beams with large aperture, and so with high energy [31]. These advances enable to increase the output energy of the devices based on QPM, but they also give us the possibility to test the angular quasi-phase-matching (AQPM) concept developed in our group and described in section 1.6 of chapter 1. Indeed a thick sample enables to have a reasonable interaction length at any angle with respect to the grating vector [2].

This chapter presents the first experiments of AQPM using a sphere of 5%MgO:PPLN [32]. The measurements of AQPM directions in the case of type I SHG and types I and II DFG are presented and are used to refine the Sellmeier coefficients of 5%MgO:PPLN. The benefit of AQPM over the classical techniques is then discussed, especially in term of spectral acceptance. Finally, the potentialities of AQPM versus the grating period are summarized.

3.2 Experimental setup

In order to be able to measure any SHG or DFG AQPM direction, we cut a 5%MgO:PPLN sphere with a diameter of 3.9 mm from a slab (cf. Fig. 3.2) having a grating period

$\Lambda = 32.2\,\mu$m provided by the group of Takunori Taira of the Institute for Molecular Science (IMS) in Japan. The sphere was polished, oriented and stuck on a goniometric head along the z-axis or y-axis of the dielectric frame with a precision better than 0.5° by using the Laue method.

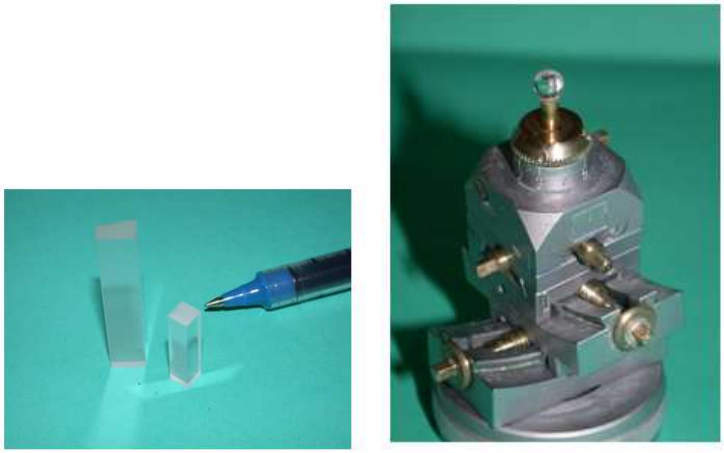

(a) (b)

Figure 3.2: Crystal of 5%MgO:PPLN used for the experiment; (a) slab of thickness 5 mm fabricated at IMS; (b) sphere of diameter 3.9 mm cut at Néel Institute.

The experimental setup was presented in Fig. 2.2 of chapter 2. The sphere being placed at the center of an Euler circle and by using the focusing configuration described in section 2.4, it was possible to propagate the laser beams in any direction of propagation of the crystal by keeping normal incidence. The correpondance between the Euler angles (α, β, γ) and the angles of spherical coordinates (θ, ϕ) giving the direction of propagation in the dielectric frame was calculated thanks to formula 2.12 and 2.15. The focusing lens located at the entrance side of the sphere ensures a quasi-parallel propagation of the beams inside the sphere as described in section 2.4.2. The beam emitted by the parametric source, tunable between $0.4\,\mu$m and $10\,\mu$m, was used as the fundamental wave for SHG measurements, or as the injection beam by mixing it with a beam at $1.064\,\mu$m for the study of DFG. Two half-wave plates allowed the incident beams to be polarized according to the chosen AQPM type defined in table 1.2 of chapter 1. The wavelength was continuously controlled by a Chromex 250 SM monochromator. SHG or DFG directions were detected when the associated conversion efficiency was maximal, leading to a measurement of the AQPM angles with an accuracy of about ±1°.

3.3 AQPM directions

The experiments presented below concern SHG and DFG. Although AQPM allows the eight possible combinations of polarization given in table 1.2, all of these are not necessary compatible with the momentum conservation relation 1.27 according to the grating period and the refractive indices at the considered wavelengths. In particular, with our grating period of 32.2 μm, type IV corresponding to three extraordinary polarized waves is not possible; it would have required a smaller grating period.

3.3.1 Type I and II second-harmonic generation

In the following, we use the notation SHG $(\lambda_\omega, \lambda_\omega, \lambda_{2\omega})$ for SHG $(\lambda_\omega^{-1} + \lambda_\omega^{-1} = \lambda_{2\omega}^{-1})$. By using the incident beam coming from the OPG-OPA stage, we were able to measure the AQPM tuning curves at $T = 22°C$ of type I SHG $(\lambda_\omega^o, \lambda_\omega^o, \lambda_{2\omega}^e)$ and type II $\equiv$ III SHG $(\lambda_\omega^o, \lambda_\omega^e, \lambda_{2\omega}^e)$ in the full space and in the full transparency range of 5%MgO:PPLN: indices (o) and (e) stand for the ordinary and extraordinary polarizations, respectively [32]. The data of type I SHG are given in Fig. 3.3 in the xz and yz planes, while Fig. 3.4 shows type II SHG in the xz plane. The curve relative to the yz plane corresponds to BPM since the direction of propagation is parallel to the domains.

Fig. 3.5 gives the energy of the beam generated by type I SHG at 1.064 μm recorded as a function of θ in the plane $\phi = 0°$. According to the uniaxial symmetry, the BPM tuning curve of type I SHG given in Fig. 3.3 is not specific to $\phi = 90°$ but it is the same for any other value of ϕ. This was verified by the measurement of the phase-matching angles at the fixed fundamental wavelength $\lambda_\omega = 1.064\,\mu$m. This measurement presented in Fig. 3.6 well shows that θ_{BPM} is the same for any value of ϕ, which is not the case for AQPM, also shown in Fig. 3.6. These observations corroborate that the ϕ angle has no influence on the BPM phase-matching relation 1.24, leading to a conical distribution of the phase-matching loci around the z-axis, while the ϕ angle has an influence on the AQPM phase-matching relation 1.27.

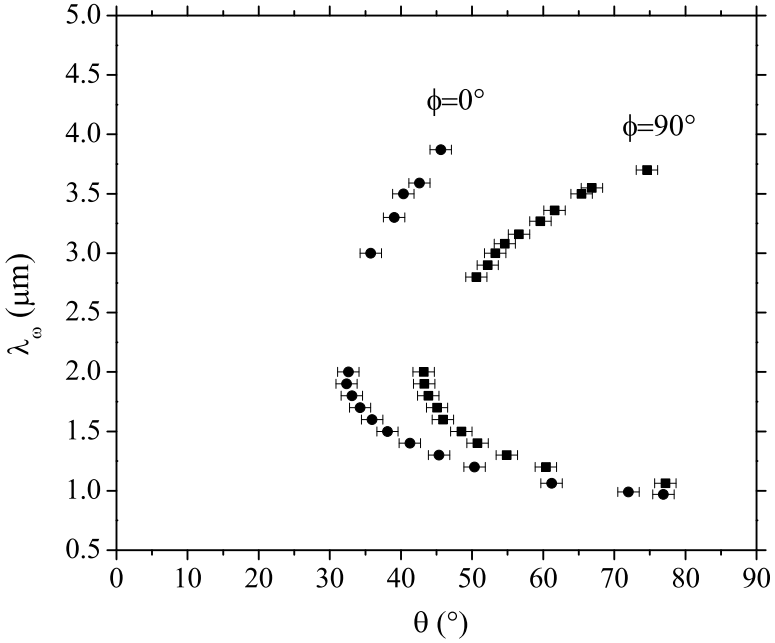

Figure 3.3: Measured type I SHG tuning curves of 5%MgO:PPLN with $\Lambda = 32.2\,\mu$m at $T = 22°C$; the fundamental wavelength λ_ω is given as a function of θ at $\phi = 0°$ and $\phi = 90°$ [32].

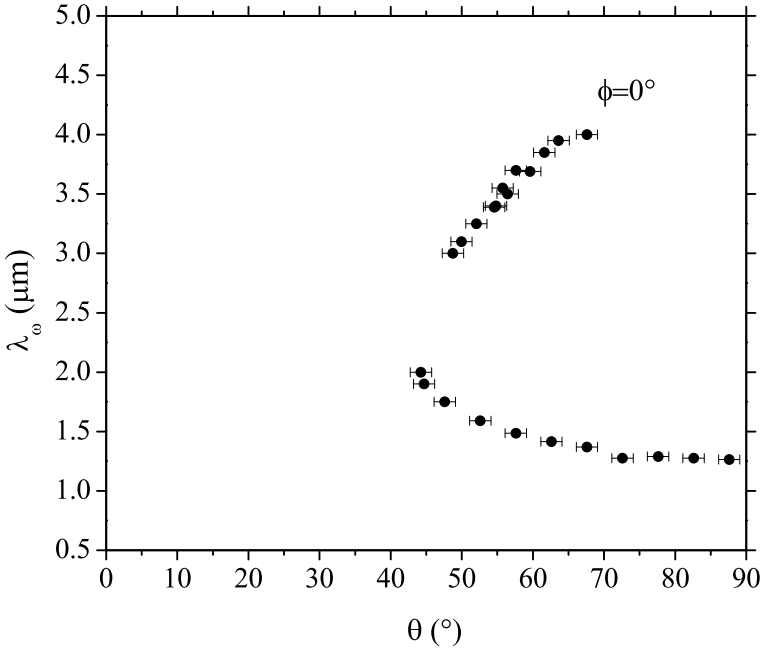

Figure 3.4: Measured type II SHG tuning curve of 5%MgO:PPLN with $\Lambda = 32.2\,\mu$m at $T = 22°C$; the fundamental wavelength λ_ω is given as a function of θ at $\phi = 0°$.

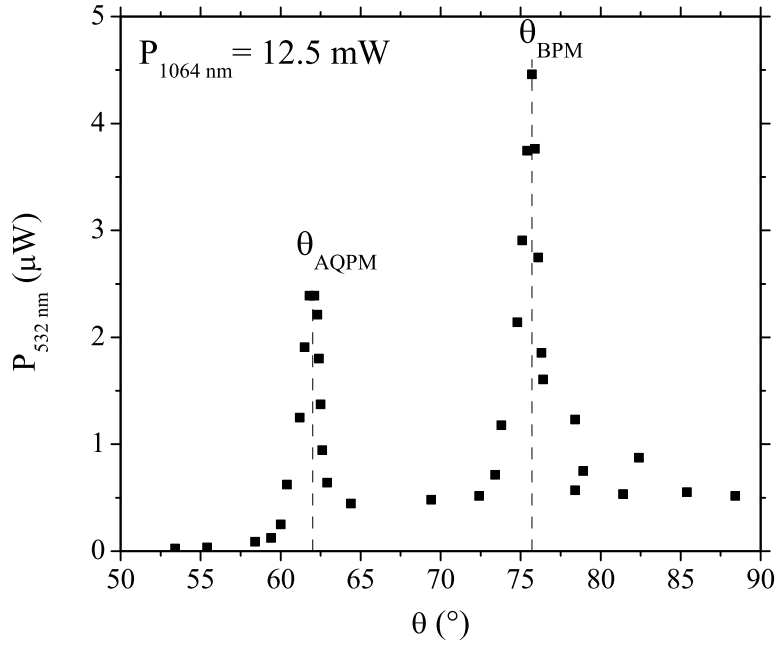

Figure 3.5: Second-harmonic power at 532 nm generated by type I AQPM and BPM SHG in the xz plane of a sphere of 5%MgO:PPLN. The angles θ_{AQPM} and θ_{BPM} correspond respectively to the AQPM and BPM directions in the considered plane.

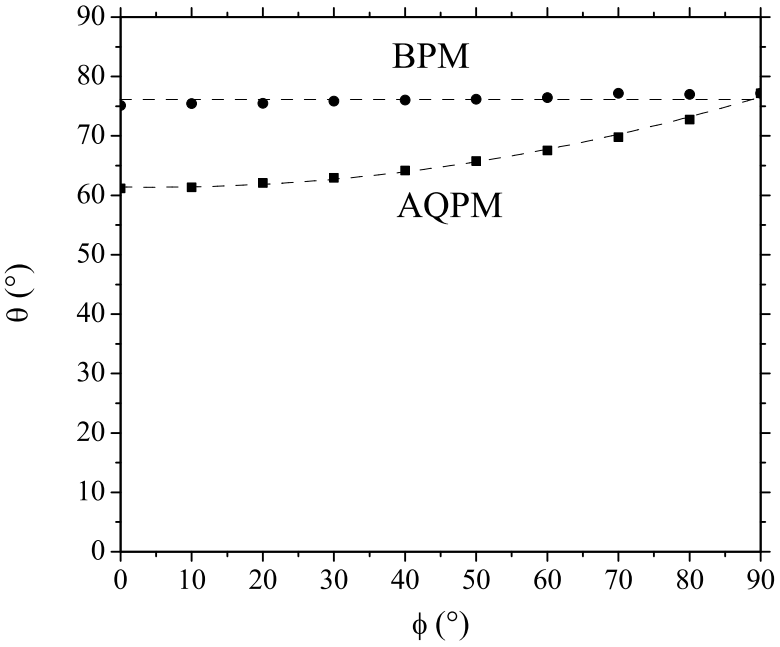

Figure 3.6: Measured curves of BPM and AQPM type I SHG at $\lambda_\omega = 1064\,\mathrm{nm}$ in a sphere of 5%MgO:PPLN. The dashed lines are guides for the eyes.

3.3.2 Type I and II difference-frequency generation

In the following, we use the notation DFG $(\lambda_p, \lambda_s, \lambda_i)$ for DFG $(\lambda_p^{-1} - \lambda_s^{-1} = \lambda_i^{-1})$, where λ_p, λ_s and λ_i are the pump, signal and idler wavelengths respectively with $\lambda_p < \lambda_s < \lambda_i$. The signal wave is defined as the wave that is incident together with the pump wave at $\lambda_p = 1.064\,\mu$m. The temporal overlap between pump and signal was realized thanks to a delay line between the two incident beams in order to realize the parametric generation.
By using the experimental setup described in Fig. 2.2, we measured the AQPM tuning curves at $T = 22°C$ of type I DFG $(\lambda_p^e, \lambda_s^e, \lambda_i^o)$ and type II DFG $(\lambda_p^e, \lambda_s^o, \lambda_i^e)$ in the full space of 5%MgO:PPLN, indices (o) and (e) standing for the ordinary and extraordinary polarizations respectively [32]. The measurement of types I and II DFG in the xz plane is presented in Fig. 3.7.

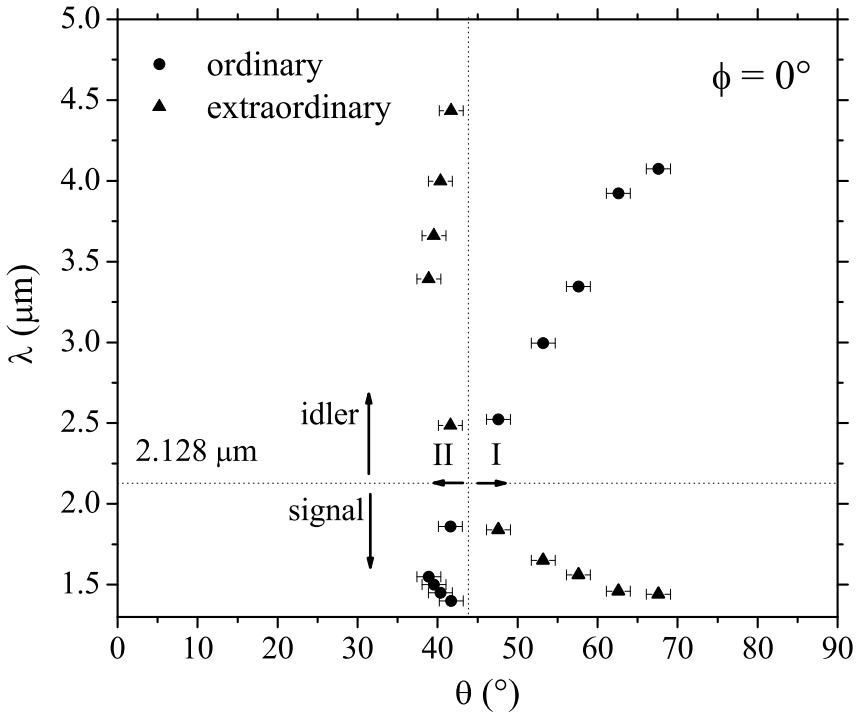

Figure 3.7: Measured types I and II DFG in a sphere of 5%MgO:PPLN with a pump at $1.064\,\mu$m; λ stands for the signal or idler wavelengths plotted as a function of θ at $\phi = 0°$.

Type I is obtained by choosing an ordinary polarization for the signal beam since type II corresponds to an extraordinary polarized signal beam. In both cases, we notice that an idler beam can be generated in the second atmospheric transparency band.

3.3.3 Refinement of the Sellmeier equations of 5%MgO:PPLN

From the momentum conservation 1.27, our experimental data are relatively well modelized by using the following Sellmeier equation with the coefficients of Ref. [22] given in Tab. 3.1:

$$n^i(\lambda) = \left(A^i + \frac{B^i}{\lambda^2 - C^i} - D^i \lambda^2 \right)^{1/2} \tag{3.1}$$

where i = (o, e) is relative to the ordinary and extraordinary principal refractive indices.

Sellmeier coefficients	Reference [22]	Present work [32]
A^o	4.87620	4.89789
B^o	0.11554	0.14720
C^o	0.04674	0.02719
D^o	0.03312	0.03305
A^e	4.54690	4.52222
B^e	0.09478	0.09194
C^e	0.04439	0.07475
D^e	0.02672	0.03647

Table 3.1: Sellmeier coefficients relative to the ordinary (o) and extraordinary (e) principal refractive indices of 5%MgO:PPLN at $T = 22°C$.

But the simultaneous fit of all our experimental data allowed us to refine the Sellmeier equations of this material. We used a non linear least-squares fit, and Eqs. 1.27 and 3.1. The fit was a numerical calculus using the Levenberg-Marquardt algorithm encoded with MATLAB: it led to a really much better agreement with our experimental data compared with calcultations from the previous Sellmeier equations of Refs. [22] and [33] as shown in Fig. 3.8 and 3.9. The corresponding Sellmeier coefficients are given in Tab. 3.1; they are the best set of coefficients for the considered sample [32]. Since the precision of our angular measurements is $\pm 1°$, the new refractive indices have a typical accuracy $\Delta n^{o,e}/n^{o,e}$ better than 10^{-4} over the entire transparency range of the crystal, which could be easily verified by numerical calculations using Eq. 1.27.

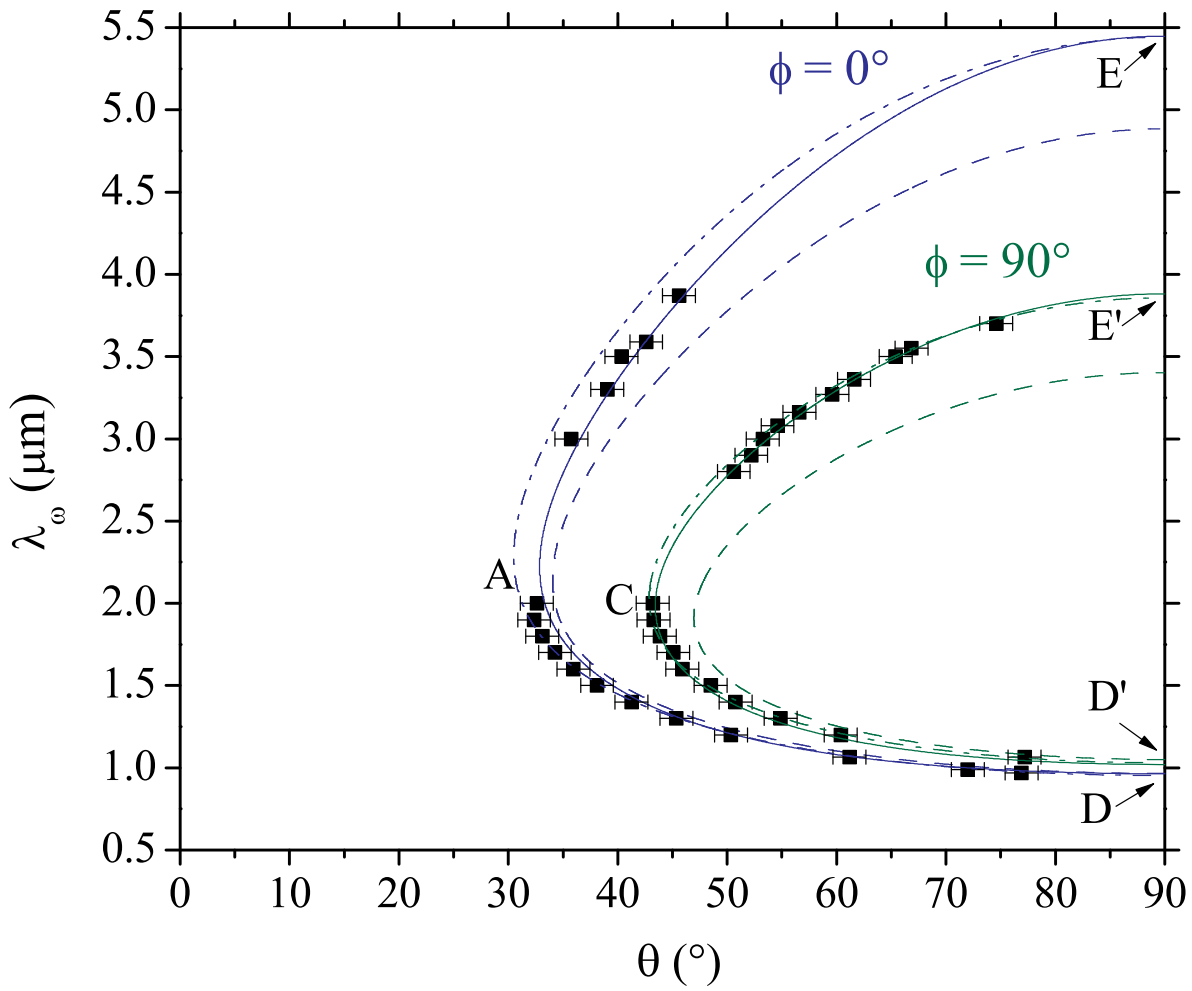

Figure 3.8: Type I SHG AQPM tuning curves of 5%MgO:PPLN with $\Lambda = 32.2\,\mu$m; the fundamental wavelength λ_ω is given as a function of θ at $\phi = 0°$ and $\phi = 90°$. Dots stand for experimental data, dashed lines and dashed doted lines correspond to calculations from Sellmeier equations of Refs. [22] and [33] respectively and continuous lines are the fit of the experimental data. Vertical tangents of the curves at points A and C correspond to spectrally non critical interactions. Points D and E correspond to the x direction while points D' and E' correspond to the y direction.

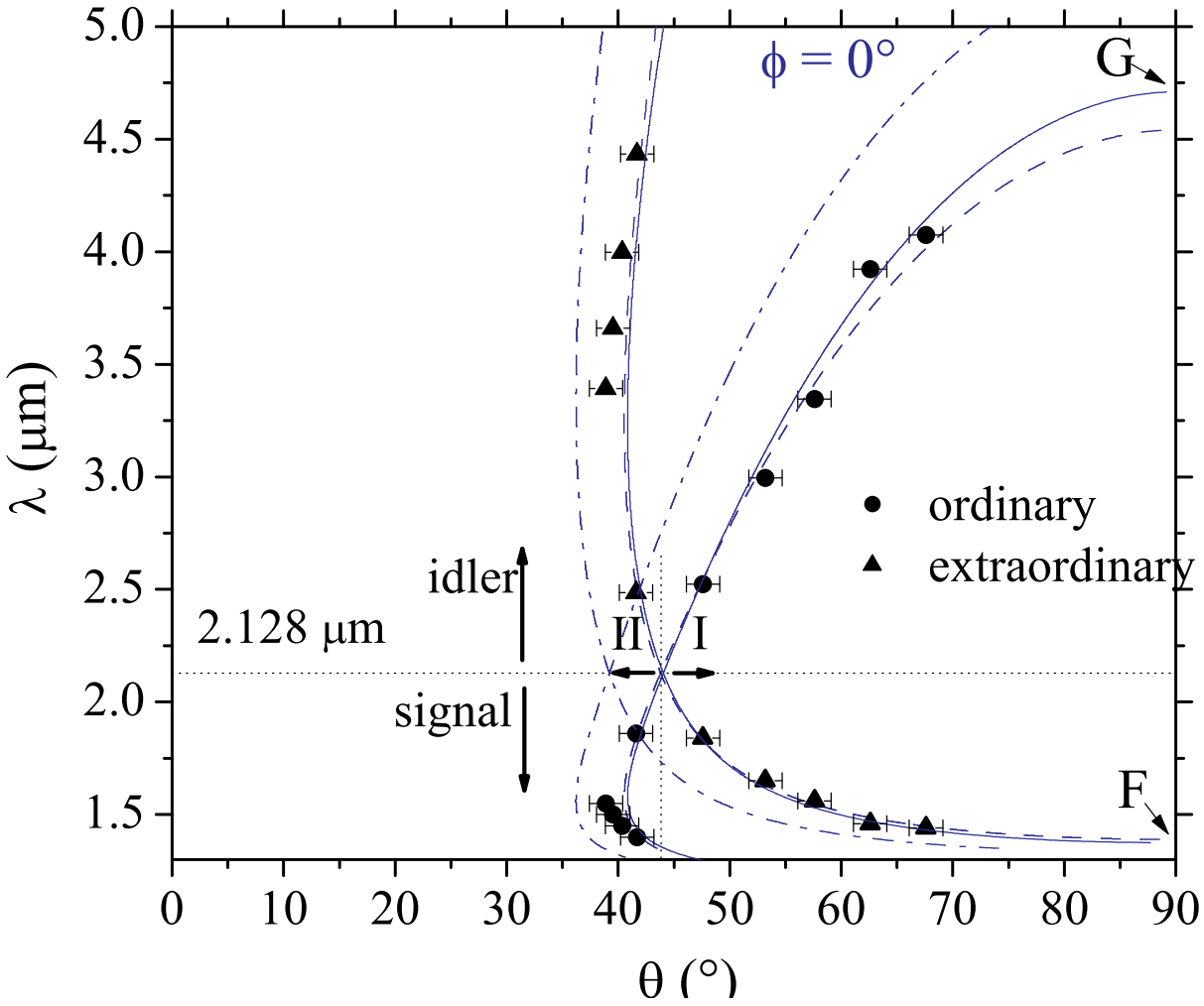

Figure 3.9: Type I and II DFG AQPM tuning curves of 5%MgO:PPLN with $\Lambda = 32.2\,\mu$m with a pump at $1.064\,\mu$m; λ stands for the signal or idler wavelengths plotted as a function of θ at $\phi = 0°$. The dots correspond to experimental data, the dashed lines and the dashed doted lines correspond to calculations from Sellmeier equations of Refs. [22] and [33] respectively and the continuous lines to the fit of the experimental data. Points F and G correspond to the x direction.

3.3.4 General analysis of the AQPM tuning range of 5%MgO:PPLN

The benefit of AQPM over BPM in term of tuning potentiality can be evaluated in Fig. 3.8 in the case of type I SHG. While BPM allows a tunability of the wavelength from $1.02\,\mu$m (dot D') to $3.88\,\mu$m (dot E'), AQPM allows a tunability between $0.96\,\mu$m (dot D) and $5.45\,\mu$m (dot E). The maximum tuning range of AQPM is obtained in the xz plane corresponding to $\phi = 0°$. It is also interesting to compare this tuning range of AQPM in the xz plane with the tuning range of the xy plane that could be interesting since the corresponding walk-off angle is nil. This comparison is shown in Fig. 3.10.

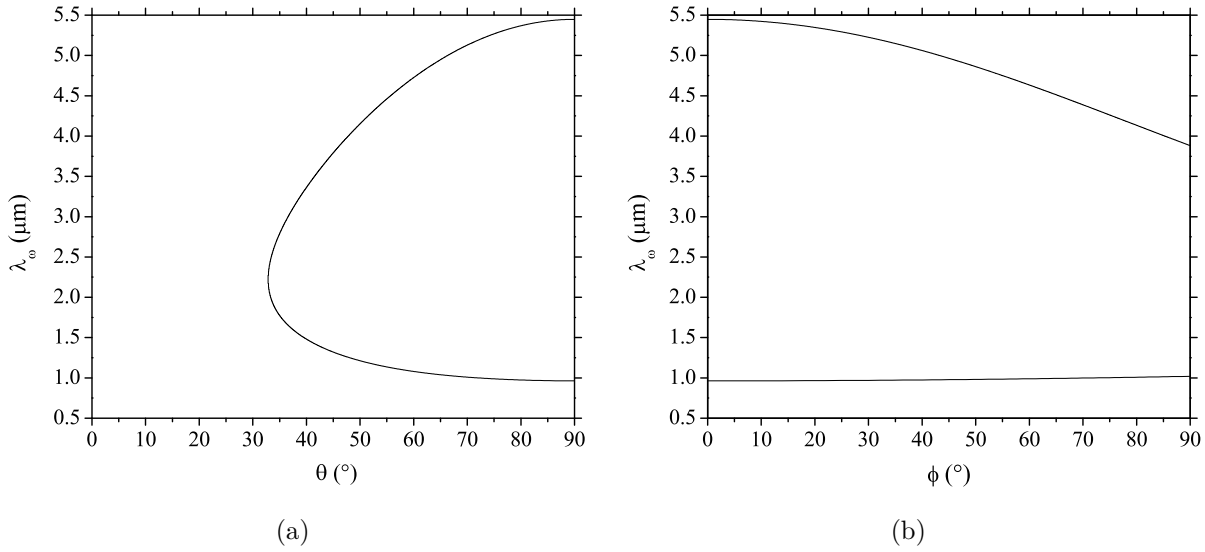

(a) (b)

Figure 3.10: Calculated tuning curves of type I SHG in the xz plane (a) and in the xy plane (b) of 5%MgO:PPLN with $\Lambda = 32.2\,\mu$m.

We notice that AQPM in the xy plane is far less attractive in term of tunability since it does not enable to realize type I SHG in the range $1.02 - 3.88\,\mu$m, which exactly corresponds to the range accessible by pure BPM. This limitation is due to the fact that there is no tunability of the birefringence in the xy plane.

The wavelength range between points D and E of Fig. 3.8 is obtained with a grating period of $\Lambda = 32.2\,\mu$m corresponding to the sample we studied, but it can be also interested to see how this interval evolves as a function of the principal grating period Λ. From our refined Sellmeier equations given in table 3.1, it is possible to have a reliable full "picture" of the tunability of 5%MgO:PPLN [32]. The example of SHG is given in Fig. 3.11 where the distance between the upper part and the lower part of the curves at a given Λ gives the

maximum wavelength range which is accessible for a given type by varying the θ angle in the xz plane.

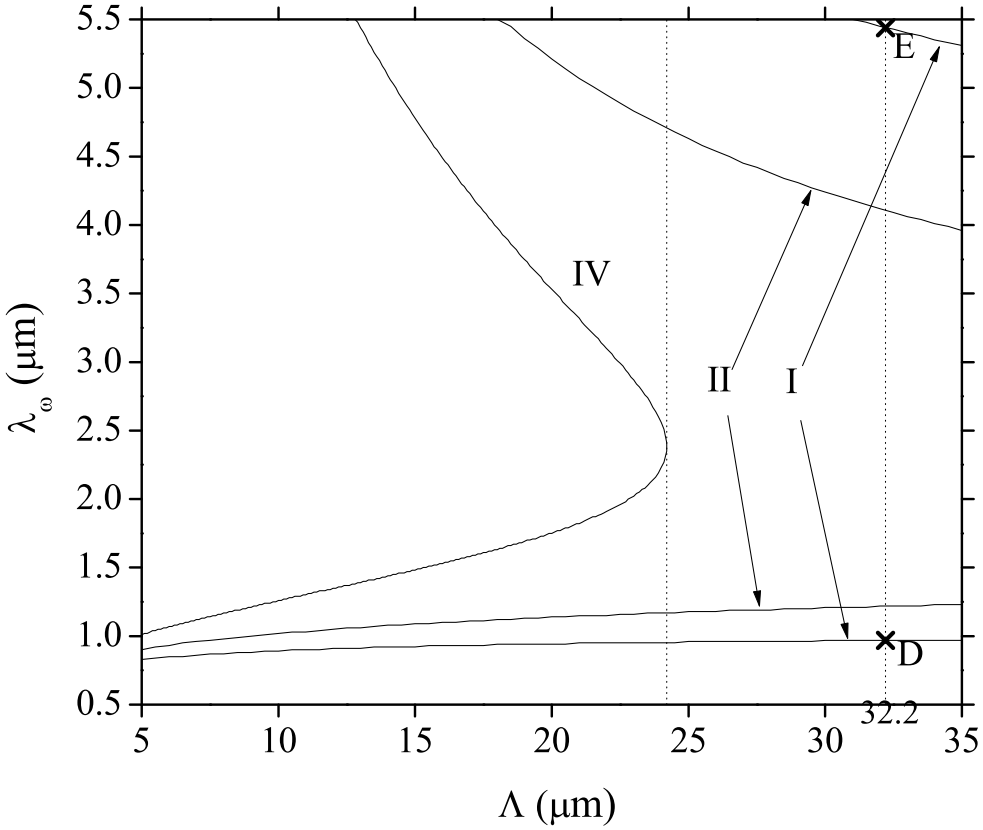

Figure 3.11: Calculated tuning ranges of types I, II and IV SHG in the xz plane of 5%MgO:PPLN as a function of the principal grating period Λ. λ_ω is the fundamental wavelength. Points D and E refer to particular points of the tuning curve of Fig. 3.8.

Fig. 3.11 shows that types I and II SHG are allowed for any value of Λ, while type IV SHG $(\lambda^e_\omega, \lambda^e_\omega, \lambda^e_{2\omega})$ is possible only if $\Lambda \leq 24\,\mu$m.

Furthermore, we see that it is necessary to have $\Lambda \leq 13\,\mu$m in order to reach $\lambda_\omega = 5.5\,\mu$m, which is the infrared cutoff wavelength of the crystal. For more legibility, we did not plot the curves relative to types V $(\lambda^o_\omega, \lambda^o_\omega, \lambda^o_{2\omega})$, VI $\equiv$ VII $(\lambda^o_\omega, \lambda^e_\omega, \lambda^o_{2\omega})$ and VIII $(\lambda^e_\omega, \lambda^e_\omega, \lambda^o_{2\omega})$ SHG; type V has a behaviour comparable to the one of type IV, and the other types are possible only at very small periodicities that are not yet accessible because of technological difficulties. Fig. 3.11 also shows that type I is the most favourable configuration for a broad wavelength tuning of the SHG.

Fig. 3.12 illustrates the case of DFG. It is obtained using Eq. 1.27 and 3.1 and our Sellmeier coefficients given in Tab. 3.1.

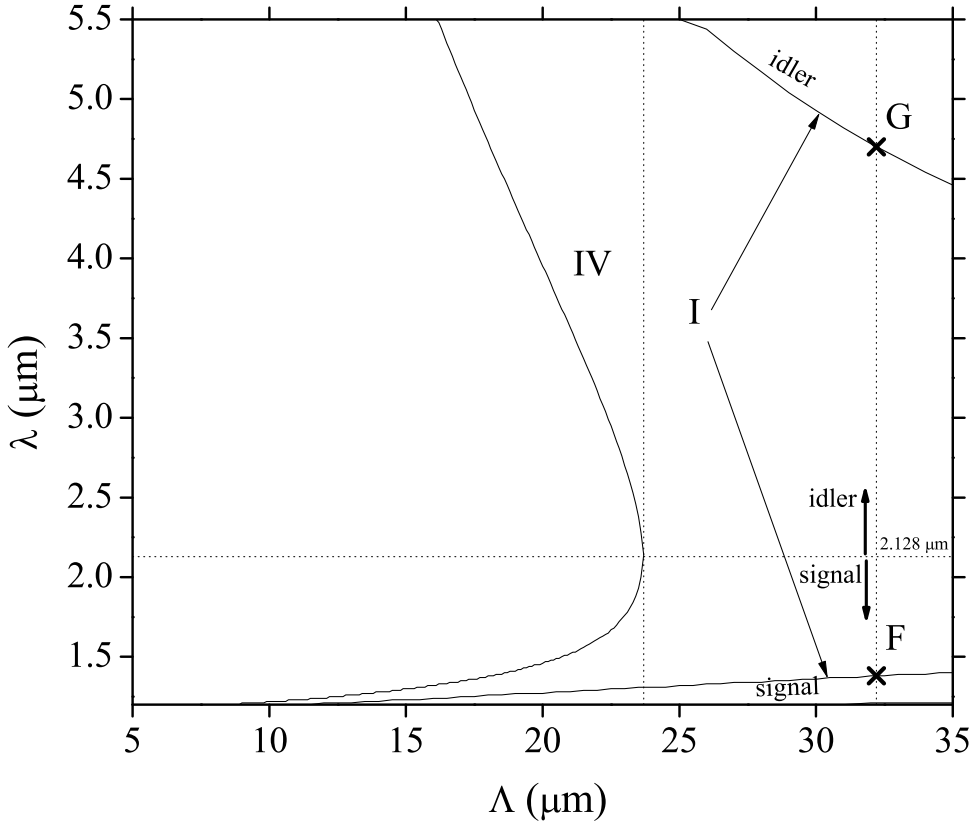

Figure 3.12: Calculated tuning ranges of types I, II and IV DFG in the xz plane of 5%MgO:PPLN as a function of the principal grating period Λ. Points F and G refer to particular points of the tuning curve of Fig. 3.9.

We see that type I and type II are also the most favourable for wavelength tuning: the infrared cutoff can be reached with a grating of $\Lambda = 25\,\mu$m with type I as against $\Lambda = 16\,\mu$m with type IV. It is also important to note that the larger the grating is, the thicker the sample can be grown. But the superiority of types I and II must be moderated by the fact that the corresponding effective coefficient involving d_{yyy} and d_{zxx} is of about seven times lower than d_{zzz} that correponds to type IV [8], as it will be shown in paragraph 3.5.

3.4 Acceptances

We have shown that AQPM opens new possibilities in term of acceptances with respect to BPM and QPM. Measurements were done to prove the interesting properties predicted by the theory [32, 34].

3.4.1 Spectral acceptance

The spectral acceptance was measured along each determined type I SHG AQPM directions given in Fig. 3.3. For that we measured the variation of the intensity of the generated wave as a function of the fundamental wavelength λ_ω. An example of such a measurement is shown in Fig. 3.13.

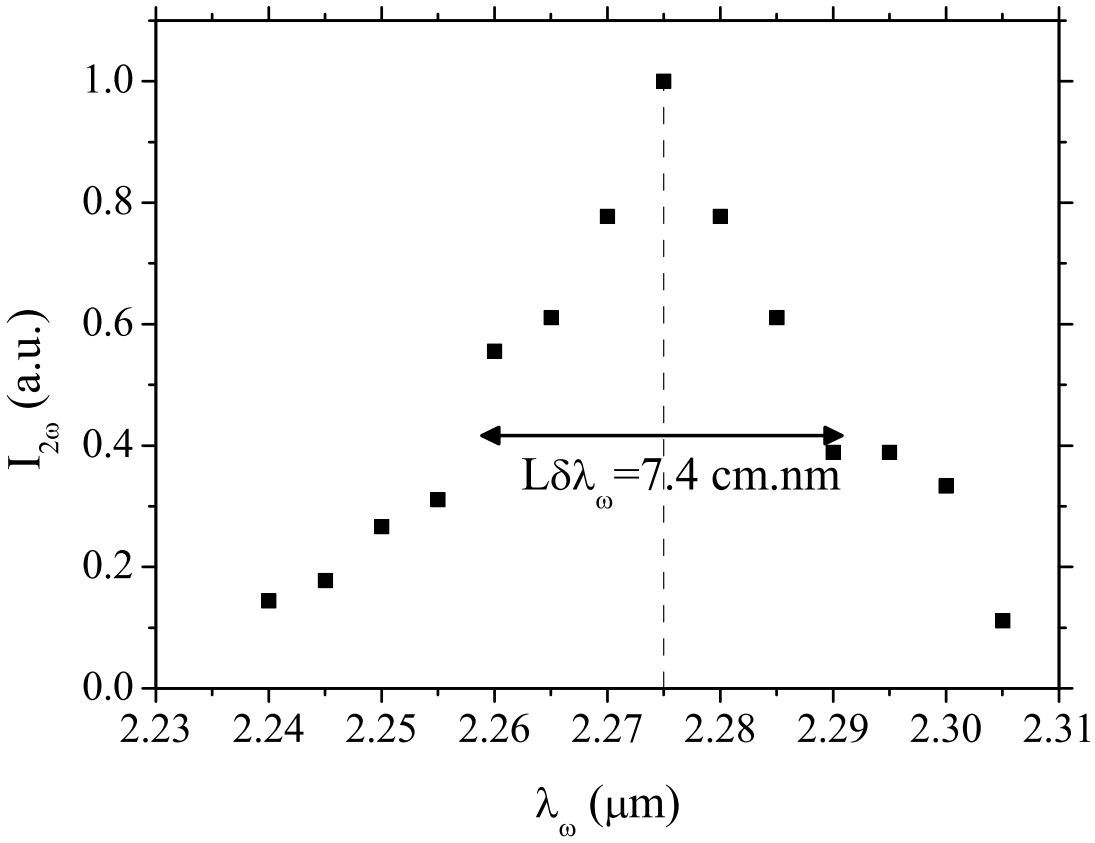

Figure 3.13: Measured AQPM type I second harmonic intensity $I_{2\omega}$ as a function of the fundamental wavelength λ_ω in the direction ($\theta = 31.4°$, $\phi = 0°$) of the 5%MgO:PPLN sphere of diameter 3.99 mm and grating period $\Lambda = 32.2\,\mu$m; the AQPM fundamental wavelength is $\lambda_\omega = 2.275\,\mu$m.

Fig. 3.14 shows the measured spectral acceptance along the whole AQPM curve of type I SHG at $\phi = 0°$ [32]. In the xz plane, $L\delta\lambda_\omega$ exhibits a maximum value of about $0.08\,\mathrm{cm}\cdot\mu\mathrm{m}$

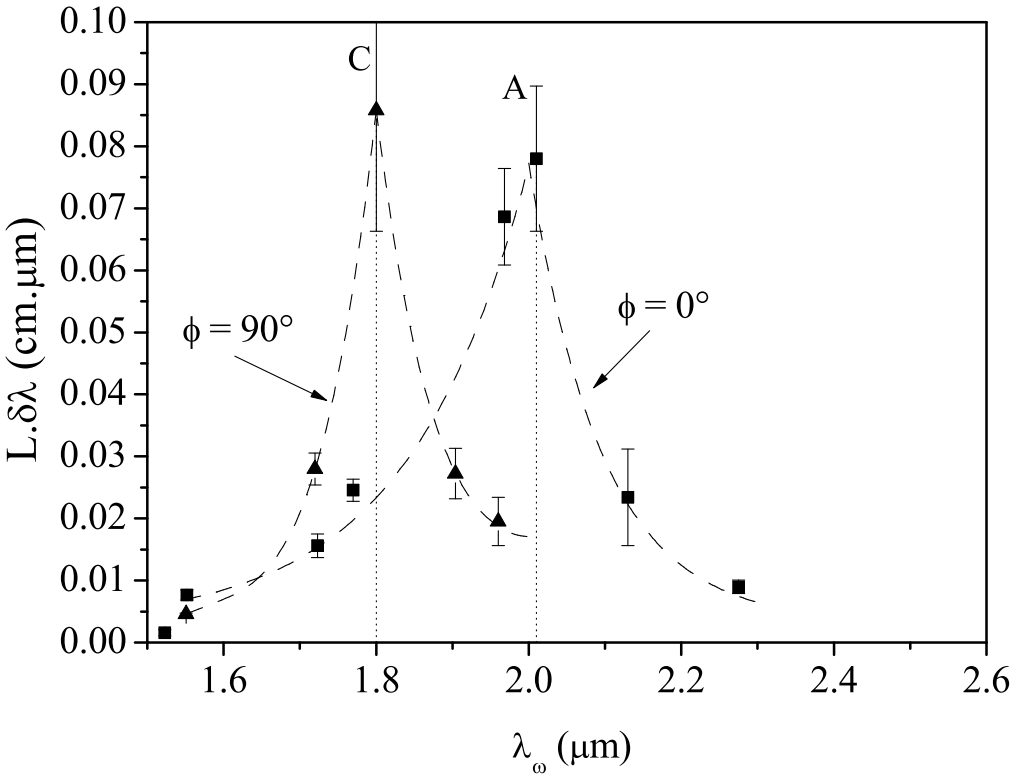

Figure 3.14: Type I SHG AQPM spectral acceptance measured in the xz plane ($\phi = 0°$) and yz plane ($\phi = 90°$) of a 5%MgO:PPLN sphere with $\Lambda = 32.2\,\mu$m as a function of the fundamental wavelength λ_ω. The doted line is a guide for the eye. The peak values denoted by A and C correspond to the vertical tangents of the two tuning curves of Fig. 3.8.

at $\lambda_\omega = 2.02\,\mu$m; this particular wavelength corresponds to the vertical slope of the curve of Fig. 3.8 marked out with dot A. Furthermore, by varying the ϕ angle from 0° to 90°, the wavelength associated to the vertical slope reaches $\lambda_\omega = 1.8\,\mu$m for $\phi = 90°$, as shown in Fig. 3.14. In this way, at $\Lambda = 32.2\,\mu$m and thanks to a continuous variation of the ϕ angle, AQPM type I SHG can exhibit a maximal acceptance over a wide spectral range, *i.e.* $2.09\,\mu\mathrm{m} < \lambda_\omega < 2.22\,\mu\mathrm{m}$. These experimental results were confirmed by using the refined Sellmeier equations with the coefficients given in table 3.1, as shown in Fig. 3.15 [34].

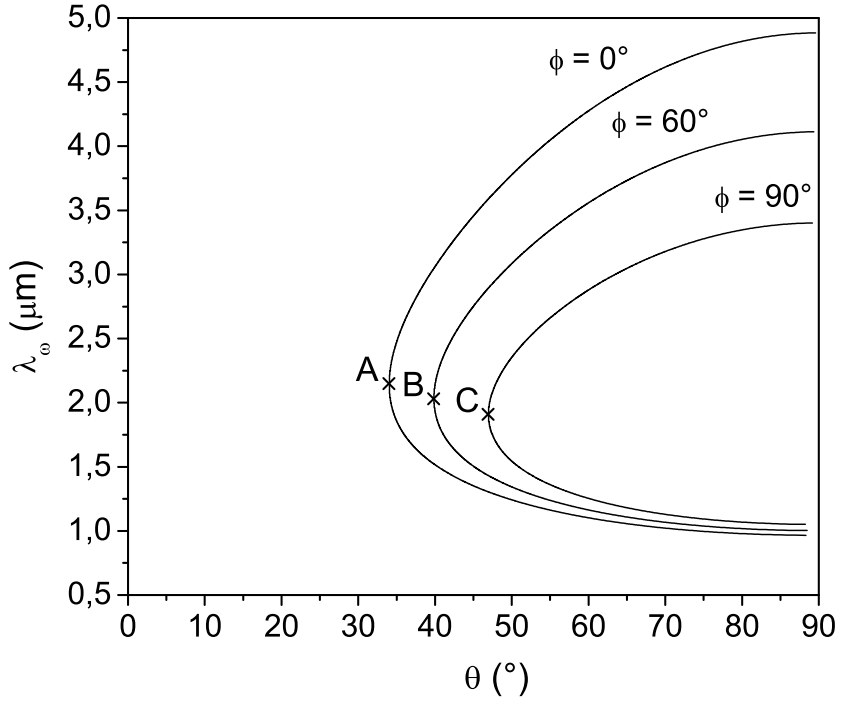

(a)

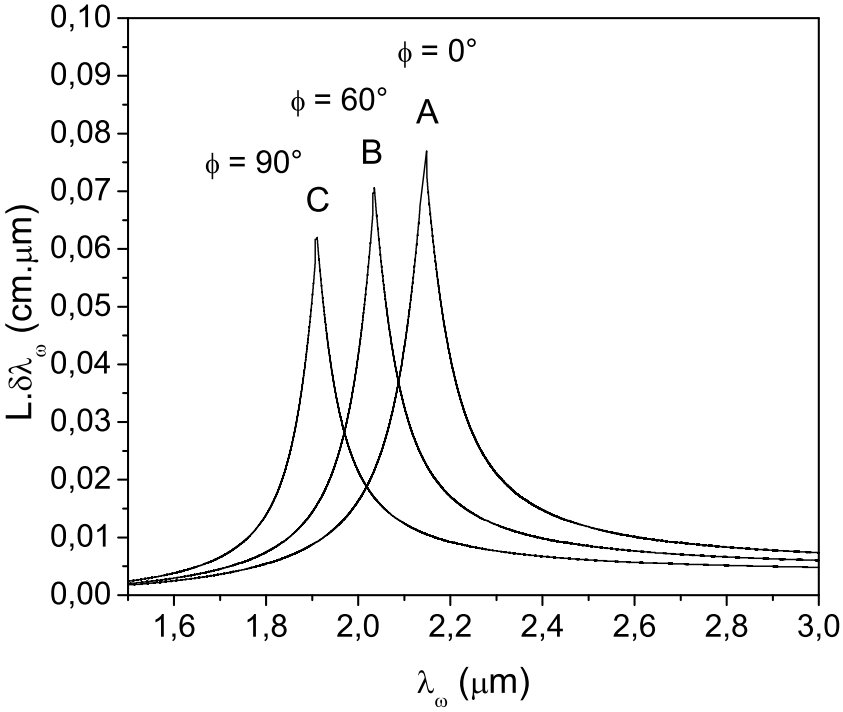

(b)

Figure 3.15: Calculated AQPM curves of type I SHG in 5%MgO:PPLN with $\Lambda = 32.2\,\mu$m at three different ϕ angles (a) and their correponding spectral acceptances (b). Points A, B and C are three points of the continuum for which the spectral acceptance is maximal.

The tuning of the wavelength allowing a maximal spectral acceptance can be well understood by considering the expression of the AQPM phase-mismatch Δk_{AQPM} given by Eq. 1.27. One can distinguish the term $\Delta k_{\mathrm{crystal}}$ specific to the crystal, and $\Delta k_{\mathrm{grating}}$ depending only on the grating periodicity [34]:

$$\begin{aligned} \Delta k_{\mathrm{crystal}} &= 2\pi\left[\frac{n(\lambda_3,\theta)}{\lambda_3} - \frac{n(\lambda_1,\theta)}{\lambda_1} - \frac{n(\lambda_2,\theta)}{\lambda_2}\right] \\ \Delta k_{\mathrm{grating}} &= 2\pi\left|\frac{\Lambda}{\sin(\theta)\ \cos(\phi)}\right| \end{aligned} \tag{3.2}$$

Then by expanding Δk in a Taylor series following Eq. 1.28, it comes:

$$\frac{2\pi}{L} = \left(\frac{\partial(\Delta k_{\mathrm{crystal}} + \Delta k_{\mathrm{grating}})}{\partial\lambda}\right)_{\lambda_{\mathrm{AQPM}}} \delta\lambda + \frac{1}{2}\left(\frac{\partial^2(\Delta k_{\mathrm{crystal}} + \Delta k_{\mathrm{grating}})}{\partial\lambda^2}\right)_{\lambda_{\mathrm{AQPM}}} (\delta\lambda)^2 + \dots \tag{3.3}$$

The grating term $\Delta k_{\mathrm{grating}}$ does not depend on the wavelength, so that:

$$\left(\frac{\partial\Delta k_{\mathrm{grating}}}{\partial\lambda}\right) = \left(\frac{\partial^2\Delta k_{\mathrm{grating}}}{\partial\lambda^2}\right) = 0 \tag{3.4}$$

Thus Eq. 3.3 becomes:

$$\frac{2\pi}{L} = \left(\frac{\partial(\Delta k_{\mathrm{crystal}})}{\partial\lambda}\right)_{\lambda} \delta\lambda + \frac{1}{2}\left(\frac{\partial^2(\Delta k_{\mathrm{crystal}})}{\partial\lambda^2}\right)_{\lambda} (\delta\lambda)^2 + \dots \tag{3.5}$$

It is then interesting to come back to the tuning curve of Fig. 3.15. According to Eq. 1.29, the A,B,C points correspond to a spectral non-criticity, defined by:

$$\left(\frac{\partial(\Delta k_{\mathrm{crystal}})}{\partial\lambda}\right)_{\lambda_{\mathrm{A,B,C}}} = 0 \tag{3.6}$$

In these particular situations, the value of the spectral acceptance is maximum. Note that the crystal contribution $\Delta k_{\mathrm{crystal}}$ does not vary as a function of ϕ since 5%MgO:PPLN is an uniaxial medium. But $\Delta k_{\mathrm{grating}}$ does, as shown by Eq. 1.26. It could then seem paradoxal to have a variation of the wavelength corresponding to a maximal spectral acceptance, *e.g.* $\lambda_A \neq \lambda_B \neq \lambda_C$, with the ϕ angle. Actually it is due to the fact that the tuning curves depend on ϕ, which comes from the variation of the effective grating period Λ_{eff} with ϕ according to Eq. 1.26. The same kind of calculations were performed for type II SHG and types I and II DFG using our refined Sellmeier equations. The corresponding curves are

plotted in Figs. 3.16 and 3.17 [34].

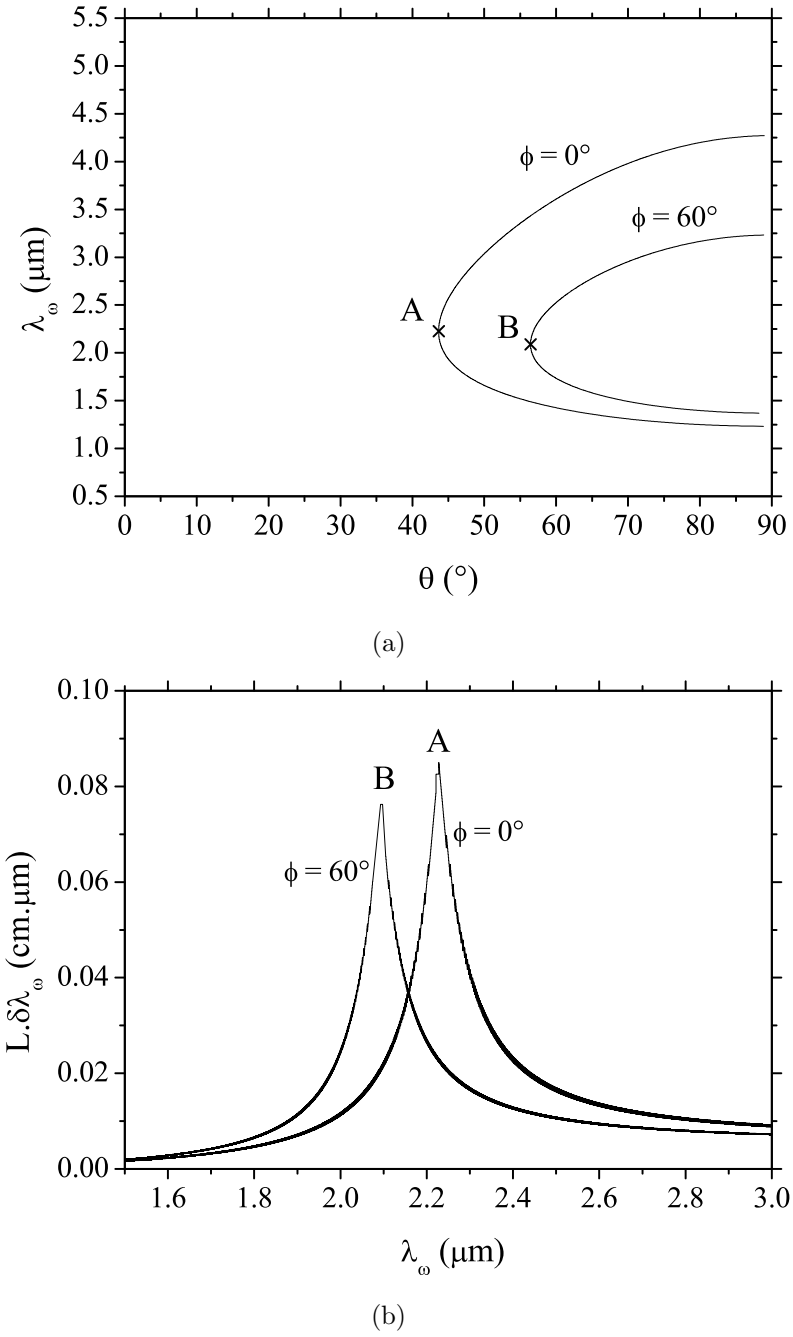

Figure 3.16: Calculated AQPM curves of type II SHG in 5%MgO:PPLN with $\Lambda = 32.2\,\mu$m at two different angles (a), and their corresponding spectral acceptances (b). Points A and B are two points of the continuum for which the spectral acceptance is maximal.

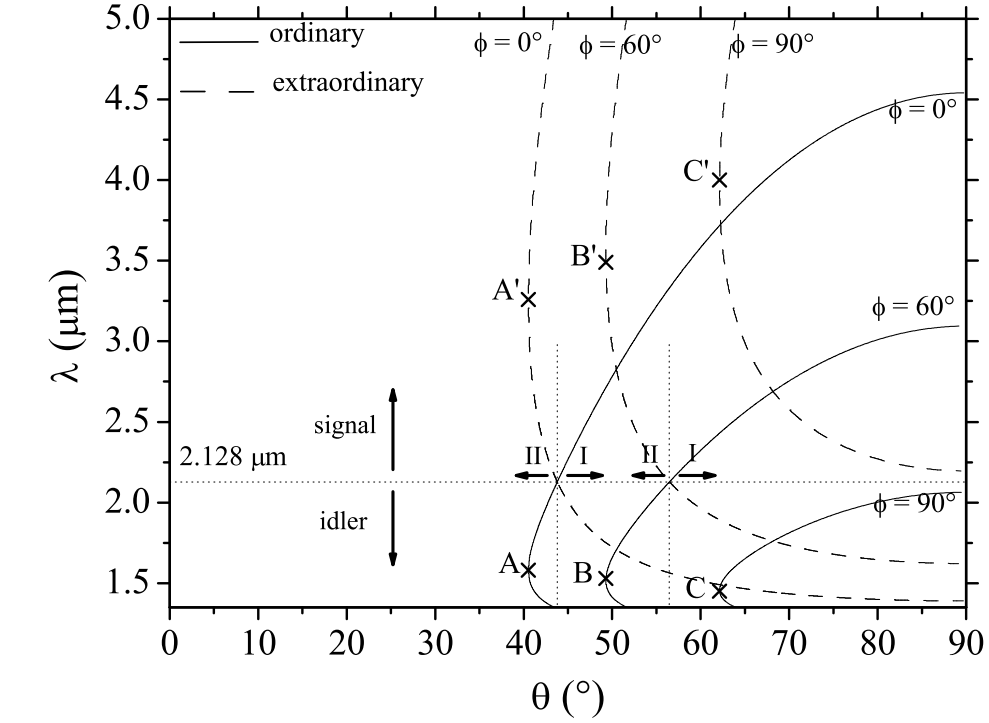

(a)

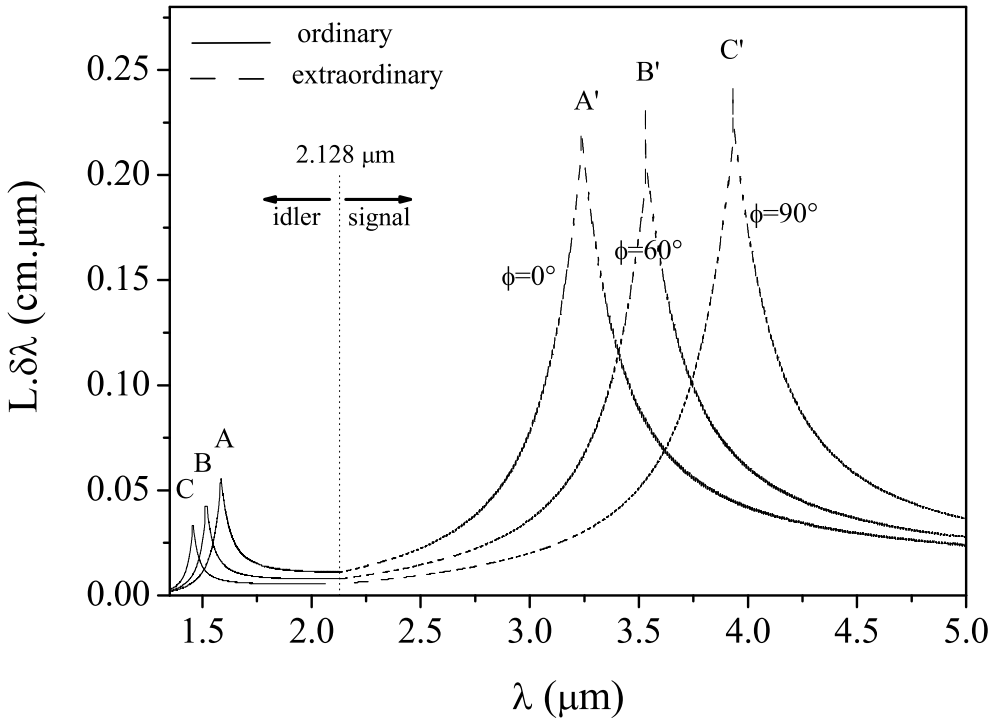

(b)

Figure 3.17: Calculated AQPM cures of types I and II DFG at three different ϕ angles (a), and their corresponding spectral acceptances (b). Points (A, A'), (B, B') and (C, C') belong to the continuum for which the spectral acceptance is maximal.

It is also interesting to study how the interval over which the maximal spectral acceptance can be tuned evolves with the grating period. The hatched zones in Fig. 3.18 show how this interval increases as the grating period decreases, and how types I and II exhibit ranges that are complementary and wider than those of type IV. Such large spectral acceptance ranges also exist for DFG and are presented in Fig. 3.19.

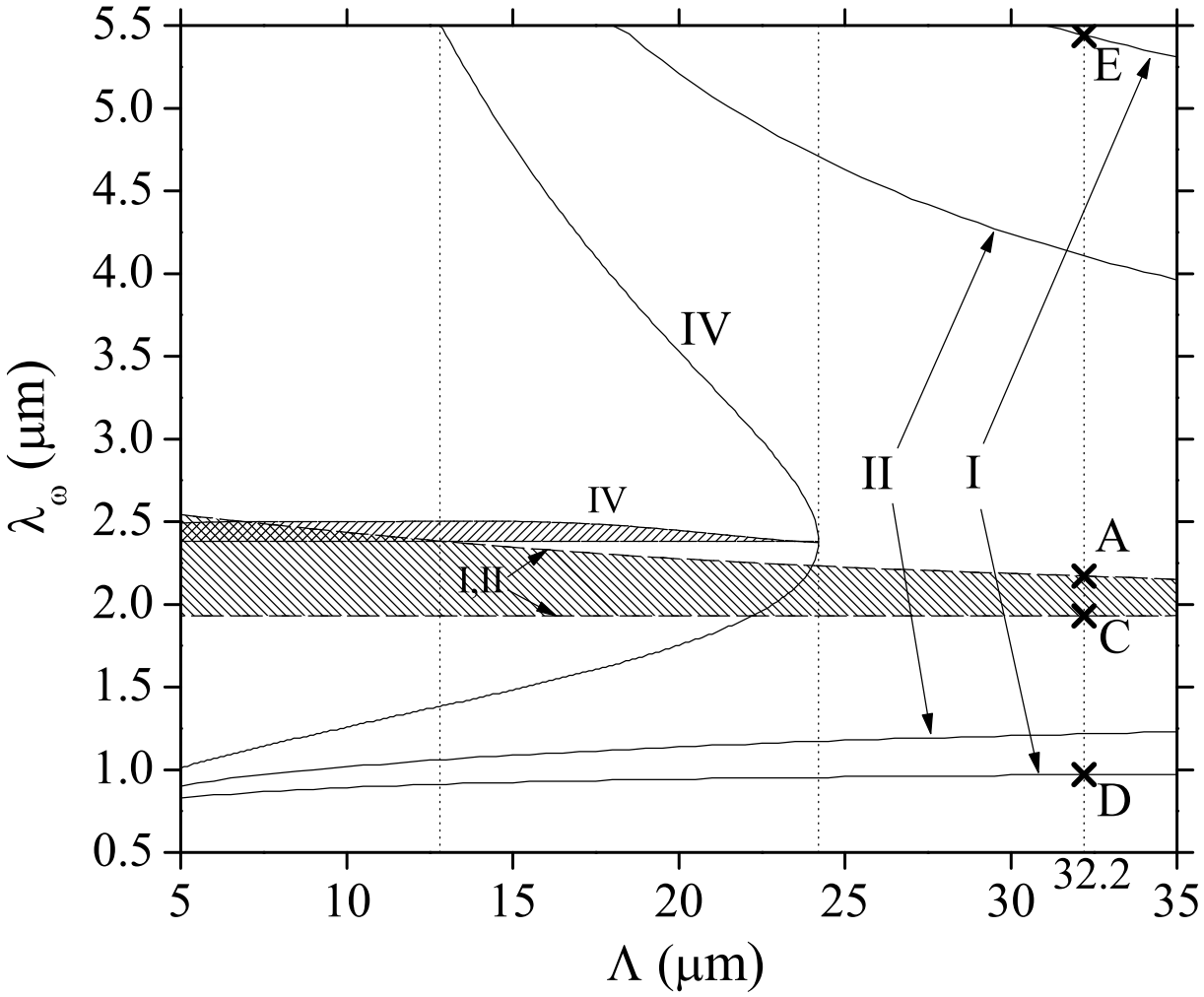

Figure 3.18: Fundamental wavelength tuning ranges (continuous lines) and maximal acceptance domains (hatched zones) of types I, II and IV AQPM SHG calculated in the xz plane of 5%MgO:PPLN, as a function of the grating periodicity Λ. Dots A, B, C, D refer to particular points of the tuning curves of Fig. 3.8.

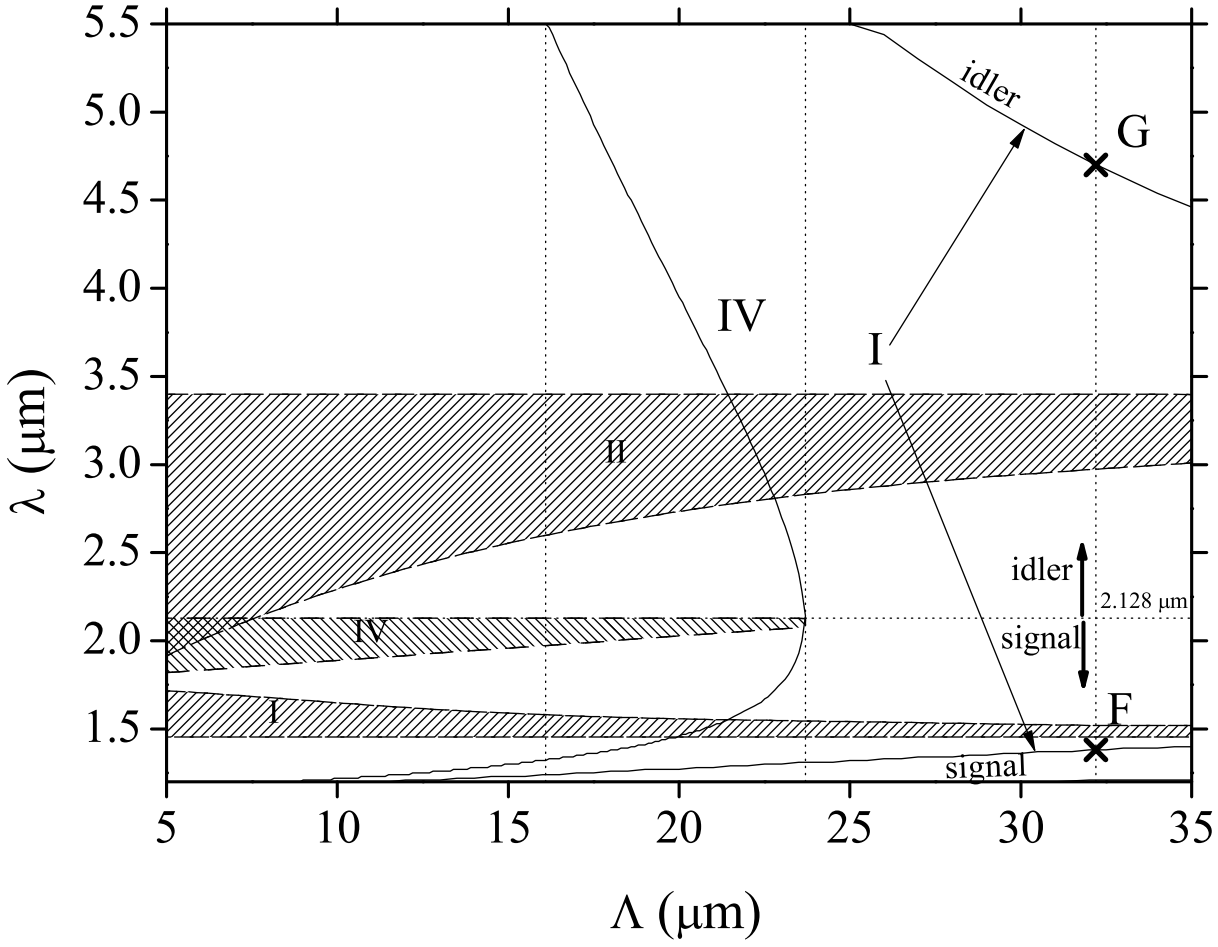

Figure 3.19: Signal and idler wavelengths tuning ranges (continuous lines) and maximal acceptance domains (hatched zones) of types I, II and IV AQPM DFG calculated in the xz plane of 5%MgO:PPLN, as a function of the grating periodicity Λ. The pump wavelength is $\lambda_p = 1.064\,\mu$m. Dots F and G refer to particular points of the tuning curves of Fig. 3.9.

3.4.2 Angular acceptances

At the opposite of the spectral acceptance, the angular acceptances $L\delta\theta$ and $L\delta\phi$ have a contribution of the grating coming from both the first and second orders of the Taylor series expansion, *i.e.*:

$$\begin{aligned}\left(\frac{\partial(\Delta k_{\text{grating}})}{\partial\theta}\right)_{\theta_{\text{AQPM}}} &= -\frac{\cos(\theta_{\text{AQPM}})\cos(\phi_{\text{AQPM}})}{\Lambda} \\ \left(\frac{\partial(\Delta k_{\text{grating}})}{\partial\phi}\right)_{\phi_{\text{AQPM}}} &= \frac{\sin(\theta_{\text{AQPM}})\sin(\phi_{\text{AQPM}})}{\Lambda}\end{aligned} \tag{3.7}$$

and

$$\left(\frac{\partial^2(\Delta k_{\text{grating}})}{\partial\theta^2}\right)_{\theta_{\text{AQPM}}} = \left(\frac{\partial^2(\Delta k_{\text{grating}})}{\partial\phi^2}\right)_{\phi_{\text{AQPM}}} = \frac{\sin(\theta_{\text{AQPM}})\cos(\phi_{\text{AQPM}})}{\Lambda} \tag{3.8}$$

Furthermore due to the uniaxial symmetry, it comes:

$$\left(\frac{\partial(\Delta k_{crystal})}{\partial\phi}\right)_{\phi_{\text{AQPM}}} = \left(\frac{\partial^2(\Delta k_{crystal})}{\partial\phi^2}\right)_{\phi_{\text{AQPM}}} = 0 \tag{3.9}$$

Then $L\delta\phi$ only depends on the grating, while $L\delta\theta$ is governed by both the refractive indices and the grating. The angular acceptances have been numerically calculated from the $\text{sinc}^2\left(\frac{\Delta k(\theta,\phi)\cdot L}{2}\right)$ function for type I SHG (Fig. 3.20), type II SHG (Fig. 3.21), type I DFG (Fig. 3.22) and type II DFG (Fig. 3.23). All the $L\delta\theta$ acceptances are lower at $\phi = 0°$ than at $\phi = 90°$, showing that the effect of the grating period is not favorable for the angular bandwidth. Moreover, unlike BPM for which it was infinite, the $L\delta\phi$ acceptance is limited to values which are comparable to the $L\delta\theta$ acceptance.

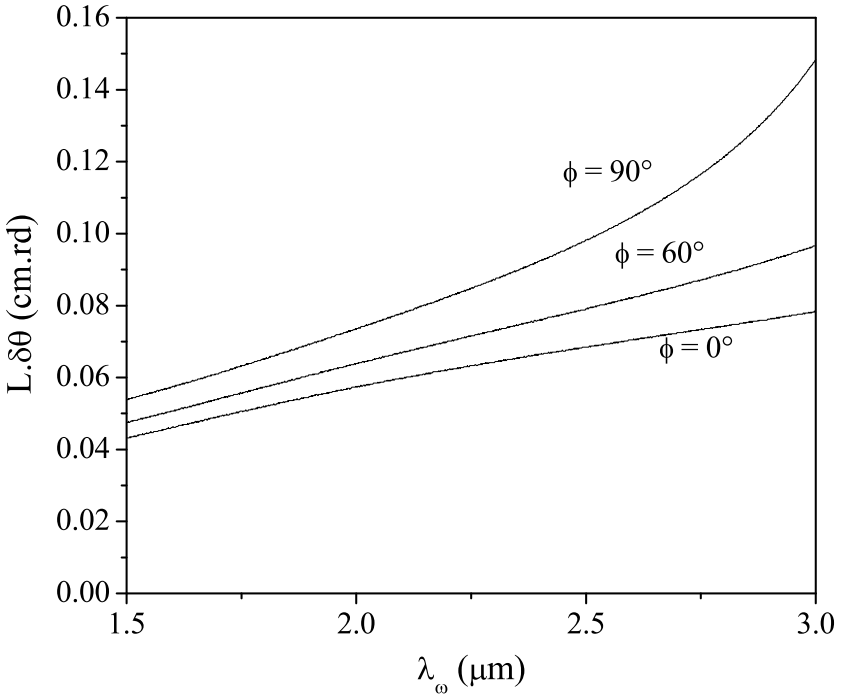

(a)

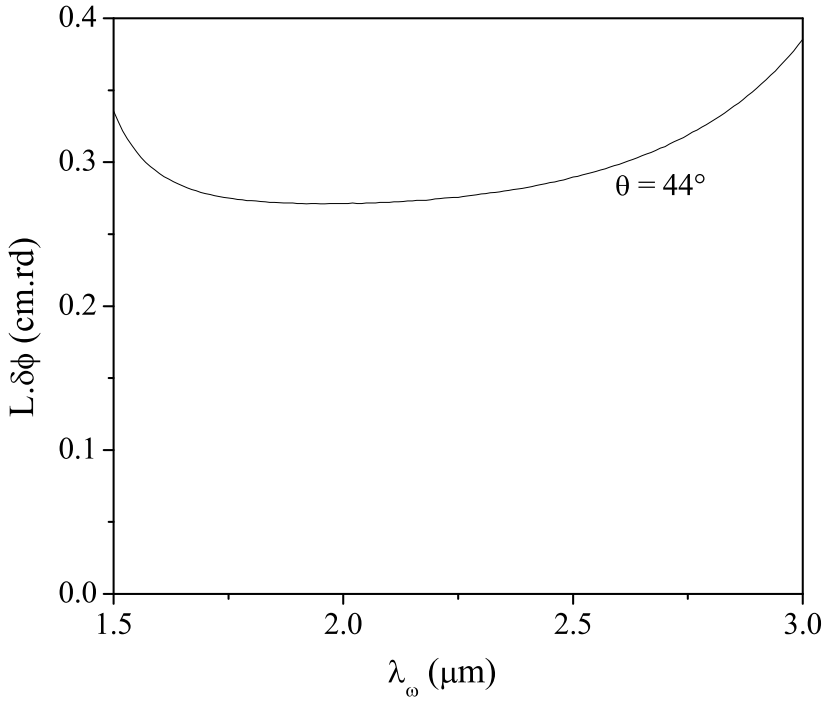

(b)

Figure 3.20: Angular acceptances of type I SHG in 5%MgO:PPLN crystal with $\Lambda = 32.2\,\mu$m. (a) θ acceptance calculated as a function of the fundamental wavelength corresponding to the AQPM curves of Fig. 3.15(a); (b) ϕ acceptance calculated as a function of the fundamental wavelength at a given θ angle. L is the length of the crystal.

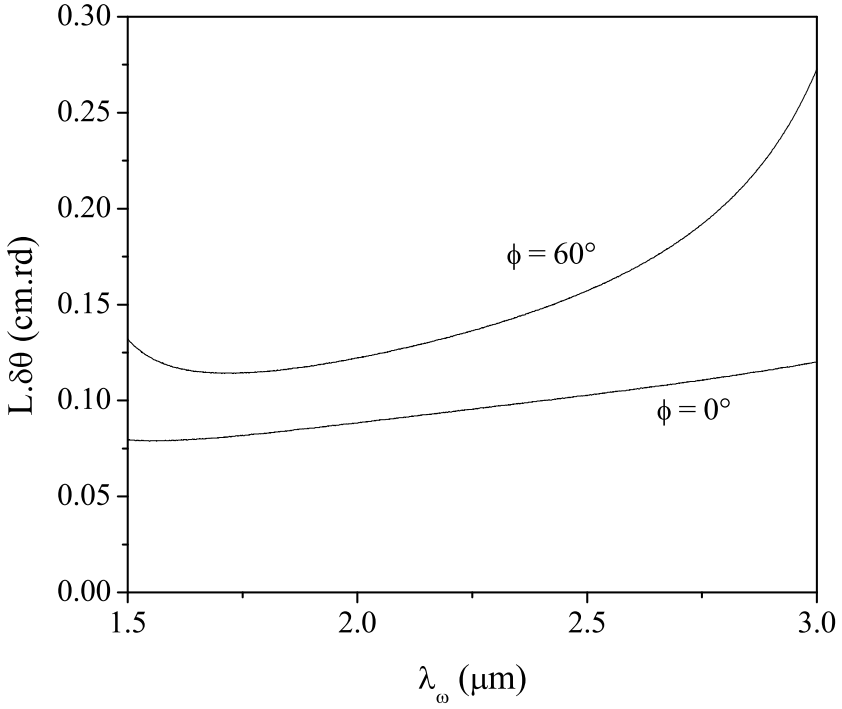

(a)

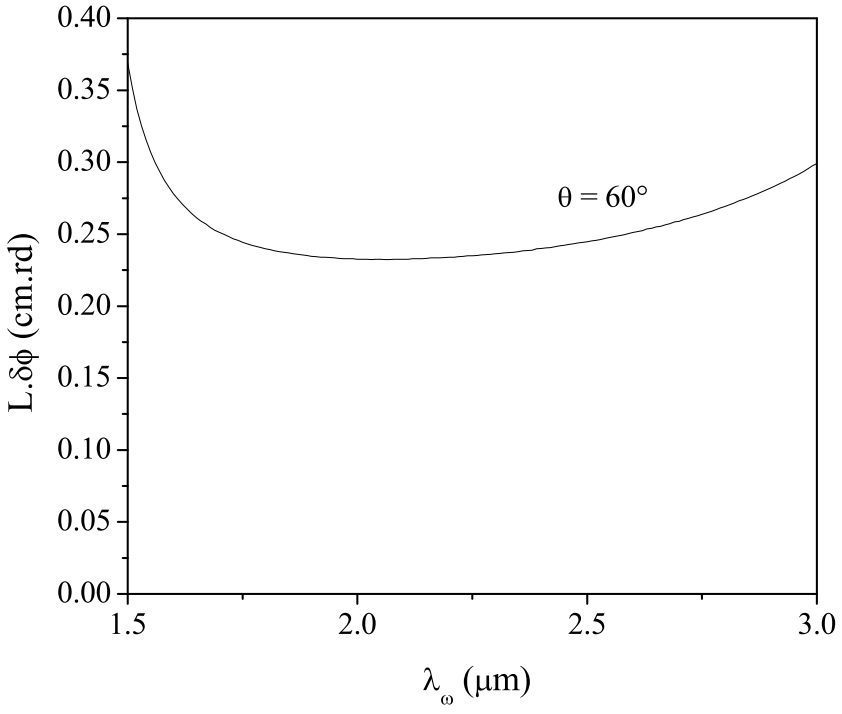

(b)

Figure 3.21: Angular acceptances of type II SHG in 5%MgO:PPLN crystal with $\Lambda = 32.2\,\mu$m. (a) θ acceptance calculated as a function of the fundamental wavelength corresponding to the AQPM curves of Fig. 3.16(a).; (b) ϕ acceptance calculated as a function of the fundamental wavelength at a given θ angle. L is the length of the crystal.

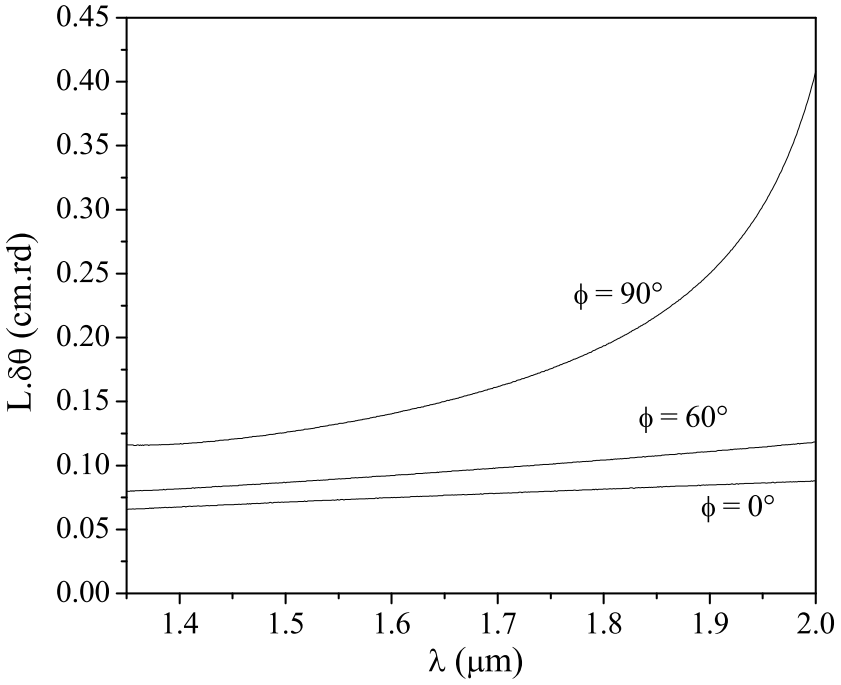

(a)

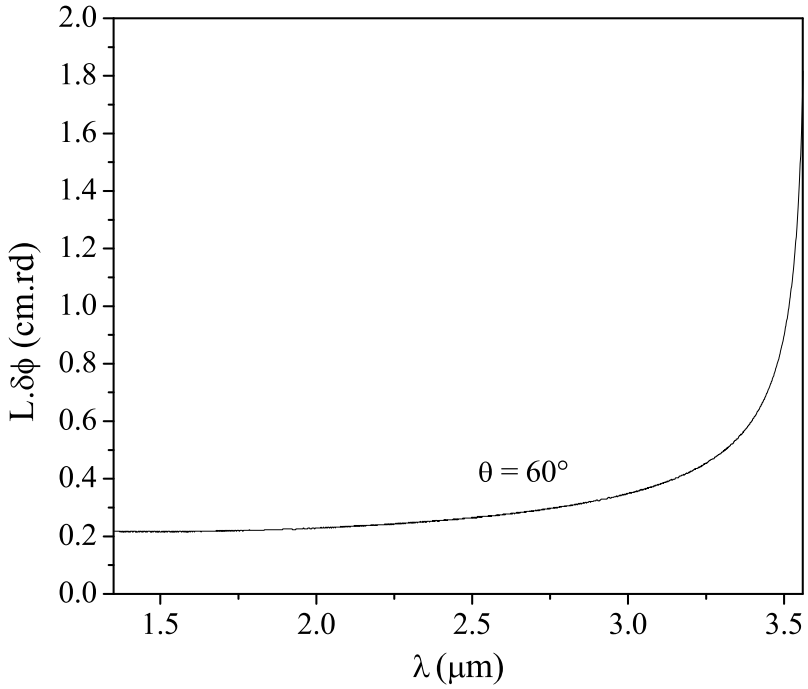

(b)

Figure 3.22: Angular acceptances of type I DFG in 5%MgO:PPLN crystal with $\Lambda = 32.2\,\mu$m. (a) θ acceptance calculated as a function of the fundamental wavelength corresponding to the tuning curves of Fig. 3.17; (b) ϕ acceptance calculated as a function of the fundamental wavelength at a given θ angle. L is the length of the crystal.

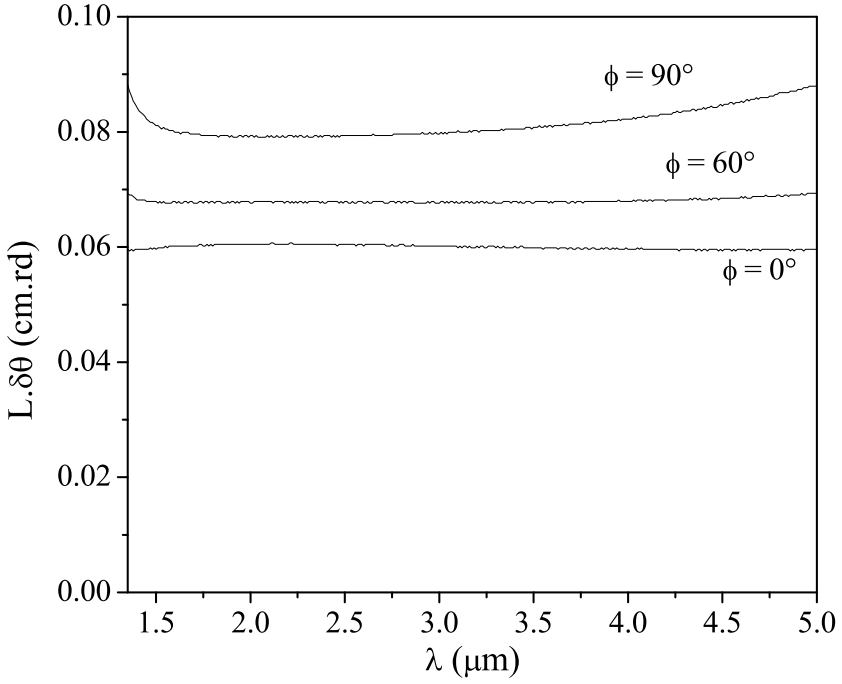

(a)

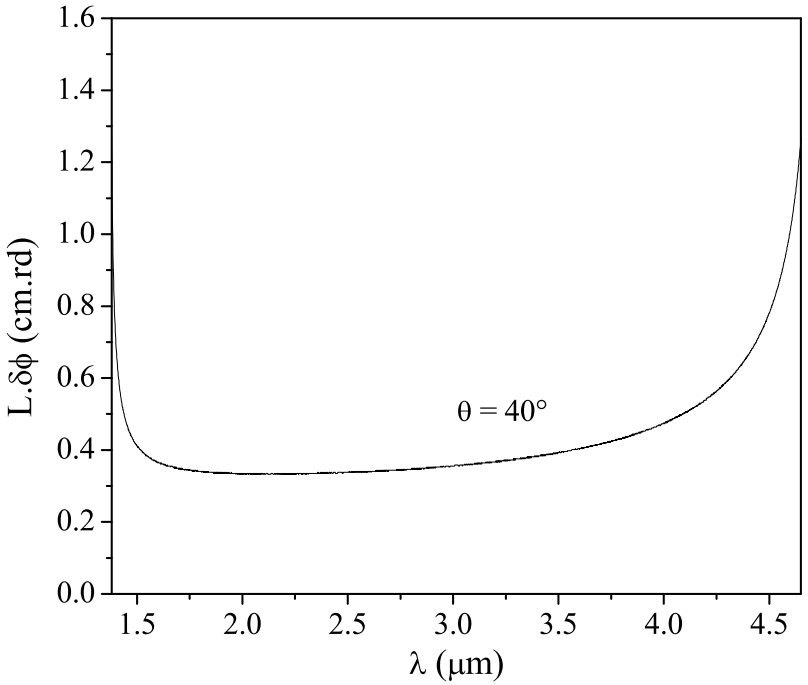

(b)

Figure 3.23: Angular acceptances of type II DFG in 5%MgO:PPLN crystal with $\Lambda = 32.2\,\mu$m. (a) θ acceptance calculated as a function of the fundamental wavelength corresponding to the tuning curves of Fig. 3.17; (b) ϕ acceptance calculated as a function of the fundamental wavelength at a given θ angle. L is the length of the crystal.

3.5 Effective coefficient

Even if momentum conservation can be theoritically satisfied for the eight possible combinations of polarization, it was necessary to ensure that the reversal of the crystal structure in 5%MgO:PPLN gives rise to a reversal of the sign of all the second order electric susceptibility tensor coefficients. The poling causes a 180° rotation of the crystal structure around the x-axis, as shown in Fig. 3.24.

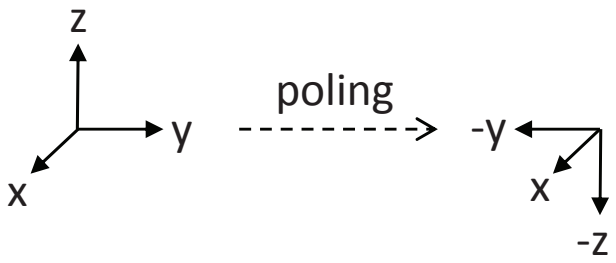

Figure 3.24: Reversal of y-axis and z-axis of 5%MgO:PPLN due to the rotation of the crystal structure around the x-axis.

The sign of a nonlinear coefficient is changed only if it exhibits an odd number of x, y or z Cartesian indices. According to this consideration, it appears that the five independent nonlinear coefficients of 5%MgO:PPLN, *i.e.* $\chi_{xxy} = \chi_{xyx} = \chi_{yxx} = -\chi_{yyy}$, $\chi_{xxz} = \chi_{yyz}$, $\chi_{xzx} = \chi_{yzy}$, $\chi_{zxx} = \chi_{zyy}$, χ_{zzz} [5], change their sign as the crystal structure is reversed. In table 3.2 are given the expressions of the effective coefficients of the eight possible configurations of polarization using Eq. 1.20 multiplied by the factor $2/\pi$ specific to AQPM [8, 34], and where the χ_{ijk} coefficients are replaced by the standard coefficients d_{ijk} defined by $d_{ijk} = \chi_{ijk}/2$ [5].

$$\begin{cases} d_{yyy} = -d_{xxy} = -d_{xyx} = -d_{yxx} = 2.6\,\text{pm/V} \\ d_{xxz} = d_{yyz} = 3.8\,\text{pm/V} \\ d_{xzx} = d_{yzy} = 3.8\,\text{pm/V} \\ d_{zxx} = d_{zyy} = 3.8\,\text{pm/V} \\ d_{zzz} = 21.6\,\text{pm/V} \end{cases} \tag{3.10}$$

Figures 3.25 and 3.26 show the variation of the effective coefficient as a function of the SHG and DFG AQPM directions calculated from the expressions of table 3.2, the refined

Type $(\omega_3\,\omega_1\,\omega_2)$	Effective coefficient d_{eff}
I (e o o)	$2\pi^{-1}\big[d_{yyy}\cos(\theta+\rho_3)\sin(\phi)\big(1-4\cos^2(\phi)\big)+d_{zxx}\sin(\theta+\rho_3)\big]$
II (e e o)	$2\pi^{-1}\big[d_{yyy}\cos(\theta+\rho_3)\cos(\theta+\rho_1)\cos(\phi)\big(4\sin^2(\phi)-1\big)\big]$
III (e o e)	$2\pi^{-1}\big[d_{yyy}\cos(\theta+\rho_3)\cos(\theta+\rho_2)\cos(\phi)\big(4\sin^2(\phi)-1\big)\big]$
IV (e e e)	$2\pi^{-1}\big[-d_{yyy}\cos(\theta+\rho_3)\cos(\theta+\rho_1)\cos(\theta+\rho_2)\sin(\phi)\big(1-4\cos^2(\phi)\big)$ $+d_{xzx}\cos(\theta+\rho_3)\sin(\theta+\rho_1)\cos(\theta+\rho_2)+d_{xxz}\cos(\theta+\rho_3)\cos(\theta+\rho_1)\sin(\theta+\rho_2)$ $+d_{zxx}\sin(\theta+\rho_3)\sin(\theta+\rho_1)\cos(\theta+\rho_2)+d_{zzz}\sin(\theta+\rho_3)\sin(\theta+\rho_1)\sin(\theta+\rho_2)\big]$
V (o o o)	$2\pi^{-1}\big[d_{yyy}\cos(\phi)\big(1-4\sin^2(\phi)\big)\big]$
VI (o e o)	$2\pi^{-1}\big[d_{yyy}\cos(\theta+\rho_1)\sin(\phi)\big(1-4\cos^2(\phi)\big)+d_{xzx}\sin(\theta+\rho_1)\big]$
VII (o o e)	$2\pi^{-1}\big[d_{yyy}\cos(\theta+\rho_2)\sin(\phi)\big(1-4\cos^2(\phi)\big)+d_{xxz}\sin(\theta+\rho_2)\big]$
VIII (o e e)	$2\pi^{-1}\big[d_{yyy}\cos(\theta+\rho_1)\cos(\theta+\rho_2)\cos(\phi)\big(4\sin^2(\phi)-1\big)\big]$

Table 3.2: Effective coefficients associated to the eight types of AQPM in 5%MgO:PPLN [34].$(\omega_1,\omega_2,\omega_3)$ are the circular frequencies of the interacting waves and (ρ_1,ρ_2,ρ_3) are the corresponding double refraction angles. (o) and (e) refer to the ordinary and extraordinary polarizations. (θ,ϕ) are the angles of spherical coordinates of the direction of propagation. The d_{ijk} coefficients are the second order electric susceptibility tensor coefficients.

Sellmeier equations given in table 3.1, and the values of the d_{ijk} coefficients of Eq. 3.10 [8]. We see that the effective coefficient strongly depends on the ϕ angle, and that it vanishes in some cases. For example, Fig. 3.25 shows that the effective coefficient is zero at $\phi = 30°$ in the case of type I SHG. Furthermore, the values of d^2_{eff} of type I and II SHG or DFG are low in comparison with the usual type IV for which $d^2_{\text{eff}} > 400\,\text{pm}^2/\text{V}^2$ along the x direction.

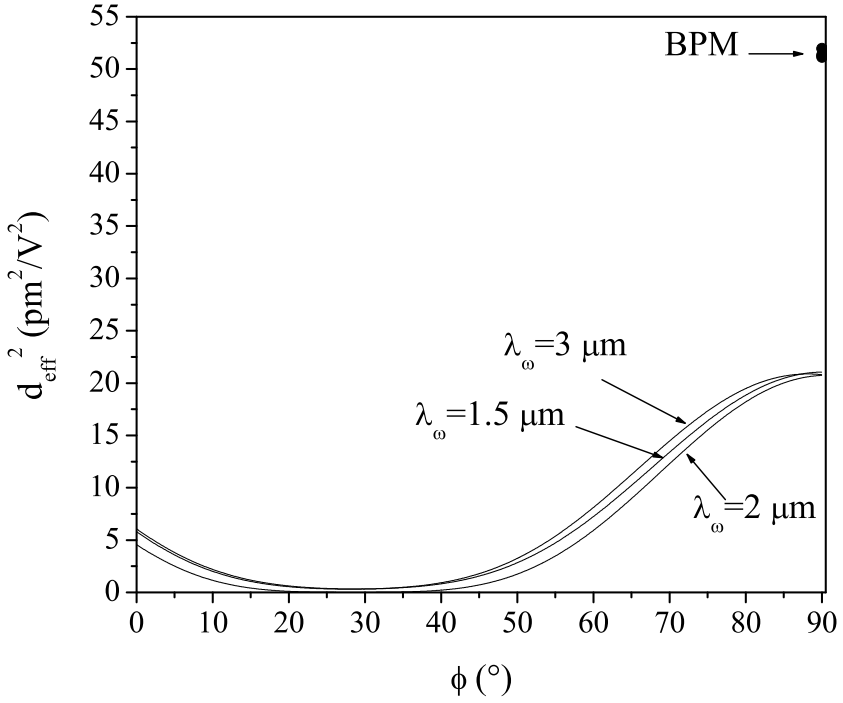

(a)

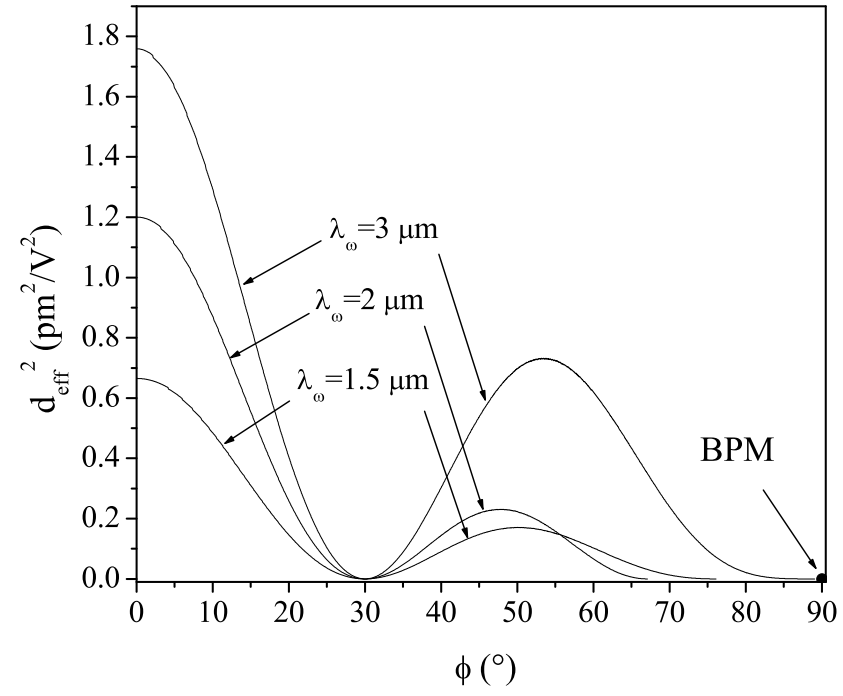

(b)

Figure 3.25: Square of the effective coefficient of type I SHG (a) and type II SHG (b) for different fundamental wavelengths λ_ω as a function of the spherical ϕ angles of the AQPM directions in 5%MgO:PPLN crystal with $\Lambda = 32.2\,\mu$m. The dot at $\phi = 90°$ corresponds to BPM.

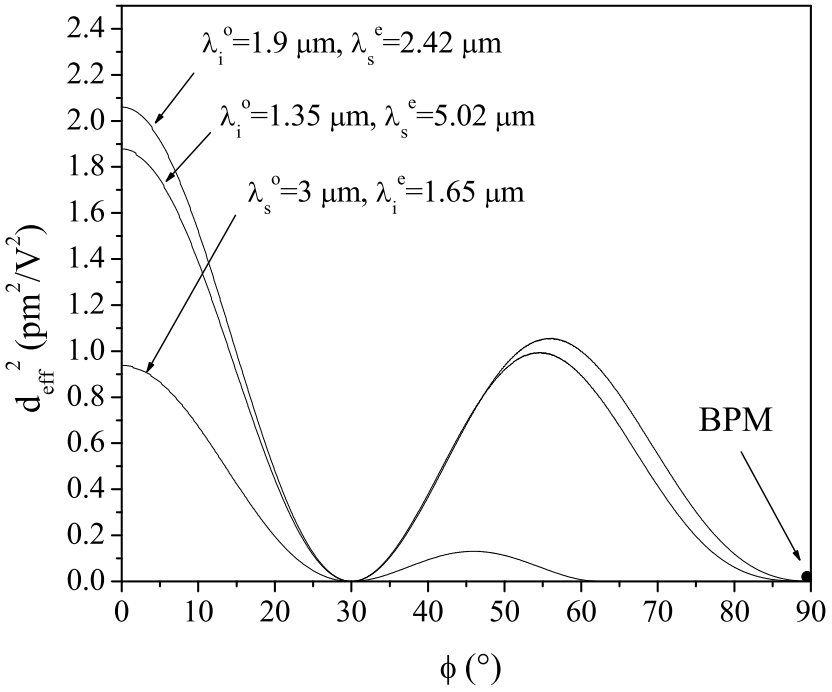

(a)

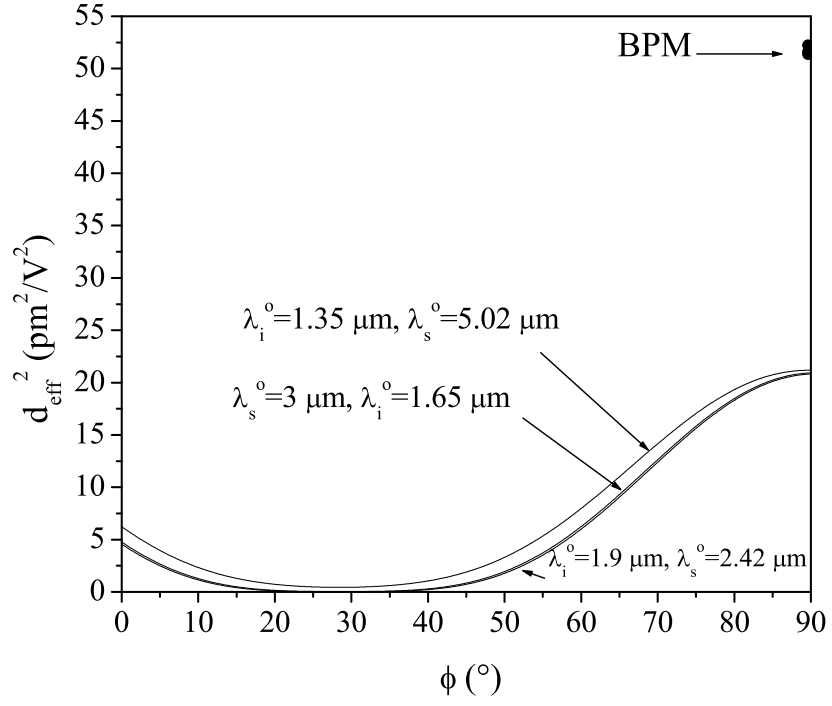

(b)

Figure 3.26: Square of the effective coefficient of type I DFG (a) and type II DFG (b) for different fundamental wavelengths λ_ω as a function of the spherical ϕ angles of the AQPM directions in 5%MgO:PPLN crystal with $\Lambda = 32.2\,\mu$m. The dot at $\phi = 90°$ corresponds to BPM.

3.6 Trade-off between conversion efficiency and acceptance bandwidth

Laser pulses that are tunable in wavelength in the femtosecond regime would be of particular interest for many applications like time-resolved spectroscopy for example. The availability of high energy femtosecond lasers allows to consider parametric interaction in this time domain. However, frequency conversion by keeping an ultrashort pulse is a real challenge. Indeed, achieving phase-matching for all the frequencies requires a large spectral acceptance since ultrashort pulses have a wide spectral bandwidth. Actually, for bandwidth-limited Gaussian-shaped pulses, the time-bandwidth product is [35]:

$$\delta\nu \cdot \delta\tau \approx 0.44 \tag{3.11}$$

Given the pulse duration $\delta\tau$, the minimum bandwidth $\delta\nu$ that is necessary for maintaining this duration can be calculated thanks to Eq. 3.11. For example, pulses of 1 ns, 1 ps and 1 fs have respectively bandwidths of 440 MHz, 440 GHz and $440 \cdot 10^3$ GHz. If the pulse has a wavelength around 1 μm, it correponds respectively to bandwidths of about 1.510^{-3} nm, 1.5 nm and 1500 nm.
The easiest way to increase the spectral bandwidth of a nonlinear crystal is to reduce its length since the spectral acceptance is inversely proportional to its length [36]. However, reducing the length of the nonlinear crystal causes a decrease of the efficiency which is inversely proportional to the square of the length (according to Eq. 1.22). In conclusion, while dealing with ultra-short pulses, there is a trade-off between conversion efficiency and spectral bandwidth.

Section 3.4.1 showed that AQPM exhibits interesting properties in term of spectral bandwidth. Now, these properties have to be confronted to the effective coefficients given in section 3.5.
From $\nu = c/\lambda$, we can deduce the link between the spectral acceptance $L\delta\lambda$ [cm $\cdot$ μm] and the spectral bandwidth $\delta\nu$ [Hz]:

$$\delta\nu = \frac{c}{L\,\lambda^2}\,(L\delta\lambda) \tag{3.12}$$

Eqs. 3.11 and 3.12 allow to calculate the maximum length of crystal $L = L_{\max}$ that can be used without lengthening the pulse duration:

$$L_{\max} = \frac{c\,\delta\tau}{0.44\,\lambda^2}\,(L\delta\lambda) \tag{3.13}$$

According to Eqs. 1.22 and 3.13, and assuming a group velocity matching, we have:

$$\mathcal{P}^{3\omega} \propto {d_{\text{eff}}}^2 \left(L_{\max}\delta\lambda\right)^2 \tag{3.14}$$

Consequently, the relevant quantity for the present purpose is the product $(L_{\max}\delta\lambda)^2 {d_{\text{eff}}}^2$. Figure 3.27 gives the example of the calculation of $(L_{\max}\delta\lambda)^2 {d_{\text{eff}}}^2$ in the case of type I SHG corresponding to the curves of Figs. 3.15(a) and 3.15(b).

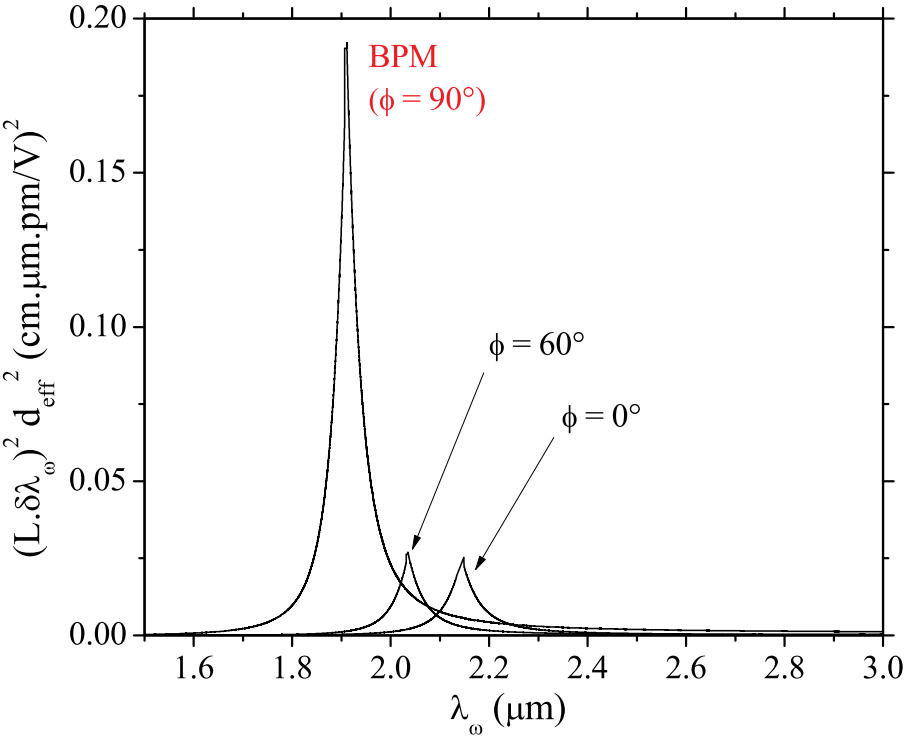

Figure 3.27: Product $[(L\delta\lambda)d_{\text{eff}}]^2$ as a function of different ϕ angles for type I SHG. $d_{\text{eff}}(\theta,\phi)$ is calculated from Table 3.2; θ varies according to the tuning curves given in Fig. 3.15(a).

It appears that it is more interesting to perform type I SHG in the yz plane, which corresponds to BPM when the fundamental wavelength λ_ω is below $2.02\,\mu$m. But for $2.02\,\mu\text{m} < \lambda_\omega < 2.23\,\mu\text{m}$, it is preferable to use AQPM by taking advantage of the maximal spectral acceptance continuum ranging below $\phi = 90°$.

3.7 Conclusion

The experiments done in a 5%MgO:PPLN sphere with a grating period $\Lambda = 32.2\,\mu$m allowed first to validate the AQPM theory, with in particular the demonstration of a continuum of directions allowing a giant spectral acceptance. They also allowed us to refine the Sellmeier equations of this crystal, which is of crucial importance as well for fixed-wavelength applications as for tunable devices. Furthermore, we have shown that the usual combination of polarization, called type IV in this work, that solicits the stronger element of the second-order electric susceptibility, is not necessary the best one in term of spectral acceptance. There is actually a complicated compromise between efficiency and spectral acceptances.
The main limitation of AQPM is that it requires thick periodically-poled media in order to have a sufficient interaction length in any direction. The problem of the limited thickness of the samples is due to the impossibility to overcome the cohercitif field with electric fields on more than few millimeters. The resolution of this problem could come from a direct growth from a periodically-poled seed that would conserve the poling during the growth. This possibility has been demonstrated recently on PPKTP in the group of Néel Institute.

As a perspective, AQPM may also be applied to PPKTP [27], PPLT [28] and PPKN [37] since they exhibit nonlinear coefficients with the same order of magnitude than those of PPLN.

Chapter 4

Optical properties of $CdSiP_2$

4.1 State of the art

4.1.1 Introduction

Nowadays, solid-state lasers allow to cover a wide spectral band from ultraviolet to infrared light, partly thanks to parametric devices based on frequency conversion in nonlinear crystals. However there are not yet satisfying solutions in order to produce high energetic pulses in the range of wavelengths $8-12\,\mu$m. This interval corresponds to a transparency band of the atmosphere, called third band (band III), which is interesting for various applications like detection of atmospheric pollutants or nerve gases, infrared spectroscopy, communication between satellites, biomedicine, laser surgery, teledetection, and counter-measure.

With no claim to be exhaustive, this state of the art presents the main characteritics of the existing sources that already exist in this interval of wavelengths. A first part is dedicated to fixed-wavelength lasers that emit in the 8-12 μm band, in particular CO_2 lasers, lead salt laser diodes and quantum cascade lasers. A second part is focused on optical parametric sources that usually consist on the association of a fixed-wavelength laser and a nonlinear crystal, such sources enabling a broad spectral tunability. The generally-used nonlinear crystals and the promising ones are then described into details in order to understand the choice that was done to work on $CdSiP_2$.

4.1.2 Lasers

Carbon dioxide lasers (CO_2 lasers) emit around 10 μm. They can work either in continuous wave (CW) or in nanosecond regime at very high power, until several kilowatts. They are widely used for metal cutting, surgery and LIDAR applications. These lasers can also serve as pump source for parametric processes. In the literature, a lot of nonlinear materials for the infrared region are characterized by second-harmonic generation (SHG) measurements of a CO_2 laser [38, 39]. In theses examples the power of the CO_2 laser varies from 10 watts CW to 10 kilowatts of peak power in nanosecond regime.

Lead salt laser diodes are made of PbTe, PbSe or PbS. The photons come from a transition of electrons from the conduction band to the valence band. Since the energy gap between these two bands is low in such materials, *i.e.* between 0.1 eV and 0.3 eV, the associated emission of light occurs in the infrared. The main problem of these lasers is the necessity to work at cryogenic temperatures in order to be able to work in CW regime, in particular because of the non radiative Auger recombination [40]. Furthermore, the output power does not exceed the milliwatt level at wavelenghs ranging between 8 μm and 12 μm. As a consequence, the lead salt laser diodes are mainly used for spectroscopy.

Since they were invented in 1994, quantum cascade lasers (QCL) have shown better performance than lead salt lasers. QCL are semiconductor lasers that emit in the infrared. The emission is realized by electronic intersubband transitions in heterostructures. They have several advantages. First, the energy levels do not depend on the gap of the semiconductor itself but depend on the thickness of the layers leading to an easy way to tune the QCL wavelength. Then it is not the recombination of an electron with a hole that generate a photon as in a classical diode. Actually in a QCL, a single electron allows to generate about 30 photons by a phenomenon of cascade. Thus the quantum efficiency is greater than 100%. QCL show output powers that are greater than lead salt laser diodes. Beyond 8 μm, an output power of 350 mW has been demonstrated at room temperature [41]. Another advantage of QCL is that they can emit until terahertz radiation. However QCL have some drawbacks: the major part of the electric energy is converted into heat, so that it is difficult for them to emit in CW regime at room temperature [42]. Output powers are low compared with solid state lasers, in the order of ten milliwatts (15 mW by Hamamatsu [43]). Finally these lasers are not stricly speaking tunable because one needs to change the chemical composition of the heterostructure in order to change the wavelength.

As a conclusion, lead salt laser diodes and QCL are tunable sources in the infrared. They emit between 8 μm and 12 μm, but there tunability is limited and they do not allow high peak powers.

4.1.3 Optical parametric sources

4.1.3.1 General considerations

Optical parametric oscillators (OPO) are coherent light sources that present the advantage to be easily and widely tunable in wavelength, and they are commonly used to generate waves at wavelengths for which no laser exists. An OPO is based on a nonlinear crystal placed into an optical cavity allowing the resonance at the signal wavelength (λ_s) or at the idler wavelength (λ_i), these waves being generated by a fixed-wavelength laser called the pump wavelength (λ_p) [44, 45]. Oscillation occurs when the pump power reaches a threshold level, as in a laser. There are different ways of realizing the tunability when λ_p is fixed. In the case of BPM, the rotation of the crystal with respect to the pump beam allows a variation of λ_s and λ_p by successively addressing the continuum of phase-matching directions in the plane perpendicular to the rotation axis. In the case of quasi-phase-matching, the methods consist in translating a multi-grating sample or translating a fan-shaped grating or by rotating a cylinder having a single grating as shown respectively in Figs. 3.1(b), 3.1(a), and 3.1(c) of chapter 3. The tunability can also be obtained by varying λ_p or the temperature of the crystal.

The main difficulty to overcome in order to realize a phase-matched or quasi-phase-matched OPO is to find a nonlinear crystal having low absorption at λ_p and $\lambda_p/2$ in order to resist to one-photon and two-photons pump absorption respectively. Furthermore, the optical damage threshold has to be high enough to support high peak-power energies. The dimension of the crystal is also an important criterium for this purpose because the fluence can be reduced by increasing the beam diameter. Moreover, for an industrial implementation, the disponibility, the cost and the non toxicity of the crystal also become important parameters.

In this context, it is also important to have a nonlinear crystal where BPM or QPM enable the pumping by a standard and reliable laser like Nd:YAG emitting at 1.064 μm, fiber lasers doped with Erbium that generate at 1.55 μm, or the eye-safe OPOs based on KTP that emit at 1.570 μm.

The most interesting nonlinear crystals to work within the $8-12\,\mu$m region are semiconductor materials that belong to two families: chalcopyrites (II-IV-V_2 and I-III-VI_2) and III-V or II-VI semiconductors. This section is aimed at giving a brief description of the crystals that are commonly used in commercial sources ($AgGaS_2$, $AgGaSe_2$, $ZnGeP_2$, CdSe), and of promising crystals (GaN, ZnSe, PPGaN, OPGaAs, $CdSiP_2$). A more exhaustive study of nonlinear crystals for the infrared can be found in reference [46].

4.1.3.2 $AgGaS_2$ and $AgGaSe_2$

$AgGaS_2$ (AGS) and $AgGaSe_2$ (AGSe) are two interesting compounds because they can be pumped at $1.064\,\mu$m, they are transparent beyond $12\,\mu$m, and their nonlinear coefficient is of about 35 pm/V [47]. They have the drawback to have a low optical damage threshold: $1.4\,MW/cm^2$ for $AgGaS_2$ and $7\,MW/cm^2$ for $AgGaSe_2$ at $2.097\,\mu$m, at a pulse duration of 180 ns [48]. At $1.064\,\mu$m, a damage threshold of $11\,MW/cm^2$ was measured [49]. Because of the the low value of this optical damage threshold, these materials cannot be used at high power. Nevertheless they are commonly used in industrial tunable sources from $2\,\mu$m to $12\,\mu$m. As an example, the Lithuanian company *Light Conversion* offers for sale sources based on $AgGaS_2$ that deliver between $10\,\mu$J and $100\,\mu$J over 15 ps from a difference-frequency generation between a wave at $1.064\,\mu$m and a tunable wave coming from an optical parametric generator based on a LBO crystal.

4.1.3.3 $ZnGeP_2$

$ZnGeP_2$ has a high nonlinear coefficient of 75 pm/V [50] and a high optical damage threshold of $35\,MW/cm^2$ at $2.93\,\mu$m over 100 ns. Its principal drawback is that it cannot be pumped at less than $2\,\mu$m because of a high absorption. Thus OPOs have been realized using as a pump either Erbium lasers at $2.93\,\mu$m [50] or KTP-based OPOs [51] or PPLN-based OPOs [52]. The devices are tunable between $3.8\,\mu$m and $12.4\,\mu$m, and the quantum efficiency reaches 35 % [50].

4.1.3.4 Cadmium selenide

Among all the birefringent crystals, cadmium selenide (CdSe) has been the most studied in order to realize frequency conversion in the 8-12 μm range. It holds several advantages: its growth is well controlled, it is transparent from $0.75\,\mu$m to $24\,\mu$m, its nonlinear coefficient is comfortable, *i.e.* 18 pm/V, and its optical damage threshold is high: $40\,MW/cm^2$ for 20 ns

pulses at 2 μm. In term of tunability, it is possible to cover two disonnected spectral bands: from 2 μm to 5.5 μm and from 7.5 μm until the infrared cutoff. Even if many OPOs have been demonstrated, with a generated power reaching 1 W at around 8 μm [53], CdSe has the huge drawback of not satisfying the phase-matching condition if it is pumped at less than 1.8 μm because its birefringency is too low in that spectral range. It is thus impossible to pump CdSe with a common source at 1.064 μm or 1.570 μm.

4.1.3.5 Gallium nitride and periodically-poled gallium nitride

Gallium nitride (GaN) seems also interesting because it is birefingent and has a wide transparency window. Its large bandgap allows him to be transparent until 0.36 μm on the UV side. However it has few drawbacks. In particular its growth is not well-controlled: it is tough to obtain thicknesses that excess the millimeter. In addition, its birefringency is low and it absorbs above 10 μm. The refractive indices of GaN have only been measured on thin films of few microns and not beyond 5 μm [54, 55]. Moreover the Sellmeier equations can differ a lot from a sample to another according to the growth method or the doping concentration [56]. We found no reference dealing with the measurement of the transparency window of bulk GaN. The nonlinear coefficient of GaN is equal to 5.3 pm/V when measured on thin films by a Maker fringes experiment [5]. The principal asset of GaN is to be prone to intensive research for optoelectronic use [57]. No parametric device has yet been realized with bulk GaN.

Periodically-poled gallium nitride (PP-GaN) is grown by molecular beam epitaxy (MBE). As a consequence, the final thickness is limited to few microns. Experiments of second-harmonic generation have been performed at around 1.66 μm [58]. In these experiments, 9 μW of second-harmonic have been generated from 100 W at 1658.6 nm.

4.1.3.6 Zinc selenide

Zinc selenide (ZnSe) has an excellent transparency, from 0.5 to 20 μm [59]. It is a widely-used material of the infrared but it is optically isotropic. As a result quasi-phase-matching must be used. ZnSe has the assets to possess a high nonlinear susceptibility of 75 pm/V [39] and a high optical damage threshold, between 2 and 5 J/cm^2 [59]. In order to realize the periodical sign inversion of the nonlinear coefficient, it is possible to stick polished slices by the diffusion bonding technique, each slice being rotated of 180° with respect to the previous one. The problem of this method is technological difficulty of the sticking process

leading to losses and the interfaces. Quasi-phase-matching by Fresnel reflections has been tested recently to overcome this problem in ZnSe:Cr [60].

4.1.3.7 Orientation-patterned gallium arsenide

Gallium arsenide (GaAs) is optically isotropic. However it holds interesting characteristics for parametric optics in the infrared because it is transparent from 0.9 up to 17 μm and has a very high second order nonlinear coefficient, in the order of 94 pm/V [61]. Moreover the growth of GaAs is well domesticated, in particular thanks to its use in optoelectronics. Huge efforts have been done in order to periodically reverse the sigh of the nonlinear coefficient leading to the so-called orientation-patterned gallium arsenide (OP-GaAs). Indeed since GaAs is not ferroelectric, it is not possible to reverse the polarity by applying an electric fiels. The reversal of the structure can be realized either by diffusion bonding as for ZnSe, with the same drawbacks, or by MBE followed by hybrid vapor phase epitaxy (HVPE). The drawback of this latest technique is that the thickness remains low, in the order of 0.5 mm. An OPO tunable from 2.28 to 9.14 μm has been demonstrated [62] as well as an OPG that generates a continuum from 4.5 to 10.7 μm [63]. Quantum efficiencies reach 54% for output energies of 3 μJ [62]. An OPO based on OP-GaAs has been newly demonstrated with a record output power of 0.6 W from 2.4 W of pump power at 2 μm [64].

4.1.3.8 $CdSiP_2$

$CdSiP_2$ is a promising material which has been recently proposed for infrared frequency conversion [65]. Its strong point is the bandgap energy, of about 2.2 eV, which makes it transparent until 0.56 μm. On the infrared side, it is transparent up to 10 μm. $CdSiP_2$ is a negative uniaxial crystal with the same symmetry as KDP. Its nonlinear coefficient reaches 53 pm/V. Thanks to its high birefringency, of about 0.045, an OPO based on $CdSiP_2$ pumped at 1.550 μm could be tunable between 2 μm and 10 μm. Frequency doubling of a CO_2 laser has been realized in $CdSiP_2$ with an efficiency higher than 20% [65]. Recently an OPO based on $CdSiP_2$ was demonstrated, generating 470 μJ energy over 10 ns at about 6.2 μm [66]. Furthermore the thermal conductivity of $CdSiP_2$ is 13.6 W/mK whereas it is only 1 W/mK for AGS. Thus we can expect a higher optical damage threshold.

4.1.4 Conclusion

Table 4.1 shows a comparison between CO_2 lasers, quantum cascade lasers and parametric sources for wavelengths beyond $8\,\mu$m [41]. While CO_2 lasers are well-suited for cutting and welding applications thanks to their very high powers, quantum cascade lasers have the advantage to be compact but are limited in spectral tunability and in power levels. OPOs are the ideal sources when a wide tunability and a high power are required. Nowadays, for wavelengths higher than $8\,\mu$m, commercial OPOs are based on ZGP and AGS. They don't give a great satisfaction because their optical damage threshold is weak, which limits the output power. Thus it is necessary to pursue the research on new promising materials like $CdSiP_2$, which is described in the following sections.

Type of source	CO_2 laser	Quantum cascade lasers	Parametric sources
Regime	CW or quasi-CW	CW or quasi-CW	depending on the pump
Tunability	$9.15 - 9.83\,\mu$m $10.09 - 10.93\,\mu$m	$8.4 - 10.4\,\mu$m [67]	$8 - 12\,\mu$m
Average power	400 W	~ 500 mW	~ 1 W

Table 4.1: Comparison between the performances of various laser sources between $8\,\mu$m and $12\,\mu$m.

4.2 General characteristics of $CdSiP_2$

$CdSiP_2$ is a II-IV-V_2 chalcopyrite semiconductor belonging to the space group $\bar{4}2m$. Its band gap of 2.2 eV makes it transparent in the visible side until $0.56\,\mu$m [23]. It is a negative uniaxial crystal with a birefringence $n_e - n_o \approx -0.05$, which is large enough for realizing difference-frequency generation implying a beam at $1.064\,\mu$m or at $1.5\,\mu$m. The growth of $CdSiP_2$ was first realized in the 1970s using a molten tin flux, but the size of the grown crystals was not sufficient to measure its linear and nonlinear optical properties [68]. Recently, successful growth of large single crystals of $CdSiP_2$ was achieved using the horizontal gradient freeze technique (HGF) in the team of Peter Schunemann at BAE Systems [69]. Infrared absorption spectra have shown a good transparency in the $3 - 5\,\mu$m region, and intrinsic multi-phonon peaks at $7.1\,\mu$m and $7.65\,\mu$m. Furthermore, the nonlinear coefficient of $CdSiP_2$ was measured using SHG at $4.6\,\mu$m by comparison with a ZGP crystal of the same thickness. These measurements showed a slight superiority of $CdSiP_2$ over ZGP: $d_{36}(\text{CSP}) = 84.5$ pm/V while $d_{36}(\text{ZGP}) = 78.9$ pm/V [23]. The result is surprising

since the bandgap of $CdSiP_2$ is higher than the one of ZGP, the nonlinear coefficient usually decreasing when the bandgap increases. The principal refractive indices n_o and n_e of $CdSiP_2$ were measured using the minimum deviation technique in a 30° prism over the wavelength range $0.66 - 5.0\,\mu$m. They led to the following Sellmeier equations [23]:

$$\begin{cases} n_o^2 = 3.0811 + \dfrac{6.2791\,\lambda^2}{\lambda^2 - 0.10452} - 0.0034888\,\lambda^2 \\ \\ n_e^2 = 3.4343 + \dfrac{5.6137\,\lambda^2}{\lambda^2 - 0.11609} - 0.0034264\,\lambda^2 \end{cases} \tag{4.1}$$

These Sellmeier equations predict an angular non critical phase-matching at $6.18\,\mu$m when the crystal is pumped at $1.064\,\mu$m. This possibility was verified in 2009 with the frabrication of an OPO producing $470\,\mu$J energy at about $6.2\,\mu$m [66].

The goal of the present work is to provide a complete optical characterization of this new material in order to be able to estimate its full potentialities, especially for the generation of coherent light in the third atmospheric band.

4.3 Measurement of the transparency window of $CdSiP_2$

The absorption spectrum was measured from the visible to the far infrared thanks to two different spectrometers. The first part of the spectrum was realized using a UV-Vis-NIR *Cary* photospectrometer covering the $0.175 - 3.3\,\mu$m range. Two different detectors were used: a photomultiplier tube from 0.175 to $0.8\,\mu$m and a cooled PbS photodiode from 0.8 to $3.3\,\mu$m. The second part of the spectrum was realized with a *Bruker* FT-IR spectrometer covering the $3 - 20\,\mu$m range. The detection was done with a pyroelectric detector made of deuterated triglycine sulfate (DTGS). The two spectra were connected and the whole transparency range of $CdSiP_2$ under unpolarized light is shown in Fig. 4.1. In the visible side, the transparency rises from 5% at $0.62\,\mu$m to 40% at $0.74\,\mu$m. The band gap energy E_g can be deduced from:

$$E_g = \frac{hc}{\lambda_c} \tag{4.2}$$

where $h \approx 6.62 \times 10^{-34}\,\mathrm{J \cdot s}$ is the Planck constant, $c \approx 3 \times 10^8\,\mathrm{m/s}$ is the speed of light, and λ_c is the cut-off wavelength. From the spectrum of Fig. 4.1, λ_c ranges between $0.62\,\mu$m and $0.74\,\mu$m, which corresponds from Eq. 4.2 to 1.6 eV and 2.0 eV, close to the 2.2 eV. Since

$CdSiP_2$ absorbs at 0.532 μm, two-photon absorption will not be avoided while pumping at 1.064 μm. Note that in semiconductors, the band gap energy increases whith decreasing temperature, so that working at low temperature would lead to a decreasing of the cut-off wavelength.

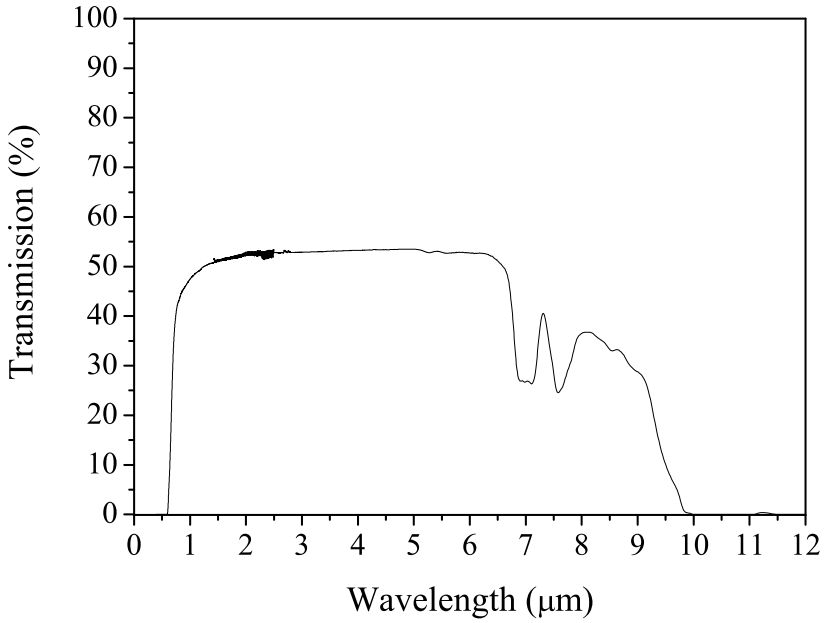

Figure 4.1: Transparency window of $CdSiP_2$

On the infrared side, the transparency decreases from 20% to 5% between 9.3 and 9.7 μm. Thus, the whole second atmospheric transparency band (3-5 μm) is covered while the third atmospheric transparency band (8-12 μm) is partly covered.

4.4 Measurement of the optical damage threshold of $CdSiP_2$

A comparative study between $AgGaS_2$ and $CdSiP_2$ have been realized on the same optical bench. The two samples were cut with the same thickness of about 1 mm, and they were polished with the same process and stuck one beneath the other on a translation stage, as shown in Fig. 4.2. The damage threshold was investigated at 1.064 μm and 1.570 μm corresponding to potential pump wavelengths. The pulse duration was 15 ps and the repetition rate 10 Hz.

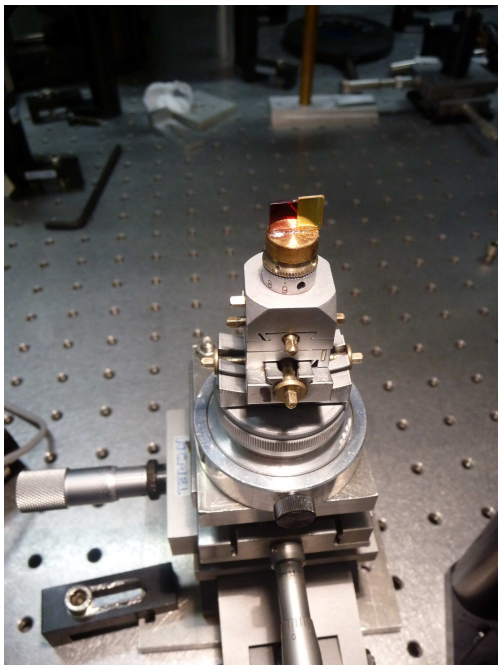

Figure 4.2: Picture of the samples of $AgGaS_2$ (right) and $CdSiP_2$ (left) stuck one beneath the other for the measurement of the optical damage threshold.

The fluence was calculated from the measurement of the pulse energy and of the section of the beam. The energy was continuously controlled thanks to the association of a rotating half-wave plate and a fixed polarizer; it was recorded with a pyroelectric detector. The measurement of the surface of the beam was carried out with a pixel-array camera. The recorded profile of the beam at $1.064\,\mu$m is shown on Fig. 4.3 where we see that the beam profile is not Gaussian. The beam profile at $1.57\,\mu$m could not be measured because of the limitation of the camera which is made of silicon. However, since these two beams come from the same OPG-OPA stage, we considered they have got the same surface in first approximation.

The surface was calculated by using the following formula which is generally used in case of non Gaussian beams:

$$S(\text{pixels}) = \frac{\sum_i p_i}{p_{\max}} \tag{4.3}$$

where p_i is the value of the energy measured on pixel i, and $p_{\max}$ is the value of the energy of the pixel of maximal energy. The sum is done on all the pixels. The surface of the beam

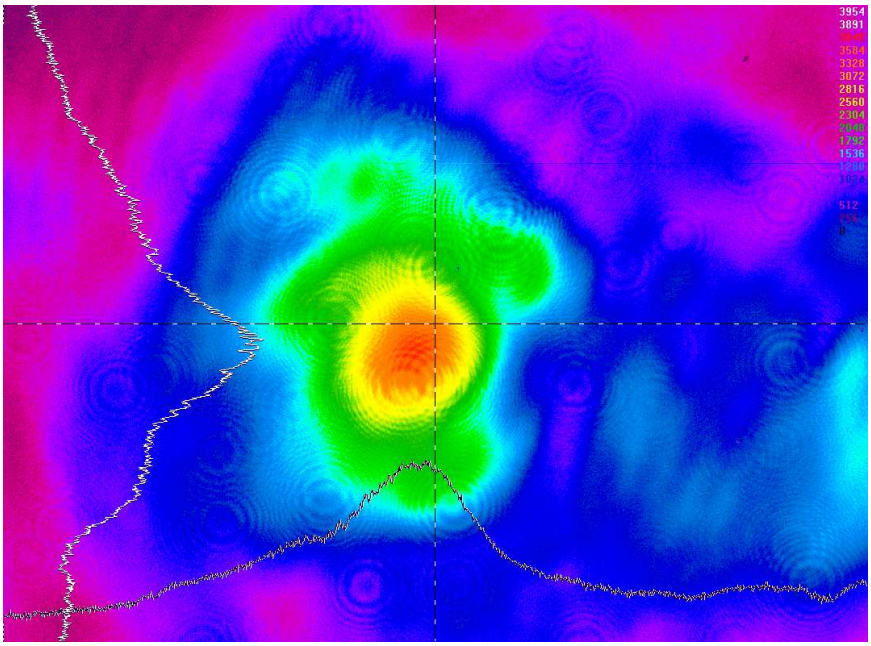

Figure 4.3: Transversal section of the laser beam at 1.064 μm recorded whith a pixel-array camera.

in cm^2 is then calculated by the knowledge of the size of one pixel:

$$S(\mathrm{cm}^2) = S(\mathrm{pixels}) \times \text{size pixel}(\mathrm{cm}^2) \tag{4.4}$$

This calculation led to $S = 0.576\,\mathrm{cm}^2$ and thus $w_0 = 1.354\,\mathrm{mm}$ from $S = \pi w_0^2$. The beam was then focused inside the crystal with a convergent lens. The surface of the beam at the focal point was calculated from the measurement of the surface before focusing and the following formula of Gaussian optics:

$$w_0' = \frac{\lambda\, f}{\pi\, w_0} \tag{4.5}$$

where λ is the wavelength, w_0 is the beam waist radius before the lens, and w_0' is the beam waist radius of the beam at the focal point. The focal length f was chosen in order to ensure that the Rayleigh length z_R, given by Eq. 2.6, was larger than the thickness e of the samples, in order to assume a quasi-parallel propagation inside the crystal. According to Eqs. 4.5 and 2.6, the condition $z_R > e$ writes:

$$f > \sqrt{\frac{\pi\, n\, w_0^2\, e}{\lambda}} \tag{4.6}$$

With our samples of thickness $e = 1\,\text{mm}$, this condition corresponds to $f > 130.3\,\text{mm}$ for $\lambda = 1.064\,\mu\text{m}$ and $f > 328.9\,\text{mm}$ for $\lambda = 1.570\,\mu\text{m}$. We chose $f = 500\,\text{mm}$ for the two wavelengths.

The method of evaluation of the optical damage threshold was a "10 on 1" method consisting in shooting 10 times at one point of the sample before looking if any damage occured. The energy of the incident beam is gradually increased until damage is observed. Damage impacts on the crystals were eyely observed under a microscope.

Damage threshold measurements are shown in Fig. 4.4 where we see that $CdSiP_2$ is inferior than $AgGaS_2$, especially at $1.064\,\mu\text{m}$. It can be due to two-photon absorption in $CdSiP_2$ since it absorbs at $0.532\,\mu\text{m}$, contrary to AGS which is transparent until $0.46\,\mu\text{m}$. But we see that $CdSiP_2$ is also worse than AGS at $\lambda = 1.570\,\mu\text{m}$, and that even if it should not suffer from two-photon absorption at this wavelength.

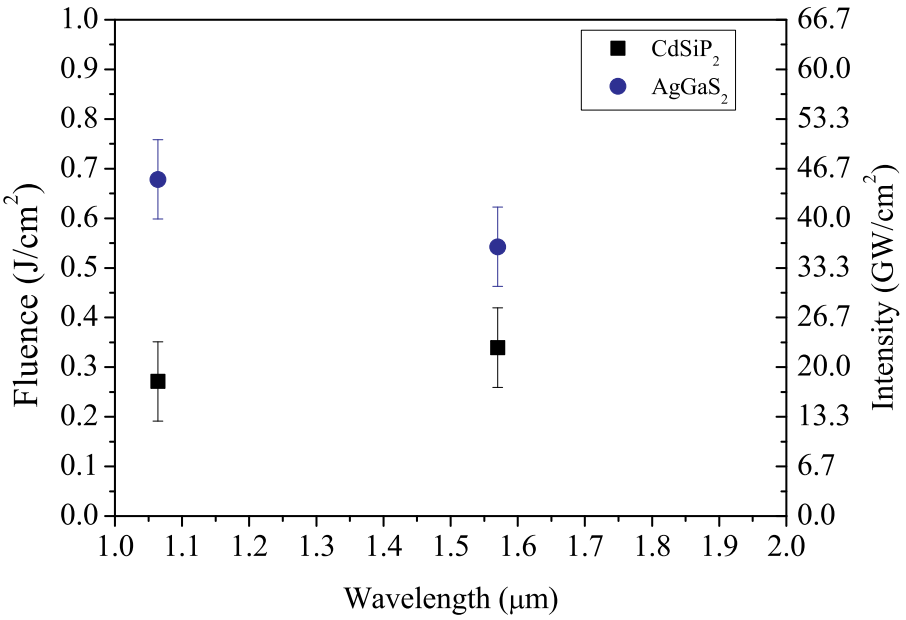

Figure 4.4: Comparison between the optical damage threshold of $CdSiP_2$ and $AgGaS_2$ at the wavelengths $1.064\,\mu\text{m}$ and $1.570\,\mu\text{m}$, and a pulse duration of 15 ps.

4.5 Measurement of the phase-matching directions

4.5.1 Experimental setup

In order to perform the sphere experiment, as described in chapter 2, it was necessary to cut and polish $CdSiP_2$ as a sphere. Our initial sample was a parallelepiped of dimensions $6.50 \times 5.15 \times 6.75$ mm provided by Peter G. Schunemann of BAE Systems in the framework of a collaboration. The cutting and polishing process was realized and led to a sphere of diameter 4.99 mm shown in Fig. 4.5. The asphericity $\Delta R/R$ is better than 1%.

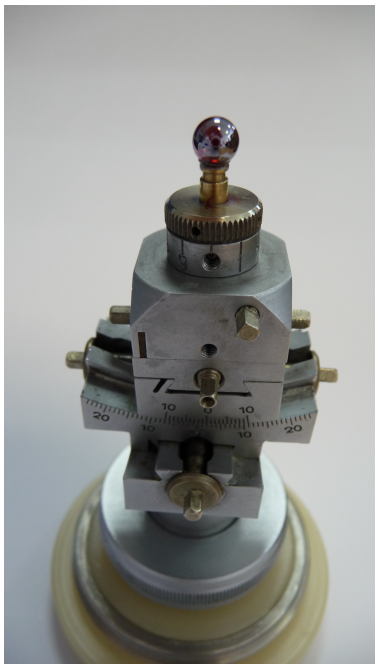

Figure 4.5: Picture of the sphere of $CdSiP_2$ of diameter 4.99 mm and asphericity better that 1% which was used for the sphere experiment.

We were able to determine the phase-matching directions of types I and II SHG, and types II and III DFG. Note that type I DFG is not compatible with the dispersion of the refractive indices given by Eq. 4.1. The position of the ZnSe entrance lens was systematically controlled in order to ensure a quasi-parallel propagation according to the fundamental wavelength for SHG, and according to the pump wavelength at 1.064 μm for DFG. Furthermore, since the incident beam radius was $w_{\text{inc}} \approx 5.4$ mm, we took care to keep an energy of the incident beam(s) below $E^{\text{th}} \approx 45\,\mu$J according to the calculation of chapter 2 shown in Fig. 2.10(a).

4.5.2 Calculation of the nonlinear coefficients

Before measuring phase-matching directions, it was necessary to study the variation of the nonlinear coefficient χ_{eff} according to the angles of spherical coordinates (θ, ϕ) of the dielectric frame. In particular, it was shown in chapter 1 that even if the ϕ angle has no infuence on the phase-matching directions in an uniaxial crystal, it can have an influence on the effective coefficient.

Many coefficients of the second order susceptibility vanish due to the crystalline symmetry $\bar{4}2m$ of $CdSiP_2$ [5]:

$$\chi^{(2)} = \begin{pmatrix} 0 & 0 & 0 & \chi_{xyz} & \chi_{xzy} & 0 & 0 & 0 & 0 \\ 0 & 0 & 0 & 0 & 0 & \chi_{yxz} & \chi_{yzx} & 0 & 0 \\ 0 & 0 & 0 & 0 & 0 & 0 & 0 & \chi_{zxy} & \chi_{zyx} \end{pmatrix} \tag{4.7}$$

and we have the following equalities between the nonzero coefficients [5]:

$$\chi_{xyz} = \chi_{yxz}\ ; \quad \chi_{xzy} = \chi_{yzx}\ ; \quad \chi_{zxy} = \chi_{zyx} \tag{4.8}$$

Furthermore, under the Kleinman symmetry approximation, all the 6 nonzero coefficients are equal [5]. According to Eq. 1.20, and thanks to the expression of the unit electric field vectors $\vec{e}^{\,o}$ and $\vec{e}^{\,e}$ given in Eqs. 1.8 and 1.9, it is possible to calculate the effective coefficient χ_{eff} as a function of θ and ϕ for types I, II and III SFG. We get under the Kleinman approximation:

$$\begin{aligned} \chi^{(2)}_{\text{eff}} &= -\chi_{xyz} \sin(\theta - \rho)\ \sin(2\phi) && \text{for type I SFG} \\ \chi^{(2)}_{\text{eff}} &= -\chi_{xyz} \sin\left[2(\theta - \rho)\right]\ \cos(2\phi) && \text{for type II SFG} \\ \chi^{(2)}_{\text{eff}} &= -\chi_{xyz} \sin\left[2(\theta - \rho)\right]\ \cos(2\phi) && \text{for type III SFG} \end{aligned} \tag{4.9}$$

The correspondance between the three types of SFG and the three types of DFG were given in table 1.1. While the θ angle is fixed by the phase-matching condition according to Eq. 1.24, the ϕ angle must be chosen in such a way that the effective coefficient is nonzero, the power of the generated wave being proportional to the square of χ_{eff} according to Eq. 1.22. Fig. 4.6 shows the variation of the $\sin^2(2\phi)$ function to which the generated power of type I SFG is proportional, and the $\cos^2(2\phi)$ one, describing the generated power of type II and III SFG.

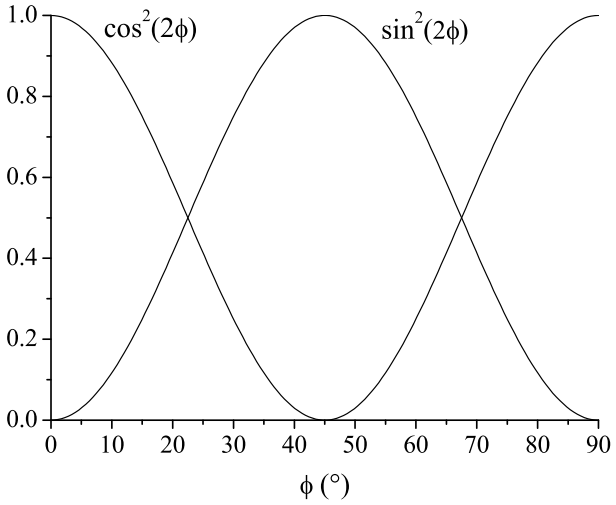

Figure 4.6: $\sin^2(2\phi)$ and $\cos^2(2\phi)$ functions governing the SFG and DFG effective coefficient in the range $0 < \phi < 90°$.

Due to mechanical obstruction with the Euler circle, it was not possible to access values of the ϕ angle exceeding 30°. Consequenly, we chose to realize the measurements at $\phi = 30°$ for type I SFG and at $\phi = 0°$ for types II and III SFG.

4.5.3 Second-harmonic generation

Second-harmonic generation (SHG) measurements were realized at $\phi = 30°$ for type I SHG and at $\phi = 0°$ for type II SHG. The polarization of the incident fundamental beam at λ_ω was controlled according to the chosen type. A glass filter (BK7) was used in order to cut the beam at λ_ω before detecting the beam at $\lambda_{2\omega}$. In order to perform this experiment, it was necessary to stick the sphere along the y direction on the goniometric head corresponding to the situation $y = Z$ in section 2.5. The directions of propagation are given in spherical coordinates (θ, ϕ) in the dielectric frame, the conversion from Euler angles being done thanks to Eq. 2.17. The results are shown in Fig. 4.7, where the experiments are compared with the resolution of the BPM phase-matching relation of Eq. 1.24 using the Sellmeier equations of Eq. 4.1. Note that there is a good agreement between theory and measurements for both type I and type II SHG. At $\theta = 47°$ corresponding to type I SHG at $\lambda_\omega = 4.0\,\mu$m, we took advantage of the possibility of varying the ϕ angle from 0° to 45° to verify the dependency in $\sin^2(2\phi)$ of the generated power at $\lambda_{2\omega}$. The conversion efficiency $\nu = \mathcal{P}^{2\omega}/\mathcal{P}^{\omega}$ is presented in Fig. 4.8.

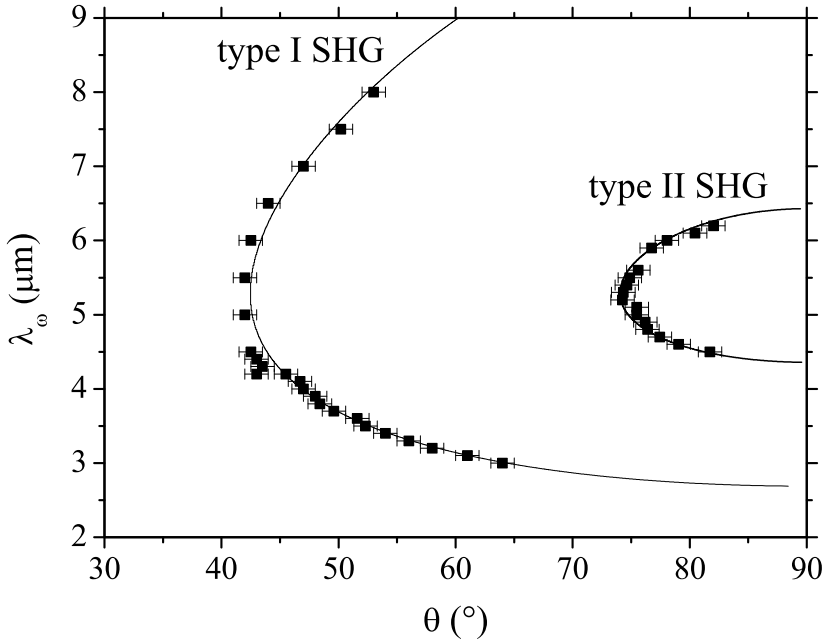

Figure 4.7: Tuning curves of Type I SHG in the $\phi = 30°$ plane and type II SHG in the $\phi = 0°$ plane. The dots correspond to the experimental data and the solid line is the calculation by solving Eq. 1.24 with $\lambda_1 = \lambda_2 = \lambda_\omega$ and $\lambda_3 = \lambda_{2\omega}$, using the Sellmeier equations given by Eq. 4.1.

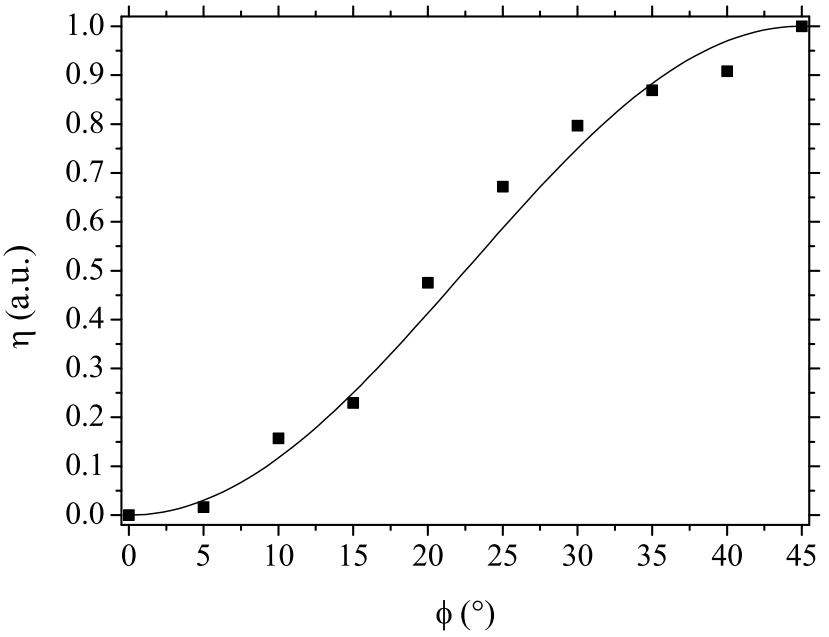

Figure 4.8: Type I SHG conversion efficiency at $\lambda_\omega = 4.0\,\mu$m as a function of ϕ when θ is fixed at 47°. The dots correspond to the experimental data and the solid line to the calculated $\sin^2(2\phi)$ function.

4.5.4 Difference-frequency generation

We are interested here in difference-frequency generation (DFG) involving a pump wave at $\lambda_p = 1.064\,\mu$m. The signal and idler waves being defined as $\lambda_p < \lambda_s < \lambda_i$, there are two possible experiments leading to the determination of the same phase-matching directions: the signal beam, is mixed to the pump beam and the generated idler beam is detected; or the idler beam is mixed to the pump beam and the generated signal beam is detected. Note that in both cases, the three wavelengths are linked by the energy conservation relation $\lambda_p^{-1} = \lambda_s^{-1} + \lambda_i^{-1}$. The main difference between the two cases concerns the experimental setup, λ_s belonging to the $1.1 - 1.2\,\mu$m interval while λ_i is in the $6 - 10\,\mu$m range.
Since the sensibility of our HgCdTe photodiode was not high enough, we chose the configuration with an incident idler beam, so that the detection was performed at λ_s. The phase-matching directions measurements are presented in Fig. 4.9. The discrimination between the different types was done thanks to the polarization of the incident beams.

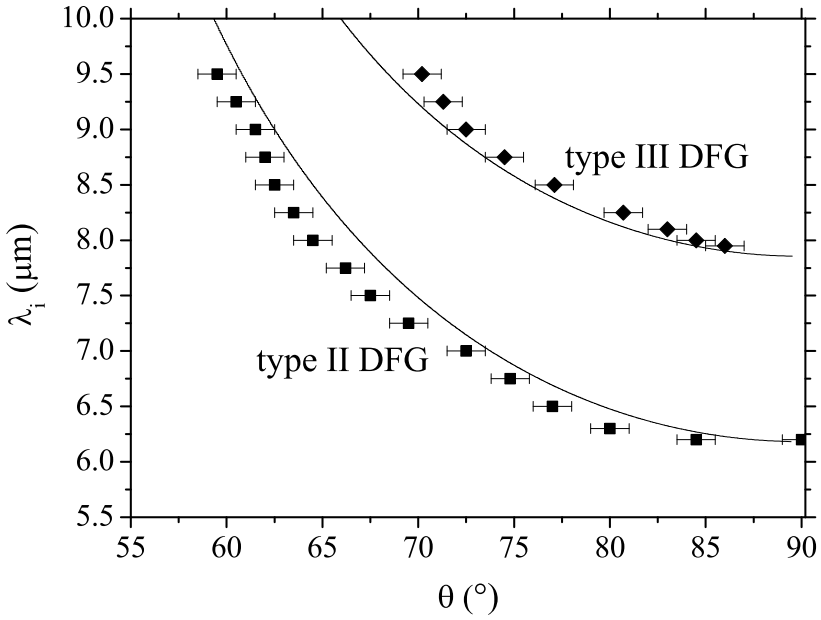

Figure 4.9: Tuning curves of type II DFG in the $\phi = 30°$ plane and type III DFG in the $\phi = 0°$ plane. The dots correspond to the experimental data and the solid line is the calculation by solving Eq. 1.24 using the Sellmeier equations given by Eq. 4.1.

We notice a discrepancy between the measurements and the calculation using the Sellmeier equations of Eq. 4.1, due to a lack of accuracy in the Sellmeier equations. Fig. 4.9 shows that types II and III DFG allow phase-matching for wavelengths ranging from $6.2\,\mu$m to $9.5\,\mu$m. The maximum generated wavelength of $9.5\,\mu$m is limited by the transparency win-

dow of $CdSiP_2$.
Type I DFG was not found, as predicted by the Sellmeier equations 4.1.

4.6 Refractive index refinement

The sphere measurements previously described show that the Sellmeier equations given by Eq. 4.1 are not reliable over the whole transparency range of the material, probably because they result from a prism experiment up to 5.0 μm. However, by fitting simultaneously all our SHG and DFG experimental data, we were able to refine the dispersion of the refractive indices. The wavelength ranges of measurements are given in Fig. 4.10 according to the different interactions.

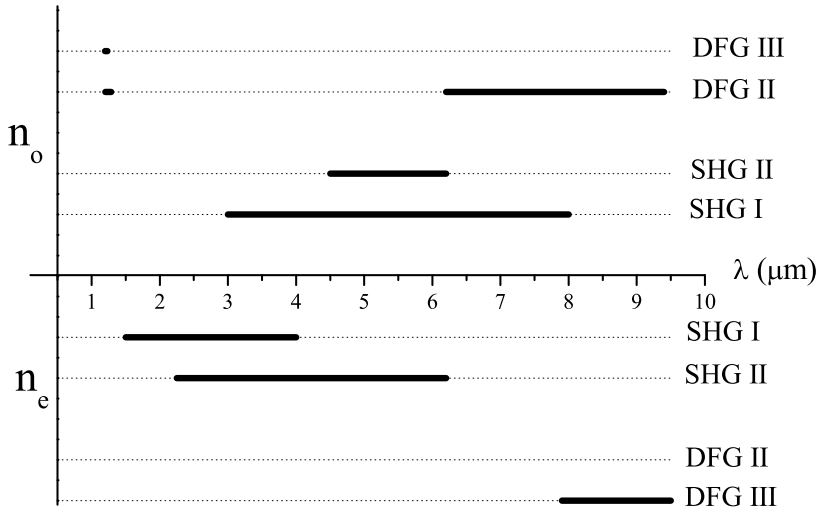

Figure 4.10: Wavelength ranges covered by the experimental data over which the principal refractive indices n_o and n_e of $CdSiP_2$ were sollicited.

As an example, data were recorded for type II SHG corresponding to $\lambda_\omega^o + \lambda_\omega^e = \lambda_{2\omega}^e$ over the range $4.5 < \lambda_\omega < 6.2\,\mu$m: n_o and n_e are thus involved through λ_ω in the range $4.5 - 6.2\,\mu$m, while n_e is involved through $\lambda_{2\omega}$ in the range $2.25 - 3.1\,\mu$m. Fig. 4.10 shows that the measurements allow the infrared range to be well covered from 3 to 9.5 μm for both the ordinary and the extraordinary indices. However, the wavelengths below 1.064 μm are not covered.

The fit of all our experimental data was realized using the Levenberg-Marquardt algorithm encoded with MATLAB. Different forms of Sellmeier equations were tested. The best result was obtained by using the following dual oscillator form:

$$n_i^2 = A_i + \frac{B_i\,\lambda^{p_i}}{\lambda^{p_i} - C_i} + \frac{D_i\,\lambda^{q_i}}{\lambda^{q_i} - E_i} - F_i\,\lambda^2 \tag{4.10}$$

where i=(o,e). The fitting curves are given in Figs. 4.11 and 4.12. They show the fit led to a better agreement, especially for DFG. The corresponding coefficients of Eq. 4.10 are given in table 4.2.

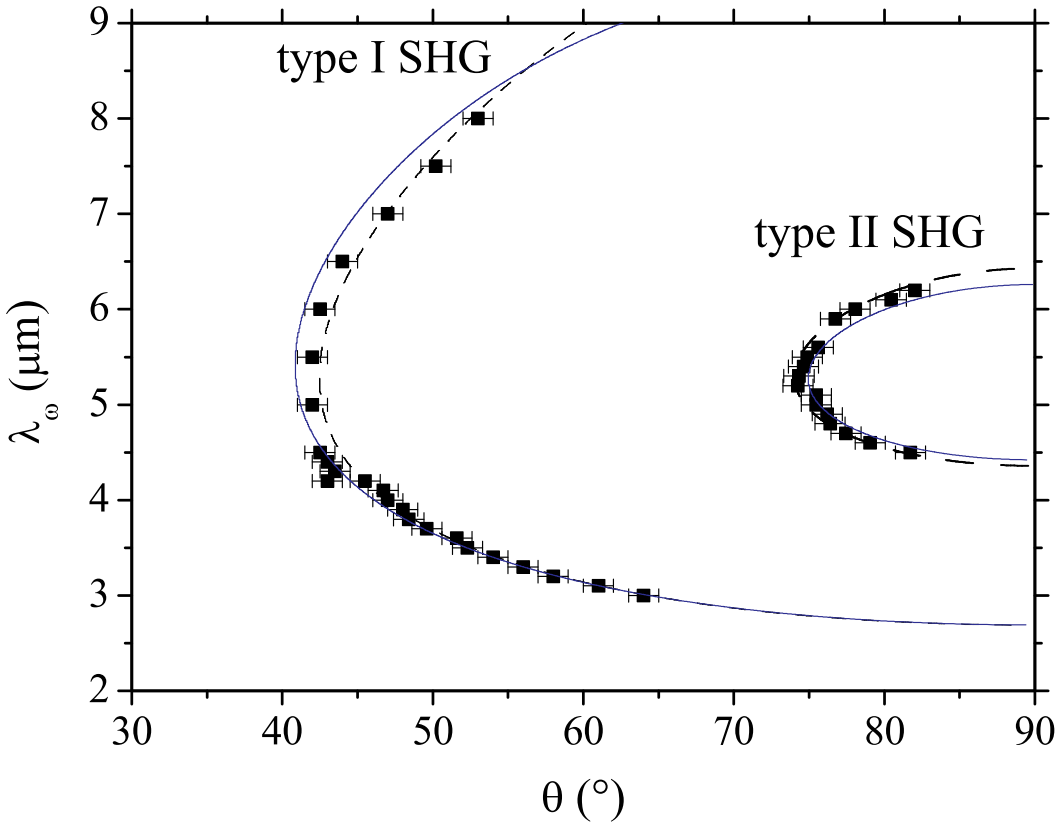

Figure 4.11: Types I and II SHG tuning curves of $CdSiP_2$; the fundamental wavelength λ_ω is given as a function of θ. Dots stand for experimental data, dashed lines correspond to calculations from Sellmeier equations of Eq. 4.1 and solid lines are the fit of the experimental data.

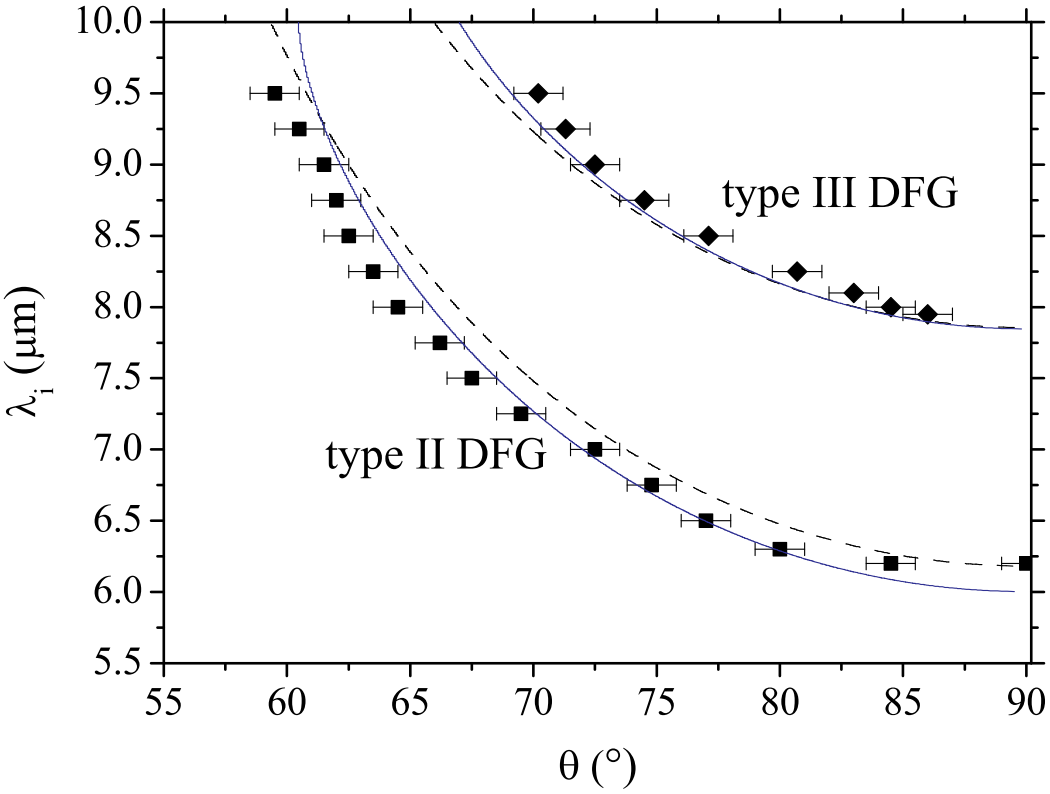

Figure 4.12: Types II and III DFG tuning curves of $CdSiP_2$ with a pump at 1.064 μm; λ stands for the idler wavelength, plotted as a function of θ. Dots stand for experimental data, dashed lines correspond to calculations from Sellmeier equations of Eq. 4.1 and solid lines are the fit of the experimental data.

A^o	3.8470	A^e	3.3427
B^o	5.4882	B^e	5.6907
C^o	0.1195	C^e	0.1161
D^o	0.0713	D^e	0.0127
E^o	170.48	E^e	249.06
F^o	0.0024	F^e	0.0039
p_o	2.0093	p_e	2.0001
q_o	2.0853	q_e	2.2101

Table 4.2: Sellmeier coefficients relative to the ordinary (o) and extraordinary (e) principal refractive indices of $CdSiP_2$ at $T = 22°C$.

4.7 Spectral acceptance

The spectral acceptance was measured by recording the power of the generated beam as a function of the wavelength around a phase-matching direction. The example of type II DFG along the x-direction is shown in Fig. 4.13.

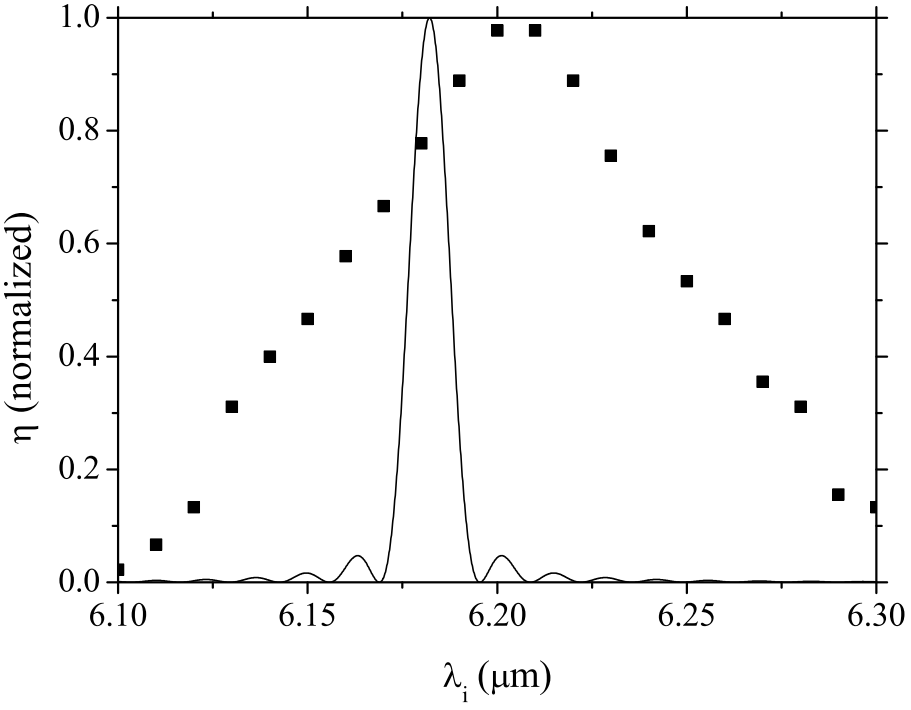

Figure 4.13: Measured (dots) and calculated (continuous line) variation of the normalized conversion efficiency η of type II DFG pumped at $\lambda_p = 1.064\,\mu$m along the x-direction as a function of the wavelength in the sphere of $CdSiP_2$ of diameter 4.99 mm.

Excluding the small discrepancy of the phase-matching wavelength, for which the generated power is maximum, we see in Fig. 4.13 that the measured spectral acceptance is much higher than the calculated one, the experiment giving $\delta\lambda_i = 122\,$nm since the calculus predicts $\delta\lambda_i = 14\,$nm. There is thus an error of a factor larger than 8 between the measurement and the calculus. This error could be attribuated to a non parallel propagation of one of the beams inside the sphere. But in fact, it is probably due to the fact that the sphere was considerably damaged prior to this measurement, leading to a strong decrease of the effective interaction length. Then according to Fig. 4.13, one can conclude that only $\approx 0.6\,$mm ($= 4.99\,$mm$/8$) is active.

The spectral acceptances of SHG and DFG were calculated using our refined Sellmeier equations. The cases of type II and type III DFG pumped at $\lambda_p = 1.064\,\mu$m is presented in Fig. 4.14.

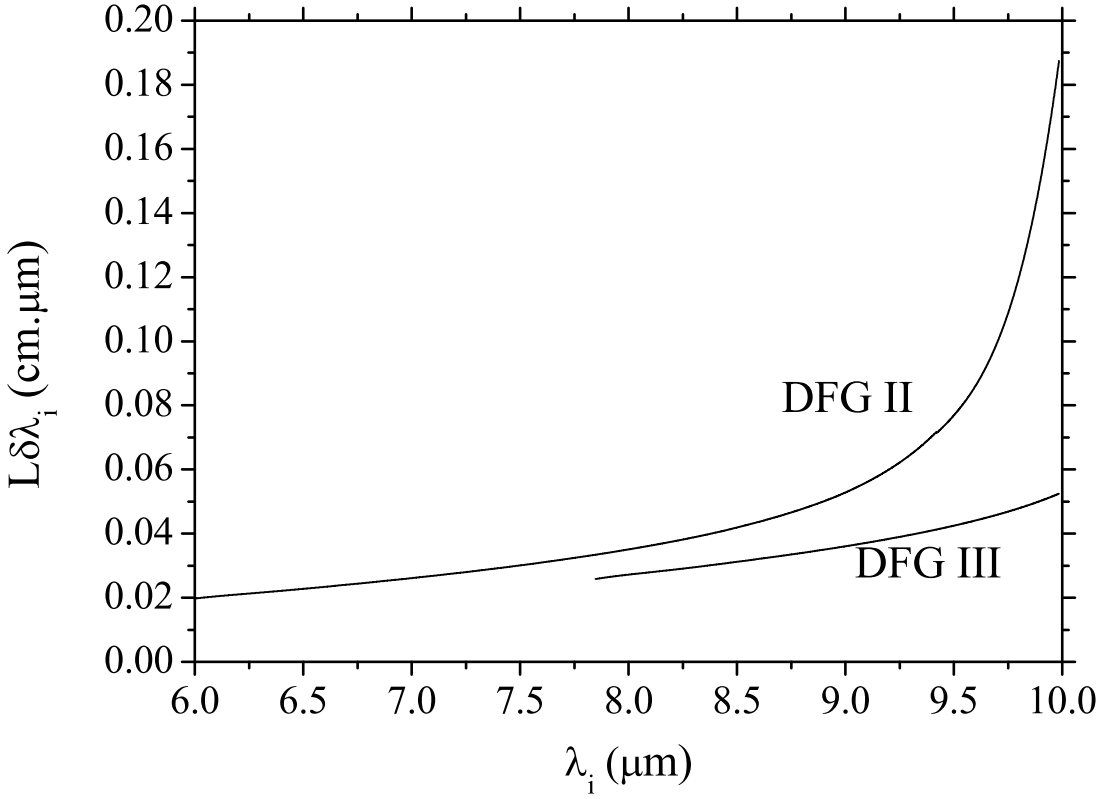

Figure 4.14: Calculated spectral acceptances $L\delta\lambda_i$ of types II and III DFG in $CdSiP_2$ pumped at $\lambda_p = 1.064\,\mu$m as a function of the idler wavelength λ_i.

Note that the spectral acceptance increases with an increasing wavelength, which can be directly linked to the derivative $d\lambda_i/d\theta$ of the tuning curves of Fig. 4.12: the higher $d\lambda_i/d\theta$ is, the higher $L\delta\lambda_i$ is.

4.8 Potentialities of $CdSiP_2$ for parametric devices

The DFG curves presented in Fig. 4.12 directly show the tuning possibility that would have an OPO based on $CdSiP_2$ and pumped by a Nd:YAG laser at $1.064\,\mu$m. By using our refined Sellmeier equations, we are able to calculate the DFG tuning curves obtained with other pump wavelengths. We chose $\lambda = 1.57\,\mu$m and $\lambda = 2\,\mu$m since they correpond to

classical pump wavelengths [70, 71], the other interest being that they cannot lead to two-photon absorption according to the gap of $CdSiP_2$. The corresponding curves are presented respectively in Figs. 4.15 and 4.16.

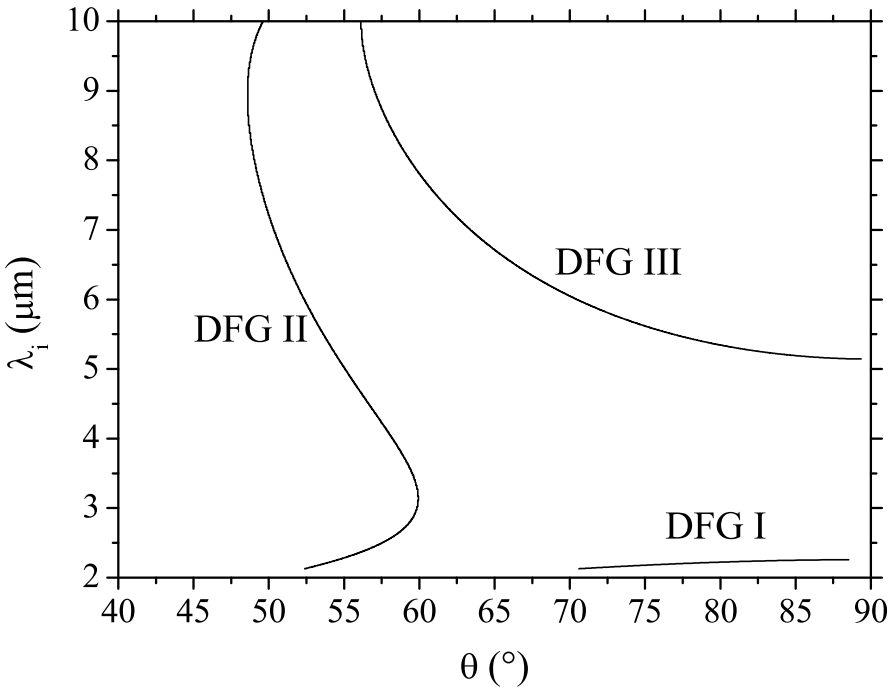

Figure 4.15: Calculated types I, II and III DFG tuning curves in $CdSiP_2$ with a pump wavelength $\lambda_p = 1.570\,\mu$m.

Note that even if it is not interesting for far infrared generation, type I DFG is allowed in $CdSiP_2$ at these pump wavelengths, which was not the case at $\lambda_p = 1.064\,\mu$m. Fig. 4.16 shows that type II DFG pumped at $2\,\mu$m may be interesting for generating ultra broad-band spectral output between $2.5\,\mu$m and $10\,\mu$m by using a very narrow angular tunability around $\theta = 45°$, which corresponds to a strong spectral non criticity.
However, type III allows a wide tuning range at the two considered pump wavelengths by tuning the θ angle over 30° as shown in Figs. 4.15 and 4.16. It has been shown that such a large angular tuning associated to a strong angular non criticity can be realized by the use of a cylindrical crystal [72], the advantage being a weak sensitivity to the possible pointing fluctuation and to the divergence of the beam.

Figs. 4.12, 4.15 and 4.16 enable the comparison between the potentialities corresponding to the different pump wavelengths. We notice that the higher the pump wavelength is, the wider the spectral tunability is. As an example, the accessible tunability of type III

DFG increases from $7.8 - 10\,\mu$m for $\lambda_p = 1.064\,\mu$m to $4.4 - 10\,\mu$m for $\lambda_p = 2\,\mu$m.

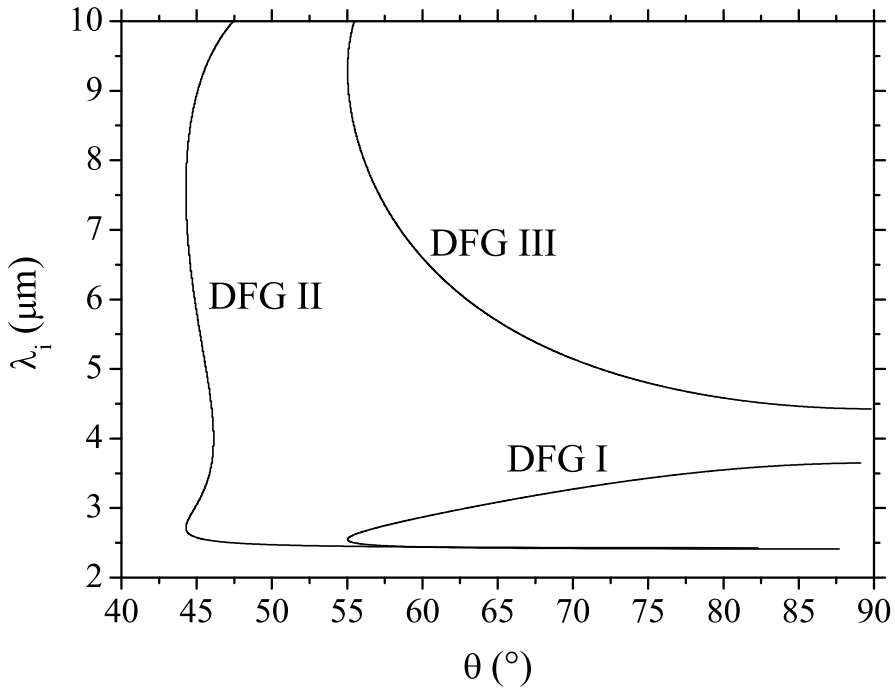

Figure 4.16: Calculated types I, II and III DFG tuning curves in $CdSiP_2$ with a pump wavelength $\lambda_p = 2\,\mu$m.

4.9 Conclusion

This experimental study of the optical nonlinear properties of $CdSiP_2$ over its whole transparency range has demonstrated the possibility of generating infrared light until $9.5\,\mu$m by parametric interactions. The material is no more transparent above this wavelength. The DFG experiments have also demonstrated the possibility of pumping $CdSiP_2$ by a Nd:YAG laser, which is an important asset that other nonlinear crystals of the infrared, like $ZnGeP_2$ or CdSe, do not have. However, the optical damage threshold of $CdSiP_2$ at $1.064\,\mu$m is below our expectations, leaving the superiority to $AgGaS_2$. The precise knowledge of the Sellmeier equations of $CdSiP_2$ resulting from this work is of prime importance for the design of OPOs emitting in the $3 - 9.5\,\mu$m range.

Conclusion

This work was devoted to the experimental study of the optical properties of 5%MgO:PPLN and $CdSiP_2$, the motivation being the development of coherent optical sources emitting between $3\,\mu$m and $12\,\mu$m. The sphere method, that had already shown its ability in the past few years, was the ideal method in order to carry out an exhaustive study of the phase-matching properties of these crystals.

On one hand, the *angular quasi-phase-matching* concept was verified on 5%MgO:PPLN. It was shown that angular quasi-phase-matching presents advantages over birefringence phase-matching or classical quasi-phase-matching, as well for the spectral tunability range as for the spectral acceptance. Furthermore, even if this material was widely used, its refractive indices were not known with good accuracy. The Sellmeier equations resulting from the fit of all our experiments can be considered as a reference for future works.

On the other hand, parametric generation until $9.5\,\mu$m was demonstrated in $CdSiP_2$. Even if the optical damage threshold in the near infrared was not as good as expected, $CdSiP_2$ remains a good candidate for a continuous spectral tunability in the third atmospheric transparency band by angular tuning. The Sellmeier equations were refined in order to calculate phase-matching conditions with accuracy in future devices.

In prospect, the work on angular quasi-phase-matching will be extended to new periodically-poled materials like MgO:PPLiTaO_3 and PPKTP. The group of Néel Institute also plans to perform an exhaustive study on a GaN cylinder in order to evaluate its potentialities.

Bibliography

[1] N. Bloembergen. *Nonlinear optics*. New York: Benjamin, 1965.

[2] Y. Petit, B. Boulanger, P. Segonds, and T. Taira. Angular quasi-phase-matching. *Phys. Rev. A*, 76:1–7, 2007.

[3] A. Yariv. *Optical waves in crystals*. New York: Wiley, 2002.

[4] J. F. Nye. *Physical properties of crystals*. Oxford: Clarendon Press, 1957.

[5] B. Boulanger and J. Zyss. *Physical Properties of Crystals*. International Tables of Crystallography, Vol. D, 2000.

[6] M. Born and E. Wolf. *Principles of Optics*. Pergamon Press, Sixth Edition, 1980.

[7] M. V. Hobden. Phase-matched second harmonic generation in biaxial crystals. *J. Appl. Phys.*, 38:4365–4372, 1967.

[8] M. M. Fejer, G. A. Magel, D. H. Jundt, and R. L. Byer. Quasi-phase-matched second harmonic generation: tuning and tolerances. *IEEE J. of Quantum Electron*, 28:2631, 1992.

[9] Yannick Petit. *Nouvelles approches en optique cristalline : distributions angulaires de l'absorption et de l'émission, auto-doublage, quasi-accord de phase angulaire*. PhD thesis, Université Joseph Fourier, Grenoble, 2007.

[10] N. E. Yu, S. Kurimura, K. Kitamura, J. H. Ro, M. Cha, S. Ashihara, T. Shimura, K. Kuroda, and T. Taira. Efficient frequency doubling of a femtosecond pulse with simultaneous group-velocity matching and quasi phase matching in periodically poled, MgO-doped, lithium niobate. *Appl. Phys. Lett.*, 82:3388–3390, 2003.

[11] N. E. Yu, J. H. Ro, M. Cha, K. Kitamura, and T. Taira. Broadband quasi-phase-matched second-harmonic generation in MgO-doped periodically poled $LiNbO_3$ at the communications band. *Opt. Lett.*, 27:1046–1048, 2002.

[12] H. Liu, R. Zhang, H. Liu, J. Ma, C. Zhu, and Q. Wang. Investigation of spectral bandwidth of BBO-I phase matching non-collinear optical parametric amplification from visible to near-infrared. *Front. Optoelectron. China*, 1:101–108, 2008.

[13] G. Marnier and B. Boulanger. The sphere method: A new technique in linear and non-linear crystalline optical studies. *Opt. Comm.*, 72:139–143, 1989.

[14] B. Boulanger, J. P. Fève, G. Marnier, C. Bonnin, P. Villeval, and J. J. Zondy. Absolute measurement of quadratic nonlinearities from phase-matched second-harmonic generation in a single KTP crystal cut as a sphere. *J. Opt. Soc. Am. B*, 14:1380–1386, 1997.

[15] Y. Guillien, B. Ménaert, J. P.. Fève, P. Segonds, J. Douady, B. Boulanger, and O. Pacaud. Crystal growth and refined Sellmeier equations over the complete transparency range of $RbTiOPO_4$. *Optical Materials*, 22:155–162, 2003.

[16] J. P. Fève, B. Boulanger, O. Pacaud, I. Rousseau, B. Ménaert, G. Marnier, P. Villeval, C. Bonnin, G. M. Loiacono, and D. N. Loiacono. Phase-matching measurements and Sellmeier equations over the complete transparency range of $KTiOAsO_4$, $RbTiOAsO_4$ and $CsTiOAsO_4$. *J. Opt. Soc. Am. B*, 17:775–780, 2000.

[17] P. Segonds, B. Boulanger, J. P.. Fève, B. Ménaert, J. Zaccaro, G. Aka, and D. Pelenc. Linear and nonlinear optical properties of the monoclinic $Ca_4YO(BO_3)_3$ crystal. *J. Opt. Soc. Am. B*, 21:765–769, 2004.

[18] P. Segonds, B. Boulanger, B. Ménaert, J. Zaccaro, J. P. Salvestrini, M. D. Fontana, R. Moncorgé, F. Porée, G. Gadret, J. Mangin, A. Brenier, G. Boulon, G. Aka, and D. Pelenc. Optical characterizations of $YCa_4O(BO_3)_3$ and $Nd{:}YCa_4O(BO_3)_3$ crystals. *Optical Materials*, 29:975–982, 2007.

[19] A. E. Siegman. *Lasers*. Hardcover, 1986.

[20] Gerrard and B. Burch. *Matrix methods in optics*. New York: John Wiley & Sons, 1975.

[21] http://refractiveindex.info/?group=crystals&material=znse.

[22] http://www.casix.com/product/prod_cry_linbo3.html.

[23] P. G. Schunemann, K. T. Zawilski, T. M. Pollak, V. Petrov, and D. E. Zelmon. $CdSiP_2$: a new nonlinear optical crystal for 1- and 1.5-micron-pumped mid-IR generation. In *Advance Solid-State Photonics (ASSP)*, 2008.

[24] L. E. Myers, G. D. Miller, R. C. Eckardt, M. M. Fejer, R. L. Byer, and W. R. Bosenberg. Quasi-phase-matched 1.064 μm-pumped optical parametric oscillator in bulk periodically poled $LiNbO_3$. *Opt. Lett.*, 20:52–54, 1995.

[25] M. H. Niemz. Threshold dependance of laser-induced optical breakdown on pulse duration. *Appl. Phys. Lett.*, 66:1181–1183, 1995.

[26] G. Arfken. *Mathematical Methods for Physicists*. Orlando, FL: Academic Press, 1985.

[27] H. Karlsson and F. Laurell. Electric field poling of flux grown $KTiOPO_4$. *Appl. Phys. Lett.*, 71:3474, 1997.

[28] F. Rotermund, C. J. Yoon, V. Petrov, F. Noack, S. Kurimura, N. E. Yu, and K. Kitamura. Application of periodically poled stoichiometric $LiTaO_3$ for efficient optical parametric chirped pulse amplification at 1 kHz. *Opt. Express*, 12:6421, 2004.

[29] T. Skauli, K. L. Vodopyanov, T. J. Pinguet, A. Schober, O. Levi, L. A. Eyres, M. M. Fejer, J. S. Harris, B. Gerard, L. Becouarn, E. Lallier, and G. Arisholm. Measurement of the nonlinear coefficient of orientation-patterned GaAs and demonstration of highly efficient second-harmonic generation. *Opt. Lett.*, 27:628–630, 2002.

[30] J. P.. Fève, B. Boulanger, B. Ménaert, and O. Pacaud. Continuous tuning of a microlaser-pumped optical parametric generator by use of a cylindrical periodically poled lithium niobate crystal. *Opt. Lett.*, 28:1028–1030, 2003.

[31] H. Ishizuki, T. Taira, S. Kurimura, J. H. Ro, , and M. Cha. Periodic poling in 3-mm-thick MgO:$LiNbO_3$ crystals. *Jpn. J. of Appl. Phys.*, 42:108–110, 2003.

[32] P. Brand, B. Boulanger, P. Segonds, Y. Petit, C. Félix, B. Ménaert, T. Taira, and H. Hishizuki. Angular quasi-phase-matching experiments and determination of accurate Sellmeier equations for 5%MgO:PPLN. *Opt. Lett.*, 34:2578–2580, 2009.

[33] O. Gayer, Z. Sacks, E. Galun, and A. Arie. Temperature and wavelength dependent refractive index equations for MgO-doped congruent and stoichiometric $LiNbO_3$. *Appl. Phys. B*, 91:343–348, 2008.

[34] P. Brand, B. Boulanger, P. Segonds, Y. Petit, C. Félix, B. Ménaert, H. Hishizuki, and T. Taira. Angular quasi-phase-matching: theory and experiment. *Proc. SPIE*, 7197:719706, 2009.

[35] Paschotta and Rüdiger. *Encyclopedia of Laser Physics and Technology*. Wiley-VCH, Berlin, 2008.

[36] M. Beutler, M. Ghotbi, F. Noack, D. Brida, C. Manzoni, and G. Cerullo. Generation of high-energy sub-20 fs pulses tunable in the 250-310 nm region by frequency doubling of a high-power noncollinear optical parametric amplifier. *Opt. Lett.*, 34:710–712, 2009.

[37] J. P. Meyn, M. E. Klein, D. Woll, and R. Wallenstein. Periodically poled potassium niobate for second-harmonic generation at 463 nm. *Opt. Lett.*, 24:1154–1156, 1999.

[38] C. K. N. Patel. Efficient phase-matched harmonic generation in tellurium with a CO_2 laser at 10.6 microns. *Phys. Rev. Lett.*, 15:1026–1030, 1965.

[39] C. K. N. Patel. Optical harmonic generation in the infrared using a CO_2 laser. *Phys. Rev. Lett.*, 16:613–616, 1966.

[40] M. Tacke. New developments and applications of tunable IR lead salt lasers. *Infrared Phys. Technol.*, 36:447–463, 1995.

[41] A. Godard. *Infrared (2-12 μm) solid-state laser sources: a review*. C. R. Physique, 2007.

[42] I. Vurgaftman and J. R. Meyer. Analysis of limitations to wallplug efficiency and output power for quantum cascade lasers. *J. Appl. Phys.*, 99:123108, 2006.

[43] http://sales.hamamatsu.com/en/products/laser-group/qcl.php.

[44] R. L. Byer. *Treatise in quantum electronics*. New York: Academic Press, 1973.

[45] S. E. Harris. Tunable optical parametric oscillators. *Proc. IEEE*, 57:2096–2113, 1969.

[46] G. Mennerat. *Conception, Modélisation et Réalisation d'une Source Cohérente de Forte Energie Accordable dans le Moyen Infrarouge*. PhD thesis, Université Louis Pasteur, Strasbourg, 2000.

[47] S. Wang, V. Pasiskevicius, F. Laurell, and H. Karlsson. Ultraviolet generation by first-order frequency doubling in periodically poled $KTiOPO_4$. *Opt. Lett.*, 23:1883, 1998.

[48] A. Harasaki and K. Kato. New data on the nonlinear optical constant , phase-matching and optical damage of $AgGaS_2$. *Jpn. J. Appl. Phys.*, 36:700–703, 1997.

[49] H. Kildal and J. C. Mikkelsen. The nonlinear optical coefficient, phasematching, and optical damage in the chalcopyrite $AgGaSe_2$. *Optics Communications*, 9:315–318, 1973.

[50] K. L. Vodopyanov, F. Ganikhanov, J. P. Maffetone, I. Zwieback, and W. Ruderman. $ZnGeP_2$ optical parametric oscillator with 3.8-12.4 μm tunability. *Opt. Lett.*, 25:841–843, 2000.

[51] S. Haidar, K. Miyamoto, and H. Ito. Generation of tunable mid-IR (5.5-9.3 μm) from a 2 μm pumped $ZnGeP_2$ optical parametric oscillator. *Optics Communications*, 241:173–178, 2004.

[52] K. L. Vodopyanov and P. G. Schunemann. Broadly tunable noncritically phase-matched $ZnGeP_2$ optical parametric oscillator with a 2 μm pump threshold. *Opt. Lett.*, 28:441–443, 2003.

[53] A. Zakel et al. Advanced solid-state photonics. *OSA*, 98:433–437, 2005.

[54] N. A. Sandford, L. H. Robins, A. V. Davydov, A. Shapiro, D. V. Tsetkov, and A. V. Dmitriev. Refractive index study of $Al_xGa_{1-x}N$ films grown on sapphire substrates. *J. Appl. Phys.*, 94:2980–2990, 2003.

[55] J. Miragliotta, D. K. Wickenden, T. J. Kistenmacher, and W. A. Bryden. Linear-and nonlinear-optical properties of GaN thin films. *J. Opt. Soc. Am. B*, 10:1447–1456, 1993.

[56] A. Chowdhury, H. M. Ng, M. Bhardwaj, and N. G. Weimann. Second-harmonic generation in periodically poled GaN. *Appl. Phys. Lett.*, 83:1077–1079, 2003.

[57] K. Waldrip. Electrolysis: a surprising method for scaling GaN crystal growth. *Compound Semiconductor*, 14:28–30, 2008.

[58] A. Chowdhury, H. M. Ng, M. Bhardwaj, and N. G. Weimann. Second-harmonic generation in periodically poled GaN. *Appl. Phys. Lett.*, 83:1077–1079, 2003.

[59] A. Mustelier, E. Rosencher, P. Kupecek, A. Godard, M. Baudrier, M. Lefebvre, M. Poulat, G. Mennerat, C. Pasquer, and P. Lemasson. Midinfrared difference frequency generation in quasi-phase matched diffusion bonded ZnSe plates. *Appl. Phys. Lett.*, 84:4422–4426, 2004.

[60] M. Raybaut, A. Godard, C. Lubin, R. Haidar, and E. Rosencher. *Fresnel phase matching: a universal phase matching scheme*. C. R. Physique, 2007.

[61] T. Skauli, K. L. Vodopyanov, T. J. Pinguet, A. Schober, O. Levi, L. A. Eyres, M. M. Fejer, J. S. Harris, B. Gerard, L. Becouarn, E. Lallier, and G. Arisholm. Measurement of the nonlinear coefficient of orientation-patterned GaAs and demonstration of highly efficient second-harmonic generation. *Opt. Lett.*, 27:628–630, 2002.

[62] K. L. Vodopyanov, O. Levi, P. S. Kuo, T. J. Pinguet, J. S. Harris, and M. M. Fejer. Optical parametric oscillation in quasi-phase-matched GaAs. *Opt. Lett.*, 29:1912–1914, 2004.

[63] P. S. Kuo, K. L. Vodopyanov, M. M. Fejer, D. M. Simanovskii, X. Yu, J. S. Harris, D. Bliss, and D. Weyburne. Optical parametric generation of a mid-infrared continuum in orientation-patterned GaAs. *Opt. Lett.*, 31:71–73, 2006.

[64] Peter Schunemann. Advances in nlo crystals for infrared parametric sources.

[65] Peter Schunemann. New mid-IR nonlinear optical crystal: $CdSiP_2$.

[66] V. Petrov, P. G. Schunemann, K. T. Zawilski, and T. M. Pollak. Noncritical singly resonant optical parametric oscillator operation near $6.2\,\mu m$ based on a $CdSiP_2$ crystal pumped at $1064\,nm$. *Opt. Lett.*, 34:2399–2401, 2009.

[67] R. Maulini. External cavity quantum-cascade laser tunable from 8.2 to 10.4 microns using a gain element with a heterogeneous cascade. *Appl. Phys. Lett.*, 88:201113, 2006.

[68] N. Itoh, T. Fujinaga, and T. Nakau. Birefringence in $CdSiP_2$. *Jpn. J. Appl. Phys.*, 17:951–952, 1978.

[69] P. G. Schunemann and T. M. Pollak. U.S. Patent No. 5,611,856, 1997.

[70] C. Kieleck, M. Eichhorn, A. Hirth, D. Faye, and E. Lallier. High-efficiency 20-50 kHz mid-infrared orientation-patterned gaas optical parametric oscillator pumped by a $2\,\mu$m holmium laser. *Opt. Lett.*, 34:262–264, 2009.

[71] S. Chandra, T. H. Allik, G. Catella, R. Utano, and J. A. Hutchinson. Continuously tunable, $6-14\,\mu$m silver-gallium selenide optical parametric oscillator pumped at $1.57\,\mu$m. *Appl. Phys. Lett.*, 71:584–586, 1997.

[72] J. P. Fève, O. Pacaud, B. Boulanger, B. Ménaert, and M. Renard. Tunable phase-matched optical parametric oscillators based on a cylindrical crystal. *J. Opt. Soc. Am. B*, 19:222–233, 2002.

Abstract

This work is devoted to the study of the nonlinear optical properties of 5%MgO:PPLN and $CdSiP_2$, the motivation being the development of parametric optical sources in the second and third atmospheric transparency bands. These two crystals were cut as spheres in order to perform second harmonic generation and difference frequency generation in any direction of propagation by keeping normal incidence. Sphere experiments in 5%MgO:PPLN allowed us to validate at first the theory of angular quasi-phase-matching (AQPM), a general configuration corresponding to a waves propagation at any angle with respect to the grating vector. We experimentally confirmed that AQPM enables to provide wider spectral range and acceptance than birefringence phase-matching. Thanks to these measurements, it was also possible to refine the Sellmeier equations of 5%MgO:PPLN. The exhaustive nonlinear properties of $CdSiP_2$, a new nonlinear crystal, were measured over its whole transparency range. The possibility to generate wavelengths above $8\,\mu$m by difference frequency generation involving a pump wavelength at $1.064\,\mu$m was confirmed. The measurements of phase-matching directions of second harmonic generation and difference frequency generation allowed the Sellmeier equations to be refined. Finally, the optical damage threshold of $CdSiP_2$ was measured and compared with $AgGaS_2$, which is the main competitor for infrared generation above $8\,\mu$m. All the results that were obtained constitute a reliable basis for further studies devoted to the design of new infrared optical parametric devices.

Key words: infrared parametric generation, angular quasi-phase matching, nonlinear optics

Résumé

Ce travail est consacré à l'étude des propriétés optiques non linéaires de PPLN:5%MgO et $CdSiP_2$, la motivation étant le développement de sources paramétriques optiques dans les seconde et troisième bandes de transmission de l'atmosphère. Ces deux cristaux ont été polis sous forme de sphère pour réaliser des mesures de génération de second harmonique et de génération par différence de fréquences dans toutes les directions en gardant une incidence normale. Les expériences sur sphère de PPLN:5%MgO ont d'abord permis de valider la théorie du quasi-accord de phase angulaire (QAPA), une configuration générale correspondant à une propagation des ondes selon une direction quelconque par rapport au vecteur réseau. Nous avons expérimentalement confirmé que le QAPA permet l'existence d'un domaine spectral plus étendu et de plus grande acceptance spectrale que l'accord de phase par biréfringence. Toutes ces mesures ont aussi permis d'affiner les équations de Sellmeier de PPLN:5%MgO. Les propriétés non linéaires exhaustives de $CdSiP_2$, un nouveau cristal non linéaire, ont été mesurées sur toute sa fenêtre de transparence. La possibilité de générer des longueurs d'onde au-delà de $8\,\mu$m par différence de fréquences impliquant une onde à $1.064\,\mu$m a été confirmée. Les mesures des directions daccord de phase de génération de second harmonique de différence de fréquences ont permis d'affiner les équations de Sellmeier. Enfin, le seuil de dommage optique de $CdSiP_2$ a été mesuré et comparé à $AgGaS_2$, qui est son principal concurrent pour la génération dans l'infrarouge au-delà de $8\,\mu$m. Tous les résultats obtenus constituent une solide base pour les prochaines études consacrées à la conception de dispositifs paramétriques optiques pour l'infrarouge.

Mots clés : génération paramétrique infrarouge, quasi-accord de phase angulaire, optique non linéaire